Drag in Binaries

Addressing the role of hydrodynamics in stellar binary evolution

Dissertation submitted for the degree of

Philosophiæ Doctor

to the PhD School of the Faculty of Science,
University of Copenhagen

Sophie Lund Schrøder

Examiners

Prof. Irene Tamborra
Prof. Katherine Blundell
Prof. Daniel Holz

Supervisors

Prof. Enrico Ramirez-Ruiz
Prof. Jens Hjorth

PUBLICATIONS RELATED TO THIS THESIS

This thesis has used material from the following first- and co-authored publications:

- *"Black Hole Formation in Fallback Supernova and the Spins of LIGO Sources,"*
  Sophie Lund Schrøder, Aldo Batta, Enrico Ramriez-Ruiz.
  APJl, Volume 862, Issue 1, article id. L3, 6 pp. (2018). arXiv:1805.01269.

- *"Explosions Driven by the Coalescence of a Compact Object with the Core of a Massive-star Companion inside a Common Envelope: Circumstellar Properties, Light Curves, and Population Statistics,"*
  Sophie Lund Schrøder, Morgan MacLeod, Abraham Loeb, Alejandro Vigna-Gómez, Ilya Mandel.
  APJ, Volume 892, Issue 1, id.13, 18 pp. (2020). arXiv:1906.04189.

- *"Accretion Disk Formation in LIGO Black Hole Binaries and Electromagnetic Counterparts,"*
  Sophie Lund Schrøder, Enrico Ramirez-Ruiz.
  Work in progress.

- *"Fallback Supernova Assembly of Heavy Binary Neutron Stars and Light Black Hole-Neutron Star Pairs and the Common Stellar Ancestry of GW190425 and GW200115,"*
  Alejandro Vigna-Gómez, **Sophie Lund Schrøder**, Enrico Ramirez-Ruiz, David R. Aguilera-Dena, Aldo Batta, Norbert Langer, Reinhold Willcox
  APJl, Volume 920, Issue 1, id.L17, 12 pp.. arXiv:2106.12381.

Abstract

Compact binaries allow us to study many spectacular and fantastic astrophysical phenomena. The evolution of massive stars in binaries is filled with interesting, open questions that we are just now beginning to be able to answer. The aim of this thesis has been to investigate the evolution of compact binary stars to gravitational wave sources via hydrodynamical simulations of interacting stellar binaries.
The thesis is organised in three main parts.

In part I, we present models for merger-driven explosions that arise after the merger between a star and compact object following a common envelope event. In the merger accretion onto the compact object produces a neutrino-cooled a disk, and the envelope material is expelled into the surrounding environment, forming a dense circum stellar medium. This event is accompanied by the release of approximately 10^{51} erg into the surrounding medium, leading to an explosion with a light curve shaped by the merger-produced circum stellar medium.

In part II, we explored the effect on LIGO sources of forming the second compact object in a fallback supernova. We found that the observed black hole systems with smaller $\mathcal{M}$ and positive $\chi_{\rm eff}$ could be formed in fallback supernova. And we propose that GW200115,a black hole neutron star system, was formed in a fallback supernova. Its neutron star has a mass is more massive than mean observed for Galactic binary neutrons stars, and its black hole has a mass close to the lower side of the black hole mass distribution, both of which are possible to form in fallback supernova of a helium star of 10.0 $M_\odot$ only depending on the supernova energy.

Finally, in part III we investigate the characteristics of an electromagnetic counterpart to a binary black hole merger after a fallback supernova. In a fallback supernova, the ejecta material settles in mini disks around each black hole and accretion continues. We predict that the accretion luminosity at time of merger is $\approx 10^{35}$ erg/s for systems formed in symmetric explosions, and can be an order of magnitude higher for systems formed in asymmetric supernova with kicks.

Dansk resumé

Observeringer af tætte dobbeltstjerner giver os mulighed for at studere nogle af de mest spektakulære fenomener i astrofysik. Store dobbeltstjerners evolution er fyldt med interessante og uafklarede spørgsmål, som vi kun er begyndt at kunne svarer på. Målet med denne afhandling er at undersøge tætte dobbeltstjerner, der udvikler sig til to sorte huller eller neutron stjerner ved hjælp af fluid simuleringer. Denne afhandling består af tre hoveddele.

I den første del præsentere vi modeller explosion fra kollisionen af en kæmpe stjerne og et sort hul eller en neutronstjerne. I kollisionen falder store dele af kæmpestjernens kerne ned i det sorte hul eller bliver optaget af neutronstjernen of danner en neutrino af kølet disk. Samtidig bliver de ydre lag af kæmpestjernen spredt rundt om kernen og det kompakte objekt. Kollisionen frigiver omkring 10^{51} erg ud i den spredte gas, hvilket et kraftigt lyssignal, hvor der er imprintet strukturen af de ydre lag af kæmpestjernen.

I den anden del forskede vi i hvordan svage supernova eksplosioner kan ændre på endelige parametre for LIGO objekter. Vores result blev at de dobbelt sorte huller med små værdier for $\mathcal{M}$ og positive værdier for $\chi_{\rm eff}$ kan formes med svage supernovaer. Vi foreslår desuden at GW200115, som blev udsendt i kollisionen mellem en neutronstjerne og et sort hul, også blev formet i en svag supernova. Neutronstjernens masse er højere end de fleste i vores galakse og det sorte huls masse er mindre end vores generelle forventninger til sorte hul masser. Det er muligt at forme begge disse komponent fra en 10.0 $M_\odot$ Helium stjerne i svag supernova.

Og i den sidste del undersøgte vi mulige observationer af kolliderende sorte huller,

hvor det sidste sorte hul er formet i en svag supernova. I en svag supernova falder noget af det ekploderende gas tilbage på de sorte huller og danner en mini disk rundt om hvert sorte hul. De sorte huller optager derefter gassen i diskene og udsender lys. Vi vurdere, at når de sorte huller efterfølgende kollidere vil de stadig udsende $\approx 10^{35}$ erg/s lysenergi, hvis supernova eksplosionen var helt symmetrisk. Hvis den derimod var assymetrisk og systemet fik en impuls i modsat retning kan lysudsendelse være en faktor ti højere.

Acknowledgements

Thank you to Enrico and all the amazing people in my foreign group for making work easy and fun: Anne, Brenna, Rosa, Ari, Xiaoshan, Sierra, Katie, Aldo, Andrea, Davide, Jane, Alejandro, Ilya, Morgan, Tassos, Jeff.
And thank you to my lovely local group for making it delightful to work at home as well - Charlotte, Nandita, Isabella, luca, Axel, Dan, Adriano, Matt, Jens, Cecilie.

Tak til min søde Nicklas for at støtte mig, lytte til mig og tro på mig. Og tak til mor, Mille, Julie og Marielle for at I lytter til alle mine brokkerier.

It is a giant amount of work to complete a PhD! Luckily I have received exceptionally large amounts of help along the way - both with academic tasks and tasks, that required quite a lot of personal growth for me. I am deeply grateful that I had amazing people around me for this part of my education.

Contents

Introduction

Assembly of binaries in the field

Stellar evolution has been studied for many years, but only recently has it been discovered that most stars actually are formed as binary stars or multiple star systems (Offner et al., 2022). When we model stellar populations and make statistical comparisons to observed populations, it is therefore necessary not only to understand how stars evolve as single stars, but also how interactions with companion stars effect the final population. Massive stars are of particular interest, as they are believed to play key roles in many aspects of astrophysics such as the reionization of the universe (Conroy & Kratter, 2012; Eldridge et al., 2017; Götberg et al., 2019; Götberg et al., 2020; Ma et al., 2016; Rosdahl et al., 2018), nucleosynthesis of heavy elements (Dray & Tout, 2003; Izzard et al., 2006; Langer, 2012; Woosley & Heger, 2007), and the diversity of observed supernovae (Eldridge et al., 2019; Eldridge et al., 2018; Eldridge et al., 2013; T. J. Moriya et al., 2017; Podsiadlowski et al., 1992; Tauris et al., 2015; Yoon et al., 2019; Yoon et al., 2017; Zapartas, Renzo, et al., 2021; Zapartas et al., 2019). A subset of these will be visible as X-ray binaries (Remillard & McClintock, 2006), double neutron stars (Tauris et al., 2017), short gamma-ray bursts (Berger, 2014; Woosley & Bloom, 2006), and gravitational-wave transients (LIGO Scientific Collaboration & Virgo Collaboration, 2019a; Mandel & Broekgaarden, 2022).

For massive stars 70% will exchange mass with their companion during their evolution (Sana et al., 2012). These interactions change the final masses, orbits and spins of the remnant or remnants.

0.1 SINGLE-STAR EVOLUTION

A star spends most of its life on the main sequence, where it is fusing hydrogen into helium in its core. During this time the star becomes more luminous while decreasing its effective temperature, T_{eff}.
For massive stars with masses above $\sim 8M_{\odot}$, phases of consecutive fusing in the core lead to the different phases of evolution. When the star runs out of Hydrogen in its core, it starts burning hydrogen in a shell around the core. This marks the end of the main sequence. The shell burning causes the star to expand on a thermal timescale and becomes a red giant star. When helium is ignited, the star contracts again and a phase of core-helium burning follows. This phase is much shorter than the main sequence, and after Helium is exhausted from the core a second giant phase begins.
For massive stars ensuing phases of core ignition and burning continues follows the second giant phase. Strong stellar winds are present both during the main sequence and later core burning phases, where large fractions of the star's mass is lost. And finally, massive stars with masses roughly between $8 - 25M_{\odot}$ end up exploding in core collapse supernova, where they eject most or all their envelope material and the a neutron star (NS) is formed. For even more massive stars, the explosion is not strong enough to eject all the envelope material, and the NS instead collapses under the weight of the envelope and forms a black hole (BH).

0.2 BINARY-STAR EVOLUTION

Here I will go through a standard evolution of a binary in the field into a gravitational wave source. What follows is one of the generally accepted evolution paths, though as I will describe in sections 0.3.2, there are many uncertainties in this schematic.

Stars in binaries go through the same phases of fuel burning and expansions as single stars. But when a close companion is present, the phases of expansion lead to mass transfer between the stars, and often mass is also lost from the system all together. Figure 0.1 shows a schematic evolution of a binary, starting out with two massive stars of 38 and $34M_{\odot}$. The more massive star will reach the giant phase first. We will call this star the primary. Because the binary is close, the primary expands beyond the size of its own gravitational domain called its Roche Lobe (RL). The outer layers of the primary

are stripped from the primary and transferred onto the companion. The companion will accrete some of the material, but in most cases it will not accept all the gas from the primary, so some of the gas is lost from the system. This decreases the mass of the primary and increases the mass of the companion. Changes in the relative masses between the stars changes the orbital separation. In this case the mass ratio increases and therefore the separation also increases (see the derivation of this relation below). Following the first mass transfer, the primary goes through its remaining phases of burning fuel, until the star collapses into a black hole of $14M_{\odot}$.
When the companion reaches the giant phase and starts expanding, mass transfer is again initiated. In this case, the giant star is much larger than the primary, and the mass transfer makes the orbit shrink. The expansion eventually happens too fast compared to how quickly the primary BH can accrete the gas, and the system enters a phase of unstable mass transfer called the Common Envelope (CE) phase. In a CE phase the expansion of the giant star results in the orbit of the primary being inside the envelope of the companion. Now the material around the primary is very dense, and it causes a lot of friction on the primary's orbit in the form of gas drag. The gas drag effectively transforms orbital energy into kinetic energy in the envelope material, so the orbit of the primary and the core of the companion shrinks, while the envelope is ejected from the binary. This rapid contraction of the orbit is necessary to make the orbit tight enough to merge via gravitational-wave radiation within the age of the Universe.. But many of these encounters are also expected to result in the primary merging completely with the companion, and the explosive outcome of such a merger is described in 1.

After the CE phase, the binary consists of a black hole and Helium core star in a very tight orbit. Because the orbit is so compact, tidal effects are efficient and will spin up the Helium star and synchronize it with the orbit. When the companion collapses into a spinning BH, with the spin relating to the pre-collapse binary separation.
Both BHs are now formed. The orbit continues shrinking due to energy and angular momentum loss via gravitational waves, and the black hole binary will eventually merge into one black hole. The time until merger depends strongly on the separation after the CE phase, and therefore only systems with separations of a few tens of solar radii can merge and be observed as gravitational wave sources by LIGO.

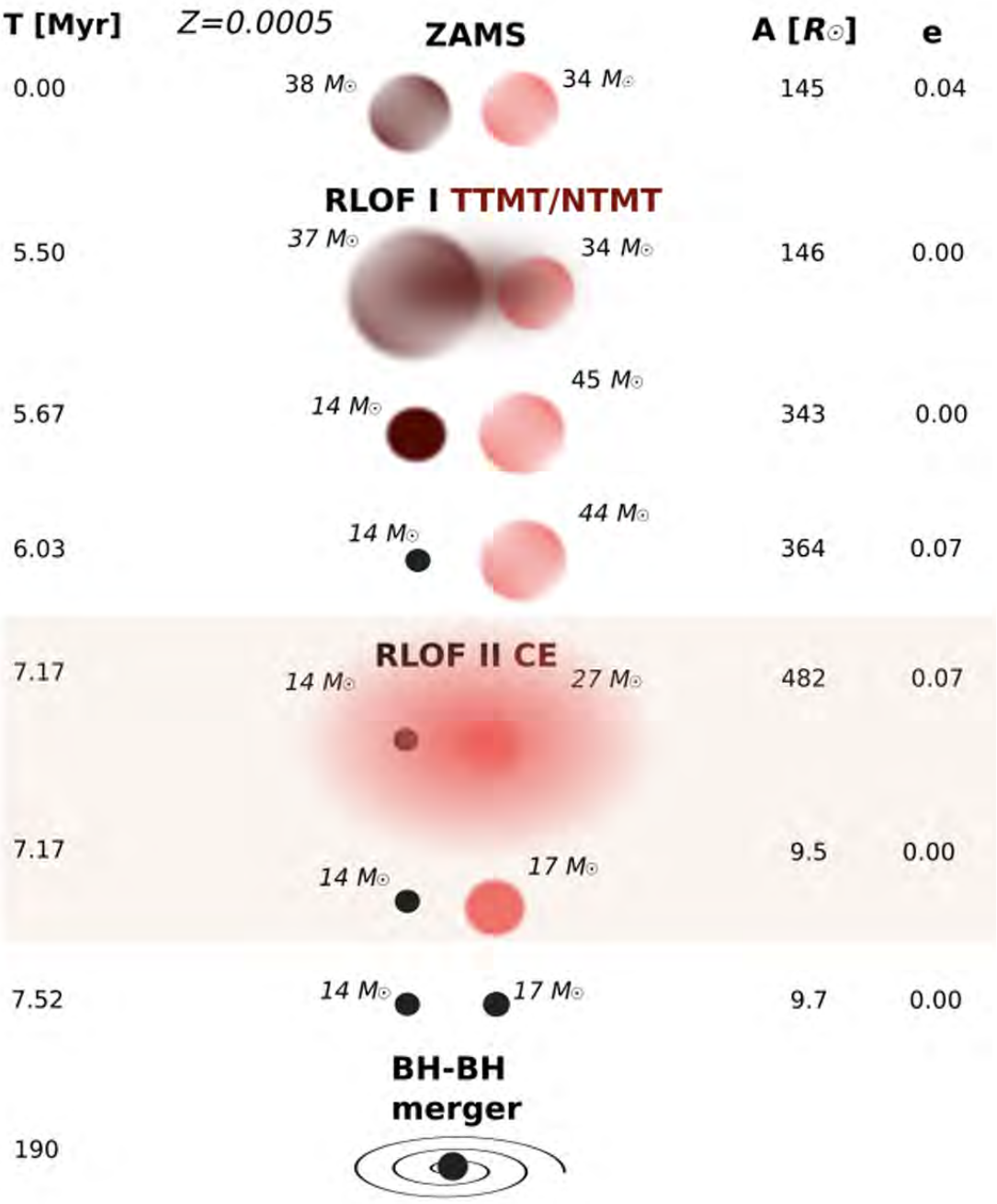

FIGURE 0.1 – Classical evolution of a stellar binary black hole system going through a phase of common envelope evolution. Figure modified from Belczynski et al. (2022)

0.3 BINARY ORBIT EVOLUTION DURING MASS LOSS

When stars evolve in binaries, multiple phases of mass and angular momentum loss change the orbit and the stars spins. Here I go through some of the analytical estimates of the phases in binary evolution, where the orbit is altered by the interactions between the stars.

0.3.1 Mass loss and torques

There are many types of mass loss and mass transfer in binary evolution. The simplest case is that of one star losing mass through a stellar wind.The companion accretes some of the gas and shapes the motion of the remaining material.
To simplify the problem we assume that the orbit is circular. Then we define the mass loosing star as m_d for donor star, and the accreting companion m_a for accreting star. The donor star is loosing mass at a rate $\dot{m}_d$. The companion accretes a fraction β of the mass lost from the donor, so $\dot{m}_a = -\beta \dot{m}_d$, which is a variable we can set in the analysis. The total angular momentum or the orbit is

$$J^2 = G\frac{m_d m_a}{m_d + m_a}a, \tag{1}$$

and by taking the total derivative, we can relate the changes in the binary to changes in the orbit

$$2\frac{\dot{J}}{J} = \frac{\dot{a}}{a} + 2\frac{\dot{m}_d}{m_d} + 2\frac{\dot{m}_a}{m_a} - \frac{\dot{m}_d + \dot{m}_a}{m_d + m_a}. \tag{2}$$

To understand the evolution of the orbit we need to keep track of changes in angular momentum. The angular momentum lost in the wind from the donor star is $\dot{J}_d = \dot{m}_d(r_d \times v_d)$, which is the angular momentum the gas had, while it was still part of the star. In a circular orbit the velocity of the star is always perpendicular to its radial vector, so we can drop the crossproduct and write $\dot{J}_d = \dot{m}_d\ r_d\ v_d$. $\dot{m}_d$ is per defintion negative when mass is lost from the donor star, so $\dot{J}_d$ is also negative.
Some of the angular momentum lost from the donor star will is retained by the system, when the companion accretes the gas. This adds a factor $\dot{J}_a$ to the total change. The angular momentum of the accreted gas will have changed as it moved across the Roche potential of the two stars, so this factor will have to be measured numerically.
The gas that is not accreted by the companion is left around the binary. Some of it is

focused in wakes behind the two stars, and these wakes exert drag forces on each object. This will transfer an angular momentum $\dot{J}_{drag}$ from the orbit to the wakes. How great this effect is depends on how much gas is present around the binary, and how fast the wind is moving. So this factor also has to be measured numerically, but is by definition negative. In total the change in angular momentum is $\dot{J} = \dot{J}_d + \dot{J}_a + \dot{J}_{drag}$.
We define the parameter α as the ratio of the specific angular momentum of material lost and the specific angular momentum of the binary

$$\alpha = \frac{\dot{J}}{\dot{m}_d + \dot{m}_a} \frac{m_d + m_a}{J} \tag{3}$$

Putting all this into equation 2, we get the orbit evolution:

$$\frac{\dot{a}}{a} = -2\frac{\dot{m}_d}{m_d}\left[1 - \beta\frac{m_d}{m_a} - (1-\beta)\left(\alpha + \frac{1}{2}\right)\frac{m_d}{m_d + m_a}\right] \tag{4}$$

$\dot{m}_d$ is negative, so if the sum in parentheses is negative too, $\dot{a}$ must be positive and the orbit will widen. If the paranthesis is positive, $\dot{a}$ will be negative and the orbit will shrink.

Equation 4 is the general equation for orbital changes in binaries when mass and angular momentum is transferred or ejected. It is useful to look at specific values for $\dot{a}/a$ under given physical setups.
First let us consider conservative mass transfer. This is the case when mass is transferred perfectly from one star to the other, without any mass being ejected so $\dot{m}_a = -\dot{m}_d$. This also means that no angular momentum is lost, so $\dot{J} = 0$. Then equation 4 simplifies to

$$\frac{\dot{a}}{a} = 2\left(\frac{m_d}{m_a} - 1\right)\frac{\dot{m}_d}{m_d} \tag{5}$$

Again $\dot{m}_d$ is negative, so if the sum in parentheses is positive, $\dot{a}$ must be negative, and the orbit will shrink. This is the case when $m_d > m_a$. If $m_d < m_a$, then $\dot{a}$ must be positive and the orbit will widen. This means that the separation will shrink until $m_d = m_a$. On the other hand, this means that a mass loss resulting in a greater difference in mass between the two star will result a wider orbit.

Another likely situation is the perfect loss of mass in a stellar wind, where mass is ejected from one star without interacting further with the binary. This type of mass loss

is called the fast mode or Jeans mode of mass loss. In this setup $\dot{m}_a = 0$ and while the mass lost from the donor is $\dot{m}_d$. The only angular momentum loss is that carried by the material ejected. It has the angular momentum of the donor star with $\dot{J}_d = \dot{m}_d r_d v_d$, and so $\alpha = \frac{m_2}{m_1}$. This simplifies equation 4 to

$$\frac{\dot{a}}{a} = -\frac{\dot{m}_d}{m_d + m_a} \tag{6}$$

Because m_d is negative, $\dot{a}$ is positive, so the orbit expands proportionally to the amount of mass lost.

It should be noted here that both these examples are simplifications. A perfectly conservative mass transfer is hard to imagine, because the accreting star has to readjust and actually absorb the oncoming mass. But the incoming mass is hot and the pressure balance is likely to push material out of the gravitational well of the accretor. The more correct orbit evolution includes an angular momentum and mass loss from the system. The wind mass loss is also a simplification, as it assumes that the wind material leaves the system with only the angular momentum it had when ejected from the surface of the donor star. After the mass has left the surface, it still has to pass outside of the potential of the binary, and will be affected by the gravitational forces. These forces will redistribute the material into an asymmetric ambient medium, with wakes behind the stars of high density material. These wakes in turn have a gravitational pull on the stars, which acts as a gravitational drag on the binary. This invokes an extra angular momentum loss term, counteracting the directly proportional expansion due to mass loss.

0.3.2 Instantaneous mass loss in binaries

When a supernova occurs in a binary, the ejection of mass from the exploding star happens on timescale much shorter than the orbit, and it can to first order be approximated as an instantaneous mass loss. Each star is assumed as a point mass moving in a circular orbit around their center of mass (CoM). The exploding star has mass M_1 and velocity v_1, and the companion has mass M_2 and velocity v_2. After the supernova the remnant has a mass M_{1f}, and the change in mass in the system is

$$\Delta m = M_1 - M_{1f} \tag{7}$$

and is it is useful to define mass loss ratio, $\tilde{m}$

$$\tilde{m} = \frac{M_1 + M_2}{M_{1f} + M_2} \tag{8}$$

To begin with I will assume that the explosion is symmetric, so no supernova kick is added to the binary. Hereafter everything in the final orbit is denoted with a subindex $_f$, and everything in the original orbit has no marker.

Because the ejection of mass happens instantly, the remnant and the companion continue orbiting each other with the same velocities. But because of momentum conservation, the whole system starts moving at velocity

$$\begin{aligned} \vec{p}_{\mathrm{CoM}} &= \Delta\vec{p}_{\mathrm{M}_1} + \Delta\vec{p}_{\mathrm{M}_2} \\ \vec{v}_{\mathrm{CoM}}(M_{1f} + M_2) &= M_{1f}\vec{v}_1 - M_1\vec{v}_1 \\ \vec{v}_{\mathrm{CoM}} &= \frac{-\Delta M\vec{v}_1}{(M_{1f} + M_2)}. \end{aligned} \tag{9}$$

From this we can see that the system will start moving in opposite direction of v_1.

In the new CoM frame the total energy at the moment of the supernova explosion is

$$E_f = -\frac{GM_{1f}M_2}{a} + \frac{1}{2}M_{1f}v_1^2 + \frac{1}{2}M_2v_2^2 = -\frac{GM_{1f}M_2}{2a}(2 - \tilde{m}) \tag{10}$$

Now we can use the energy equation to derive analytical restrictions on the post supernova orbit.
First we derive the condition for the orbit to stay bound. If the system is to remain bound, the total orbital energy has to be negative after the mass loss. Looking at equation (10), this implies that the term in parenthesis is greater than zero, so that the final binary mass is more than half the initial mass

$$\frac{1}{2}(M_1 + M_2) < (M_{1f} + M_2). \tag{11}$$

We can also derive the new semimajor axis by using the virial theorem saying that the total orbital energy of a bound orbit is $E_f = -\frac{GM_{1f}M_2}{a_f}$. Compared to equation 10 we get

$$a_f = \frac{a}{2 - \tilde{m}} \tag{12}$$

and the period of the binary can be derived from Kepler's third law

$$P_f = \frac{P}{(2-\tilde{m})^{3/2}} \tag{13}$$

The final orbit's total angular momentum is

$$L_f = \mu_f a v_{\text{orb}} \tag{14}$$

where $\mu_f = \frac{M_{1f}M_2}{M_{1f}+M_2}$ is the reduced final mass. The new orbit has excess kinetic energy, so the orbit is eccentric:

$$\begin{aligned} e &= \sqrt{1 + \frac{2E_f L_f^2}{(G[M_{1f}+M_2])^2 \mu_f^3}} \\ &= \tilde{m} - 1 \end{aligned} \tag{15}$$

From equations (12),(13) and (15), we see that the orbit grows further apart with higher mass loss. With $\tilde{m} = 2$ the semi-major axis goes to infinity because the system becomes unbound, and the value of the eccentricity becomes greater than one.

Now Galactic pulsars have been observed to move with large proper motions (Arzoumanian et al., 2002; Beniamini & Piran, 2016; Gunn & Ostriker, 1970; Hansen & Phinney, 1997; Lyne & Lorimer, 1994; Verbunt et al., 2017). The large velocities are attributed to an asymmetric supernova explosions, which causes the remnant too recoil in the opposite direction and impart a supernova kick. The exact mechanism is still uncertain, but current guesses are either hydrodynamical effects (Burrows & Hayes, 1996; Janka & Mueller, 1994; Wongwathanarat et al., 2013) or neutrino emission (Bisnovatyi-Kogan, 1993; Nagakura, Morinaga, et al., 2019; Socrates et al., 2005; Woosley, 1987).
The equations are more complicated when the supernova is non-symmetric because the kick is not necessarily in the orbital plane of the orbit. In phase space, $\vec{v_k}$ is given by

$$\vec{v_k} = \begin{bmatrix} v_k \cos\theta \cos\phi \\ v_k \cos\theta \sin\phi \\ v_k \sin\theta \end{bmatrix}. \tag{16}$$

where v_k is the magnitude of the kick vector. It is also helpful to define the relative kick velocity to orbital velocity $\tilde{v} = \frac{v_k}{v_{\text{orb}}}$. Brandt and Podsiadlowski (1995) derive the new

orbital parameters, where the new semi-major axis is

$$a_f = \frac{a}{[2 - \tilde{m}(1 + 2\tilde{v}\cos\phi\cos\theta + \tilde{v}^2)]}, \tag{17}$$

the new orbital period is then given by

$$P_f = \frac{P}{[2 - \tilde{m}(1 + 2\tilde{v}\cos\phi\cos\theta + \tilde{v}^2)]^{3/2}}, \tag{18}$$

and the new eccentricity is

$$e_f^2 = 1 - \tilde{m}\Big[2 - \tilde{m}(1 + 2\tilde{v}\cos\phi\cos\theta + \tilde{v}^2)\Big]\Big[(1 + \tilde{v}\cos\phi\cos\theta)^2 + (\tilde{v}\sin\theta)^2\Big] \tag{19}$$

Some important limits can again be found from these equations. The strongest kick allowed for an orbit to remain bound is in the exact opposite direction of the orbital motion. And for systems kicked in the right direction, higher mass loss is possible, because the kick will effectively force the system back into a bound orbit. It can even make the orbit smaller than it was before the supernova occured, if it is strong enough. This is relevant for compact object mergers, as it changes the GW merging time. The fraction of systems evolved in binary population studies that merge within a Hubble time will change depending on the assumptions behind kick velocities, and the therefor the parameter space for LIGO source progenitors.

OPEN QUESTIONS IN BINARY EVOLUTION

In this section I will present the outstanding questions in the field of binary evolution that I have worked on during my PhD.

0.4 COMMON ENVELOPE SN

Binary evolution consists of many phases, though in general the timescales are too long to actually observe populations of binaries evolving. Instead we can use theory to predict observable signatures, which then can be used to estimate numbers of objects and derive the rates of evolving binaries. One of the phases that could give a luminous signal is the CE phase, where a giant star expands and engulfs the orbit of its companion. At the onset of this interaction, some of the outer envelope material is ejected. This

phase has been suggested to be the source of the optical or infrared transients called red novae (Ivanova, Justham, Chen, et al., 2013; MacLeod, Macias, et al., 2017; Metzger et al., 2012; Soker & Tylenda, 2006). If the CE phase ends with the two stars merging, a stronger signal is possible in the form of a mergerinduced explosion or a CE jet supernova (Dong et al., 2021; Gilkis et al., 2019; Grichener & Soker, 2019; Soker & Gilkis, 2018; Soker et al., 2019). In a CE merger the hydrodynamical drag on the compact object companion causes the companion to sink all the way to the core of the donor star. Here the compact object will tidally disrupt the core of the giant star, from which material forms a rapidly accreting neutrino-cooled disk. The rapid accretion liberates energy of the order $\sim 10^{53}$ ergs. Most of this energy is emitted as neutrinos, but a fraction is emitted as mechanical energy in the form a jet or strong disk winds. Depending on exact densities and assumed efficiency, the amount of mechanical energy released is of the order 10^{50} to 10^{52} ergs.

0.4.1 Supernovae interacting with circumstellar material

The many variations seen in the light curves from type II supernovae likely originate from the supernova shock hitting dense circum stellar material (CSM) (Chevalier & Irwin, 2011; Chugai, 1997, 2001; Chugai & Danziger, 1994; Chugai et al., 2004; Dessart et al., 2015; T. J. Moriya, Blinnikov, et al., 2013; Morozova et al., 2017; Ofek, Fox, et al., 2013; Smith & McCray, 2007). Specifically type IIn supernova are known to come from interactions with CSM, as they have narrow emission lines from slow moving material in their spectra (Kiewe et al., 2012; Taddia et al., 2013). The origin of the CSM is still unclear. Possible origins include late stage stellar winds or an outburst of gas from the star just prior to explosion (Fuller, 2017; Quataert & Shiode, 2012; Shiode & Quataert, 2014) or the formation of a disk like structure around the star (J. E. Andrews & Smith, 2018; McDowell et al., 2018). It is also likely that binary interactions and mass transfer between the stars could lead to dense CSM (Smith, 2014).

The interaction with a CSM changes the supernova light curve in the following way. An amount of energy ΔE is transformed from kinetic to internal energy in the supernova ejecta, when it is sweeping up a thin shell of CSM,

$$\Delta E \approx \frac{dM_{\rm CSM}}{M_{\rm tot}} E, \tag{20}$$

where $M_{\rm tot}$ is the sum of the supernova ejecta and the swept-up CSM mass, $dM_{\rm CSM}$ is the CSM shell mass, and E is the kinetic energy of the supernova ejecta.

When this addition of internal energy happens in an optically thin region, all of the internal energy is radiated, and $\Delta E_{\rm rad} \approx \Delta E$. But if the CSM shell lies within the photosphere radius, which is an optically thick region, the heated ejecta will instead continue to expand. The gas internal energy will then decay along an adiabat, until it has become optically thin and is free to radiate. When the gas pressure is dominated by radiation with $P \propto \rho^{4/3}$, then we can assume that the gas specific internal energy decays adiabatically as r^{-1} in optically thick regions, and

$$\Delta E_{\rm rad} \approx (r/R_{\rm ph})\Delta E. \tag{21}$$

Combining the two above equations, we can get the extra radiated energy from SN ejecta, when it is interacting with CSM within the photosphere radius

$$\frac{dE_{\rm rad}}{dM_{\rm CSM}} \approx \frac{E}{M_{\rm tot}}\frac{r}{R_{\rm ph}}. \tag{22}$$

But the CSM is rarely just a thin shell, and more likely an area of material distributed between the pre-SN radius of the star R_* and the photosphere radius $R_{\rm ph}$. To get an estimate of the total energy radiated from CSM interaction, we can integrate the expression above over radius. To simplify we will assume that E is constant. This is justified only when $M_{\rm CSM} \ll M_{\rm tot}$ and $E_{\rm rad} \ll E$. If these conditions are not met, the loss in kinetic energy to thermal energy or radiation must be included. We then replace $dM_{\rm CSM} = 4\pi r^2 \rho dr$, where ρ is the CSM density, to write

$$\begin{aligned}\frac{E_{\rm rad}}{E} &\approx \int_{R_*}^{R_{\rm ph}} \frac{r}{R_{\rm ph}}\frac{4\pi r^2 \rho}{M_{\rm tot}} dr, \\ &\approx \frac{4\pi}{R_{\rm ph} M_{\rm tot}} \int_{R_*}^{R_{\rm ph}} \rho r^3 dr.\end{aligned} \tag{23}$$

This integral shows that the density distribution $\rho(r)$ is critical in determining the CSM contribution to the radiated luminosity and the SN lightcurve. Lightcurves seen from some type II SN have material very close to the surface of the star. This CSM is hard to explain with winds or a mass outburst, as it would be moving to fast and already be further away from the star by the time of explosion. Instead in chapter 1 I present my work on explosions from stellar mergers inside a CSM created by a CE event. The CE event has slow moving CSM, which has left the star gradually right up until the time of the explosion, resulting in a very close and dense CSM.

0.5 FALLBACK SUPERNOVA IN BINARIES

The mechanism of core collapse supernova is still not well understood (Burrows & Vartanyan, 2021). A successful explosion would result in a complete ejection of the outer envelope leaving behind a NS, while an unsuccessful explosion has energies lower than the binding energy of the star, and results in an implosion with the formation of a BH. In general stars below $20M_\odot$ are expected to have successful explosions and form NSs, while stars above $20M_\odot$ have unsuccessful explosions and form BHs.

However, new studies show that whether the explosion is successful or not is harder to determine than expected and not just a function of the initial mass (Ertl et al., 2016; Nakamura et al., 2015; Sukhbold & Adams, 2020; Sukhbold & Woosley, 2014; Ugliano et al., 2012). Parameters such as the "compactness parameter" (O'Connor & Ott, 2011) have been tested, but O'Connor and Ott (2011) and Ugliano et al. (2012) and Sukhbold and Woosley (2014) have showed that processes in the late burning stages change the outcome. Instead there seem to be 'islands of explodability' in ranges of masses, and the effect seems to be stronger for stars that have been stripped of their hydrogen envelopes, which is expected during binary evolution (Ertl et al., 2020; Laplace et al., 2021; Mandel et al., 2021; Schneider et al., 2021).

Despite the difficulties in predicting the final outcome of core collapse, to do binary populations studies it is necessary to have an analytical prescription to predict remnant masses quickly. Three models are shown in figure 0.2.

Originally stellar evolution expected there would be a gap in remnant masses between the smallest observed BH of $\sim 5M_\odot$ and the most massive NS of $\sim 2.1M_\odot$. This is shown in the Rapid SN model from Fryer et al. (2012). But observations of parameters of merging GW binaries from the LIGO collaboration have started to fill in this gap (The LIGO Scientific Collaboration et al., 2021). Today a common way of treating the formation of a black hole in binary population studies is the delayed core-collapse SN model from Fryer et al. (2012), where the remnant black hole mass is related to the final carbon-oxygen core mass of the star. New models such as Mandel and Müller (2020) have a more sophisticated approach, where the compact object masses and kicks are stochastic distributions with possible NS and BH formation for the same stellar

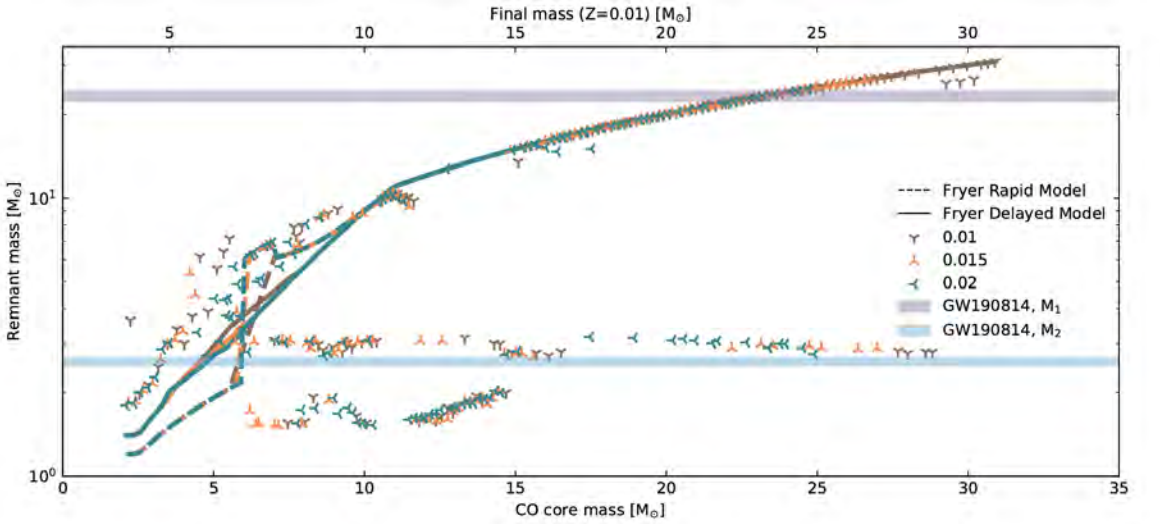

FIGURE 0.2 – Different models comparing initial stellar mass with remnant mass. Figure modified from Antoniadis et al. (2022).

parameters. These models have the advantage of filling the lower mass gap between NS and BH (Belczynski et al., 2012; Zevin et al., 2020) and matching the LIGO observations better.

To form smaller BHs these newer models all have partial explosions, where some mass collapses directly onto the BH and some mass is ejected from the system. For simplicity these two mass components are treated as being completely separated in binary populations studies for simplicity, but the SN shock actually impose ranges of velocities in the stellar envelope (Ertl et al., 2020). Material with velocities moving above the escape velocity will be ejected from the system, but material with velocities below the escape velocity will expand before collapsing onto the remnant **cite Aldo**. For a single star the expansion does not have an effect, but in the case of a binary, where a companion is present close by, the expansion causes extra drag and torque on the binary. This will alter the amount of gas and angular momentum accreted by the two stars and it changes the post SN orbital parameters, both of which will change the final properties expected for merging GW sources. This is a purely hydrodynamical effect, which is why it is so important to model these interactions using 3D simulations.

When we want to model a binary system that undergoes a supernova explosion, we can make some simplifying assumptions to get analytical estimates. In the next two sections I will go through how LIGO's GW observations of BH spins can help us

pinpoint improved supernova prescriptions.

0.5.1 Spin from LIGO sources

BHs are described by only two parameters on their own, their mass and their spin. The two main parameters LIGO measures of GW events are forms of these two parameters for binaries. As the mass combination called the Chirp Mass $\mathcal{M}$ and the BH spins projection along the orbital angular momentum $\chi_{\rm eff}$. $\mathcal{M}$ is given by

$$\mathcal{M} = \frac{(M_1 M_2)^{3/5}}{(M_1 + M_2)^{1/5}} \tag{24}$$

where M_1 and M_2 are the masses of the two compact objects. And $\chi_{\rm eff}$ is given by

$$\chi_{\rm eff} = \frac{M_1 \mathbf{a_1} + M_2 \mathbf{a_2}}{M_1 + M_2} \hat{L} \tag{25}$$

where $\hat{L}$ is the normal vector or the orbital angular momentum of the binary and $\mathbf{a_1}$ and $\mathbf{a}_2$ are the spin vectors of the two compact objects. $\chi_{\rm eff}$ is positive, when the combined spins of the compact objects are aligned with the orbital angular momentum vector, and negative when misaligned. The spins can also result in $\chi_{\rm eff} = 0$ if they are in opposite directions and/or perpendicular to the orbital angular momentum vector. Figure 0.3 shows the credibility regions of the events measured so far by LIGO.

Given these two parameters, astronomers try to discover the origin of the merging population. Different formation channels are expected to have different mass and spin distributions. Two of then are the field formation channel that I gave an overview of in section 0.2, and the dynamical assembly in clusters of stars such as globular clusters. In dynamical assembly the high density of stars leads to gravitational captures and ejections from the cluster, and the process is governed by the dynamical and chaotic interactions of multi-body systems. Stars collapse to BHs and NSs and have whatever spin the star had at collapse. The black holes enters and exits multiple gravitationally bound orbits before having a strong enough encounter to be ejected from the cluster. The result is that the expected spins of binary black holes formed in dynamical assembly have completely random directions compared to the orbital spin, and so the these systems are expected to form a Gaussian distributions of $\chi_{\rm eff}$ around zero. In field formation the angular momentum of the final BHs and NSs come mostly from the orbit,

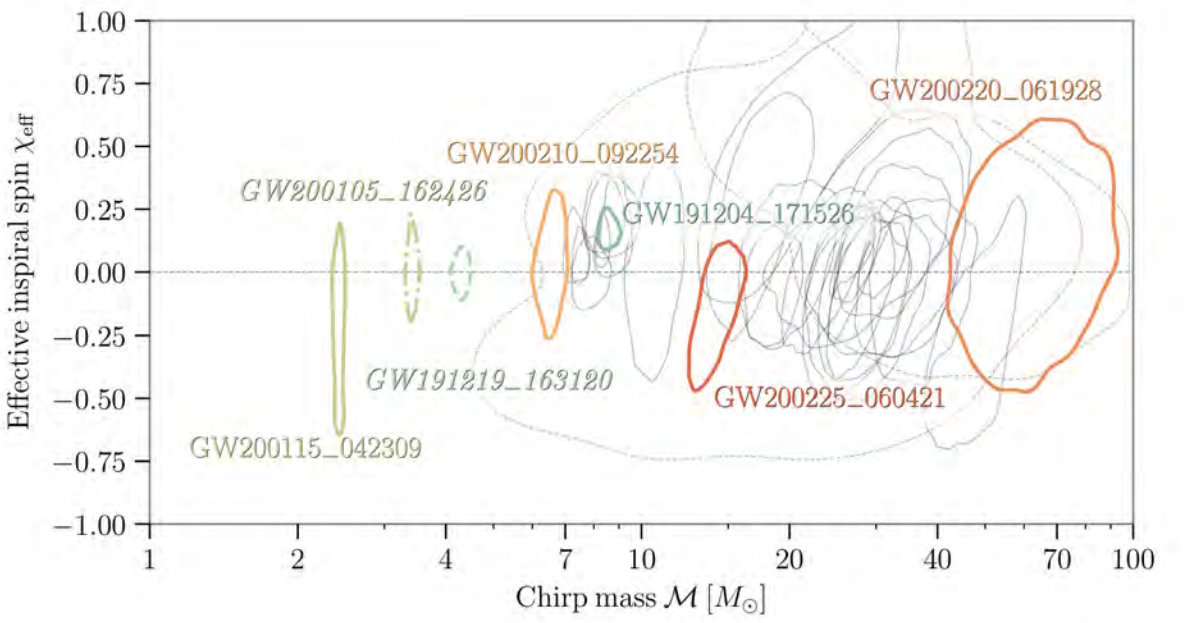

FIGURE 0.3 – Parameters of merging binaries from GW observations from LIGO. Shown are the credibility region contours of the Chirp mass $\mathcal{M}$ and $\chi_{\rm eff}$. Figure modified from https://arxiv.org/pdf/2111.03606.pdf

through mass transfers and tidal torques. The spins of these systems are therefore expected to be more aligned with the orbit and have positive values of $\chi_{\rm eff}$.

Given that we only can measure the masses and spins of GW sources, it is important to get their expected values as correct as possible to distinguish their origin.

0.5.2 Spin evolution for disk accretion on black holes

When black holes accrete mass from their surroundings, they accrete not only the material, they also accrete the angular momentum of this material, which adds to the spin of the black hole.

A black hole with angular momentum J and mass M has a spin value defined as

$$a = \frac{cJ}{GM} \tag{26}$$

where c is the speed of light and G the gravitational constant. The value of a is limited by general relativity and can vary from 1 to −1.

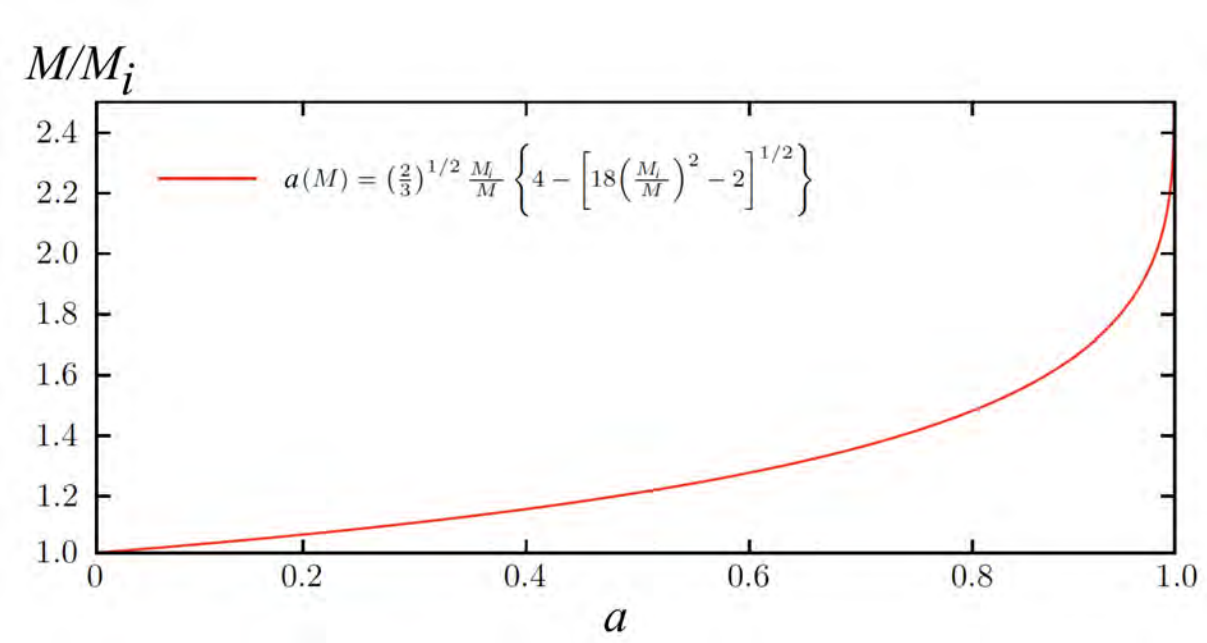

FIGURE 0.4 – Spin evolution for disk accretion onto an black hole.

When a black hole is accreting from an accretion disk, the angular momentum of the accreted material is equal to that of the innermost stable circular orbit (ISCO) with orbit radius r_{ISCO}.

The value of r_{ISCO} depends on the black hole spin. To get the spin as function of accreted mass, one needs to both evolve the spin parameter, mass of the black and r_{ISCO}. Bardeen (1970) and Bardeen et al. (1972) found that the spin of a black hole accreting from a mass at the innermost stable orbit follows

$$a = \left(\frac{2}{3}\right)^{1/2} \frac{M_i}{M} \left\{4 - \left[18\left(\frac{M_i}{M}\right)^2 - 2\right]^{1/2}\right\} \tag{27}$$

This function can be seen plotted in figure 0.4. The amount of mass accreted to achieve a certain spin value is always a fraction of the initial BH mass. This means that the final spin of a BH strongly depends on the angular momentum the collapsing material from the star before formation

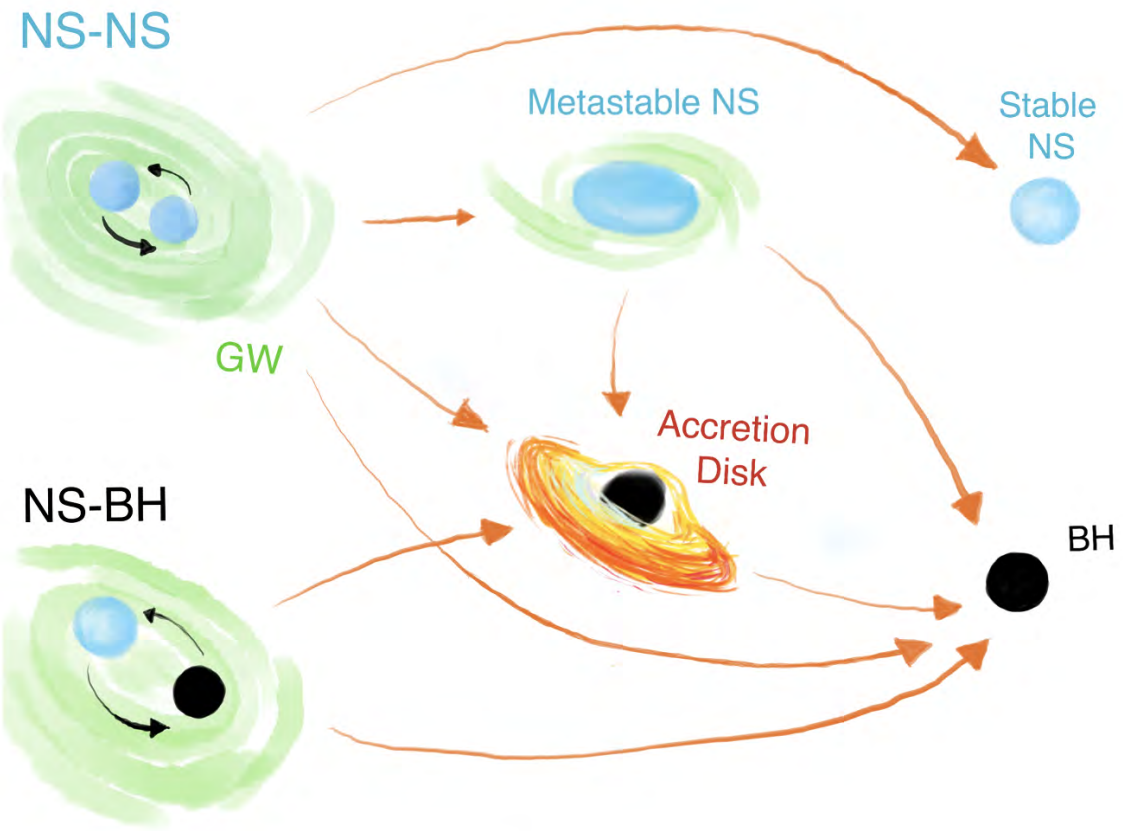

FIGURE 0.5 – The formation of accretion disks and ejecta giving rise to an electromagnetic emission from mergers of NSs and BHS. Figure modified from **Ascenzi et al 2021**

0.6 LIGO AND COUNTERPARTS

The field of observational astronomy has evolved and the onset of large-scale, spatially and temporally systematic surveys are revealing new fascinating transients. But one of the uncertain and highly sought pieces in gravitational-wave astronomy is still missing: an electromagnetic counterpart to a binary black hole merger.

Multimessenger astronomy has already achieved a great victory with the observations of the NS merger GW170817 (LIGO Scientific Collaboration, Virgo Collaboration, & Burns, 2017). GW170817 was not only the first NS merger detected by LIGO, its jet was also detected in γ-rays as a short γ-ray burst (GRB), and light was detected across the frequency spectrum in the following kilonova event (Coulter et al., 2017).

However, GW170817 is also the only event so far for which an accompanying electromagnetic signal has been confirmed (Coulter et al., 2017; Hallinan et al., 2017; Kasliwal et al., 2017; LIGO Scientific Collaboration & Virgo Collaboration, 2017c; LIGO Scientific Collaboration, Virgo Collaboration, & Burns, 2017). The other types of compact object mergers LIGO can detect are that of a BH and NS (BHNS) or binary BHs (BBHs) mergers.

A short GRBs could be produced by a BHNS merger (Foucart, 2021), as the requirement for an electromagnetic signal is that there is gas present around the binary at the time of merger. Though in the case of a too high mass BH, the NS will be swallowed whole and never emit any light. See figure 0.5 for a schematic overview. No emission from a NSBH merger has been detected so far, but the search is ongoing (Raaijmakers, Nissanke, et al., 2021).

A γ-ray transient was observed temporally coincident with the GW150914 BBH merger (Connaughton et al., 2018; Connaughton et al., 2016). Mergers from BBHs are not expected to produce an electromagnetic signal, because there is no gas available from the BHs themselves. The only way a BBH merger can result in a signal, is if there is material around the BHs at time of the merger. But general-relativistic magnetohydrodynamic simulations have revealed that jets are produced from merging black holes if there is matter around the BHs at the time of merger (Khan et al., 2018). The density and amount of surrounding gas determines the strength of any electromagnetic signal. GW150914 sparked a large interest in the community and a large amount of work has been done on possible ways to have gas present at the time of the merger. Suggestions include charged BHs (Fraschetti, 2018; Liebling & Palenzuela, 2016; B. Zhang, 2016), mergers in AGN disks (Bartos et al., 2017; Graham et al., 2020; N. C. Stone et al., 2017) or circumbinary disk remnant from field evolution (de Mink & King, 2017; Kotera & Silk, 2016; Martin et al., 2018; Murase et al., 2016; Perna et al., 2019; Perna et al., 2016).

0.6.1 Emission of light from merging black holes

The field formation of binary black holes includes many phases of mass loss, where gas is ejected from the binary and is expected to remain close by. This way two mini disks or a circumbinary disk can be formed. The binary black hole progenitors shed mass

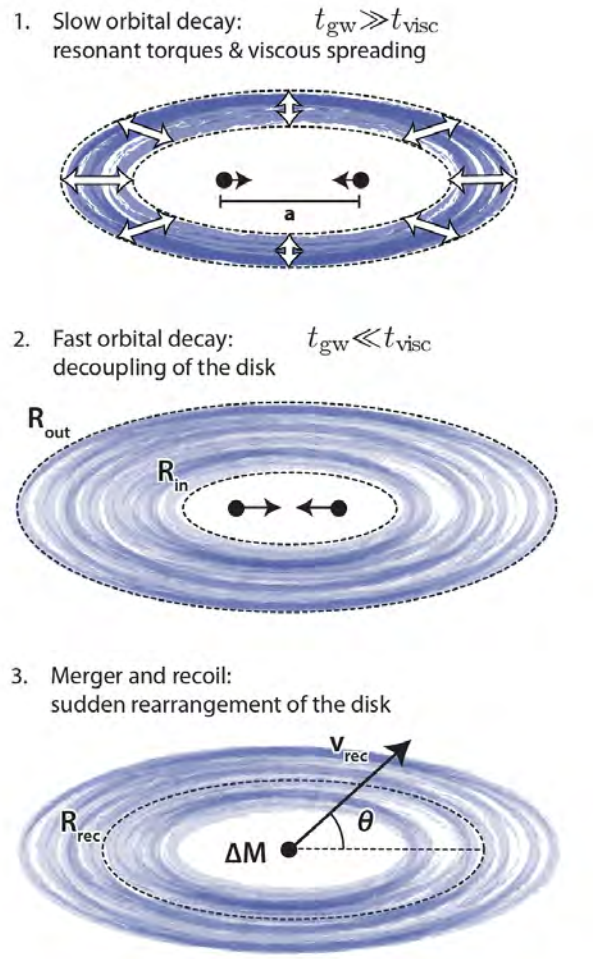

FIGURE 0.6 – Schematic of an EM signal from a BHBH merger. Figure modified from de Mink and King (2017).

through phases of stellar winds (Vink, 2007), a CE phase (Ivanova, Justham, Chen, et al., 2013) and in weak SN explosions or even in direct collapses (Fryer et al., 2006; Lovegrove & Woosley, 2013). The wind velocities are likely quite high and will escape the system. But a CE phase or weak SN explosion have material with velocities comparable to that of the orbit, which will not escape and could instead settle in a circumbinary disk.

After the formation of the second black hole, the possibility of an electromagnetic signal depends on two timescales; the viscous timescale of the disks, which determines how fast the gas is accreted by the black holes, and the inspiral timescale, which determines how fast gravitational waves shrink the black hole binary. If a circumbinary disk has

been formed, the scenario likely follows the cartoon shown in figure 0.6. In step 1 the inspiral is slow compared to the disk, and most of the disk material is likely accreted. The timescale for inspiral is proportional to the binary separation cubed. This means that eventually the inspiral timescale will be shorter than the viscous timescale as shown in step 2, and the disk material still remaining at this point will also be there at the time of merger. In step 3 when the BH merger happens, there is an almost instantaneous reduction of the total gravitational mass, and an impulsive kick is added to the newly formed single black hole. This requires the disk to instantly rearrange itself, which results in strong internal shocks. This will reheat the disk and make the viscous timescale drop suddenly. The result is a flare of accretion emission from the new BH.
The amount of gas that could settle in disks initially and the ejecta velocities are highly uncertain. Generally around $\sim 1 M_{\odot}$ is expected after a weak fallback SN in the formation of the second BH. This is also the most promising source of remaining disk material, as the gas is not exposed to further energetic emission that could push the material away from the binary. But understanding the long term accretion rates and how much material remains in the disk at the time of merger, is important to determine to estimate how strong the emission will be and how likely we are to observe any electromagnetic signal in the future.

0.7 THESIS OUTLINE

In the previous sections, a concise, but informative, description of the current status of **bla bla** was presented. The main focus of this thesis is the **bla bla**. The following two chapters enclose an article and a letter appeared in peer-reviewed journals in the past years and months.

In Chapter **bla bla**, I will present a **bla bla** (see below).

In Chapter **bla bla**, I will shift the focus on t**bla bla**. In particular, I will revisit **bla bla** solution.

Finally, Chapter **bla bla** briefly describes future developments based on these two

works. In this Chapter, I will also present the introduction and main motivation, in addition to the preliminary analysis, of a parallel project **bla bla**.

I

Electromagnetic signals from Stellar mergers

CHAPTER 1

Common envelope mergers resulting in explosions

This chapter includes the following article:

"Explosions Driven by the Coalescence of a Compact Object with the Core of a Massive-star Companion inside a Common Envelope: Circumstellar Properties, Light Curves, and Population Statistics"

Published in The Astrophysical Journal (ApJ), 892, 1, id.13, 18 pp. (2020).

Authors: Sophie Lund Schrøder, Morgan MacLeod, Abraham Loeb, Alejandro Vigna-Gómez, Ilya Mandel.

ABSTRACT

We model explosions driven by the coalescence of a black hole or neutron star with the core of its massive-star companion. Upon entering a common envelope phase, a compact object may spiral all the way to the core. The concurrent release of energy is likely to be deposited into the surrounding common envelope, powering a merger-driven explosion. We use hydrodynamic models of binary coalescence to model the common envelope density distribution at the time of coalescence. We find toroidal profiles of material, concentrated in the binary's equatorial plane and extending to many times the massive star's original radius. We use the spherically-averaged properties of this circumstellar material (CSM) to estimate the emergent light curves that result from the interaction between the blast wave and the CSM. We find that typical merger-driven explosions are brightened by up to three magnitudes by CSM interaction. From population synthesis models we discover that the brightest merger-driven explosions, $M_V \sim -18$ to -20, are those involving black holes because they have the most massive and extended CSM. Black hole coalescence events are also common; they represent about 50% of all merger-driven explosions and approximately 0.25% of the core-collapse rate. Merger-driven explosions offer a window into the highly-uncertain physics of common envelope interactions in binary systems by probing the properties of systems that merge rather than eject their envelopes.

1.1 INTRODUCTION

Binary and multiple systems are ubiquitous among massive stars. Of these systems, a large fraction are at separations so close that they will interact over the stars' lifetimes (de Mink et al., 2014; Moe & Di Stefano, 2017; Sana et al., 2012). As these multiple-star systems evolve to leave behind compact object stellar remnants, the stage is set for interactions between the evolving stars and the stellar remnants. In some cases, a phase of escalating, unstable mass transfer from a massive star donor onto a compact-object companion leads to a common envelope phase (Paczynski, 1976), in which the compact object is immersed within the envelope of the massive star and spirals closer to the massive star's core (e.g. Armitage & Livio, 2000; De Marco & Izzard, 2017; Iben & Livio, 1993; Ivanova, Justham, Chen, et al., 2013; Taam et al., 1978; Taam & Sandquist, 2000; Terman et al., 1995).

Common envelope interactions can lead to either the ejection of the shared, gaseous envelope and a surviving, binary pair or to the merger of the donor star core with the companion. The distinction between these cases for a given binary remains highly uncertain, but is of significant interest given its importance (e.g. J. J. Andrews et al., 2015; Belczynski et al., 2002; Belczynski et al., 2008; Kalogera et al., 2007; Kalogera et al., 2004; Tauris et al., 2017; Vigna-Gómez et al., 2018), for example, to estimating rates of compact object mergers and associated gravitational-wave transients (LIGO Scientific & Virgo Collaboration, 2017; LIGO Scientific Collaboration & VIRGO Collaboration, 2016; LIGO Scientific Collaboration & Virgo Collaboration, 2016b, 2017a, 2017c, 2019a, 2019b). In the case of massive stars interacting with lower-mass, compact object companions, the theoretical expectation is that only donor stars with the most-extended, weakly bound hydrogen envelopes are susceptible to ejection, while the remainder of systems are likely to merge (Kruckow et al., 2016).

What happens when a compact object merges with the helium core of a massive star? At least two possible outcomes have been suggested. Perhaps a neutron star embedded in a stellar envelope could burn stably, forming a Thorne-Zytkow object (Levesque et al., 2014; T. J. Moriya, 2018; Podsiadlowski, 2007; Podsiadlowski et al., 1995; Thorne & Zytkow, 1977). Alternatively, it is possible for the angular momentum of the merger to lead to the formation of a disk around the compact object (be it a neutron star or a black hole), from which material forms a rapidly accreting neutrino-cooled disk (Barkov & Komissarov, 2011; W.-X. Chen & Beloborodov, 2007; Chevalier, 1993, 1996, 2012; Fryer & Woosley, 1998; Fryer et al., 1996; Fryer et al., 2014; Fryer et al., 1999; Houck & Chevalier, 1991; Lee & Ramirez-Ruiz, 2006; MacFadyen & Woosley, 1999; MacFadyen et al., 2001; Popham et al., 1999; Song & Liu, 2019; W. Zhang & Fryer, 2001). Accretion of the surrounding core material liberates on the order of $\eta M_{\odot} c^2 \sim \eta 10^{54}$ erg, where η is an efficiency factor of order 0.1 (Frank et al., 2002). Much of this energy emerges in neutrinos, which stream freely away from the accretion object (Chevalier, 1993; Fryer et al., 1996; W. Zhang & Fryer, 2001). A fraction, however, emerges as Poynting flux or mechanical energy (either a disk wind or collimated outflow) and can feed back on the surroundings, powering a blast wave with energy similar to a supernova (Chevalier, 2012; Dexter & Kasen, 2013; Fryer & Woosley, 1998; Fryer et al., 2014; Gilkis et al., 2019; Soker, 2019; Soker et al., 2019; Song & Liu, 2019; W. Zhang & Fryer, 2001).

Chevalier (2012) observed that, in the case that the merger was initiated by a

preceding common envelope phase, the blast wave necessarily interacts with the dense surrounding medium of the common envelope ejecta (Gilkis et al., 2019; Soker, 2019; Soker & Gilkis, 2018; Soker et al., 2019). The resulting transient is described as a "common envelope jets supernova" by Soker et al. (2019). One of the key points that Chevalier (2012) and Soker et al. (2019) mention is that the distribution of common envelope ejecta is crucial in shaping the observed light curve (see Kleiser et al., 2018, for a similar discussion in the context of rapidly-fading supernovae). Here, we pursue this line of examination.

Light curves from supernova explosions of single stars within a dense circumstellar material (CSM) have been considered as the origin of the variations in type II supernova for many years (Chevalier & Irwin, 2011; Chugai, 1997, 2001; Chugai & Danziger, 1994; Chugai et al., 2004; Dessart et al., 2015; T. J. Moriya, Blinnikov, et al., 2013; Morozova et al., 2017; Ofek, Fox, et al., 2013; Smith & McCray, 2007), and even a population of objects that appear to transition from type I to type II (Margutti et al., 2017). Specifically type IIn, with their narrow line features, are known to be interacting with a slow moving CSM (Kiewe et al., 2012; Taddia et al., 2013). But the origin of the material around the pre-SN star is not yet clear. Ideas include late stage stellar winds or small outbursts of gas (Fuller, 2017; Quataert & Shiode, 2012; Shiode & Quataert, 2014) or formations of a disk-like torus (J. E. Andrews & Smith, 2018; McDowell et al., 2018). With this paper we add to the calculations by Chevalier (2012) the light curves expected from an engine-driven explosion inside a merger ejecta profile. We show how the atypical CSM distribution leads to light curves powered in part by CSM interaction, resembling type IIn and IIL and lacking a plateau phase (e.g. Das & Ray, 2017; Eldridge et al., 2018; Morozova & Stone, 2018).

We briefly review the engine-driven explosion model in 1.2. We then self-consistently model the circum-merger density distribution from the common envelope phase using a three-dimensional hydrodynamic simulation in Section 1.3. To explore the impact of this CSM on the resultant engine-driven explosions, we produce a number of spherically-symmetric radiative transfer models of blast waves interacting with the (spherically-averaged) common-envelope ejecta profiles in Section 1.4. Next, we map the expected populations of compact object–core mergers and their resultant transients in Section 1.5. Finally, in Section 1.6 we study the imprint of CSM on merger-driven explosions, compare to known supernovae, and discuss possible identification strategies. In Section

1.7 we conclude.

1.2 MERGER-DRIVEN EXPLOSIONS

1.2.1 Inspiral, Merger, and Central Engine

Following its inspiral through the common envelope, a compact object can tidally disrupt and merge with the helium core of the massive star (Chevalier, 2012; Soker & Gilkis, 2018; Soker et al., 2019; W. Zhang & Fryer, 2001). The disrupted material forms an accretion disk surrounding the now-central compact object. The local densities of more than 10^2 g cm^{-3} imply that accretion occuring on a dynamical timescale is very rapid of the order of 10^{-3} to $10^{-1} M_\odot$ s^{-1} (Fryer & Woosley, 1998; W. Zhang & Fryer, 2001), making these conditions very similar to those of a classical collapsar scenario of rapid accretion onto a newly formed black hole (MacFadyen & Woosley, 1999; MacFadyen et al., 2001; Siegel et al., 2019). Neutrinos mediate the bulk of the accretion luminosity at these accretion rates (MacFadyen & Woosley, 1999), so accretion can occur onto either neutron stars or black holes under these conditions (Fryer et al., 1996). At higher-still accretion rates, neutrino energy deposition can overturn the accretion flow (e.g. Pejcha & Thompson, 2012). This rapid accretion, over approximately the dynamical time of the core (W. Zhang & Fryer, 2001), 10^3 s, will lead a neutron star companion object to quickly collapse to a black hole.

These conditions of hypercritical accretion from the core onto an embedded black hole set the stage for an explosion powered by this central, accreting engine. In the context of collapsing helium stars stripped of their hydrogen envelopes, the result is a long gamma ray burst (GRB), in which a relativistic jet, perhaps powered by the coupling between the magnetic field in the accretion disk coupling to the rotational energy of the black hole (via the Blandford and Znajek (1977) process (e.g. Barkov & Komissarov, 2008)) tunnels out of the helium star and is accelerated to high Lorentz factor (MacFadyen & Woosley, 1999; MacFadyen et al., 2001).

In the context of a helium core surrounded by an extended hydrogen envelope, the beamed power of the jet is not expected to be able to tunnel out of the envelope under most circumstances. This is because the jet head must displace the ambient stellar material and, therefore, expands at a rate which balances the ram pressure of this interaction with the momentum flux of the jet (e.g. Matzner, 2003). Following

the estimates of Quataert and Kasen (2012)'s Section 2.2, a typical jet whose working surface expands at a few percent the speed of light (as it displaces the surrounding stellar envelope) reaches only approximately $0.03c \times 10^3 \mathrm{s} \sim 10^{12}$ cm before the core-accretion event ends and the jet shuts off. Lacking the pressure to continue driving its expansion, the jet is choked by the surrounding gas distribution, and expands laterally, distributing its power more isotropically into the envelope material and powering an outburst (e.g. Murguia-Berthier et al., 2014; Senno et al., 2016). We note that Dexter and Kasen (2013), Quataert and Kasen (2012), and Woosley and Heger (2012) discuss an alternate scenario in which the jet might escape if long-lived accretion from the envelope material persists over a duration of hundreds of days. The typical energies range from $10^{50} - 10^{52}$ erg (Fryer & Woosley, 1998; W. Zhang & Fryer, 2001), as we discuss in Section 1.2.2.

An alternative process of stable burning has been suggested when the engulfed object is a neutron star. In these cases a Thorne-Zytkow Object is said to form – a star with a neutron-star core, which might stably burn hydrogen for up to 10^5 yr (Podsiadlowski, 2007; Podsiadlowski et al., 1995; Thorne & Zytkow, 1977), potentially showing unique surface features (Levesque et al., 2014). If the core of the helium star is near its original density when neutron star enters it, the flow convergence rate is high enough that it seems very difficult to avoid a neutrino-cooled accretion state (Chevalier, 1993; Fryer & Woosley, 1998). However, it is interesting to note that because the neutron star enters the core from the outside in (rather than inside-out as in a collapsar) there is a possibility that feedback from lower accretion-rate common envelope inspiral (e.g. Fryer et al., 1996) would prevent the object from ever reaching the hypercritical, neutrino-cooled accreting branch (see, for example, the trajectories of infall and accretion in Holgado et al., 2018; MacLeod & Ramirez-Ruiz, 2015). Thus, more work is needed to conclusively distinguish between these alternatives.

1.2.2 Model Adopted: Engine Mass and Energetics

Before merger the donor star consists of a core of mass M_{core} and an envelope of mass M_{env}. The total mass of the star is $M_* = M_{\mathrm{core}} + M_{\mathrm{env}}$. The compact-object companion that ends up in the center of the donor's core has mass $M_2 = qM_*$. When the two stars merge, M_2 accretes a fraction, f_{acc}, of M_{core}. This either causes it to grow if it is already

a black hole, or, if it is a neutron star, collapse to a black hole, then grow to a final mass,

$$M_{\rm BH,final} = M_2 + M_{\rm acc} = M_2 + f_{\rm acc} M_{\rm core}. \tag{1.1}$$

The released energy from the accretion is, therefore, $\Delta E_{\rm acc} = \eta M_{\rm acc} c^2$, where $\eta \sim 0.1$. Much of this energy is radiated by neutrino emission. However, some energy emerges mechanically, from a magnetohydrodynamic disk wind (e.g. Feng et al., 2018). The mechanical power is an uncertain fraction of the accretion energy, such that $\Delta E_{\rm mec} = f_{\rm mec} \Delta E_{\rm acc}$. Dexter and Kasen (2013) estimate $f_{\rm mec} \sim 10^{-3}$ given an inflow-outflow model in which the accreting material decreases as a power law with radius, implying

$$\Delta E_{\rm mec} \sim 3 \times 10^{50} \left(\frac{f_{\rm mec}}{10^{-3}} \right) \left(\frac{\eta}{0.1} \right) \left(\frac{M_{\rm acc}}{2 M_\odot} \right) \text{ erg}. \tag{1.2}$$

The energy that emerges in a jet via the Blandford and Znajek (1977) process can be estimated as (W. Zhang & Fryer, 2001),

$$\Delta E_{\rm BZ} \sim 10^{52} a^2 \left(\frac{M_{\rm BH}}{3 M_\odot} \right)^2 \left(\frac{B}{10^{15}\ \text{G}} \right)^2 \left(\frac{t_{\rm acc}}{10^2\ \text{s}} \right) \text{ erg}, \tag{1.3}$$

where B is the magnetic field in the disk, $t_{\rm acc}$ is the timescale of accretion, and a is the black hole's dimensionless spin.

As we show in section 1.5, mass ratios around $q \sim 0.1$ are expected for common envelop events leading to mergers. Based on the larger mass of the giant star, we expect $M_{\rm acc} \gtrsim M_{\rm BH}$, leading to values of order unity for a regardless of the initial spin state.

In what follows, we will assume that the compact object accretes the entire core mass ($f_{\rm acc} = 1.0$) and we explore explosion energies between 3×10^{50} erg and 10^{52} erg. We further assume that regardless of the precise mechanism or energetics, the energy is shared roughly spherically with the hydrogen envelope (Chevalier, 2012; Soker, 2019; Soker & Gilkis, 2018).

1.3 CIRCUMSTELLAR MATERIAL EXPELLED DURING BINARY COALESCENCE

As a basis for our analysis, we model binary coalescence and the circumbinary ejecta that results from the merger of two example mass ratio binaries. Here we describe our

numerical method, the unstable mass exchange that leads the binary to merge, and the CSM mass distribution that this runaway mass transfer creates. The distribution of CSM at large scales, $r \sim 10^{15}$ cm, is of particular importance for the outburst light curves. We therefore focus our numerical modeling on the early phases of runaway, unstable mass exchange that expels this largest-scale CSM.

1.3.1 Hydrodynamic Models of Binary Coalescence

Our models are simulated within the Eulerian hydrodynamic code Athena++ (Stone, J.M., in preparation), and are based on the methodology described in MacLeod et al. (2018a, 2018b), MacLeod et al. (2019). We use a spherical polar coordinate system surrounding the donor star in a binary pair. We model the interaction of this donor star with a softened point mass representing an unresolved companion object. The domain extends over the full three-dimensional solid angle from 0.1 to 100 times the donor-star's original radius.

The donor star is modeled by polytropic envelope, with structural index $\Gamma = 1.35$. The donor has a core mass of 25% its total mass. The gas in the simulation domain follows an ideal-gas equation of state, with index $\gamma = 1.35$. These choices are intended to approximately represent a convective, isentropic envelope of a massive star in which radiation pressure is important in the equation of state (in which case $\Gamma = \gamma \to 4/3$, e.g. MacLeod, Antoni, et al., 2017; Murguia-Berthier et al., 2017).

We initialize the calculation at a separation slightly smaller than the analytic Roche limit separation (a_{RL}), where the donor star overflows its Roche lobe (Eggleton, 1983), and halt the calculation when the companion star has plunged to 10% of the donor's original radius – the inner boundary of our computational domain. The binary is initialized in a circular orbit and the donor star is initially rotating as a solid body with rotational frequency matching the orbital frequency at a_{RL}.

The calculations themselves are carried out in dimensionless units where the donor's mass, radius, and gravitational constant are all set to unity. They may, therefore, be rescaled to a physical binary of any mass or size. Below, we report on two models which have secondary to donor star mass ratios of $q \equiv M_2/M_* = 0.1$ and $q = 0.3$. As we will see in Section 1.5, $q \sim 0.1$ is a very common mass ratio, while $q = 0.3$ is near the upper end of the range of events that result in mergers.

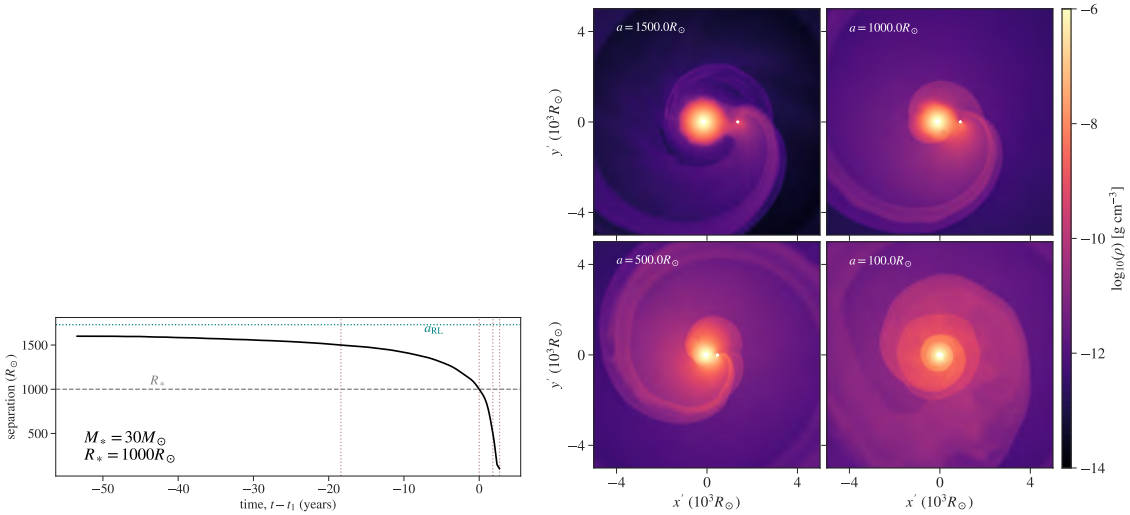

FIGURE 1.1 – Runaway Roche lobe overflow leading to binary coalescence for binary mass ratio $q = 0.1$. The upper panel shows binary separation as a function of time during our simulation. The lower panel shows four snapshots (marked with vertical lines in the upper panel) of the gas density distribution in the orbital plane. We show these slices through the orbital plane in a rotated $x' - y'$ coordinate system so that the companion star lies along the $+x$-axis. The dimensionless simulations are rescaled to donor star mass of $30M_\odot$ and radius of $1000R_\odot$ for specificity in these images. Following Roche lobe overflow, mass is pulled from the donor star and expelled from the binary system dragging the binary to tighter separations. The model is stopped when the companion object reaches 10% of the donor star's original radius, but the subsequent merger is expected to take place quite rapidly based on the rate of orbital decay (less than one year).

1.3.2 Unstable Mass Transfer Leading to Binary Merger

Mass transfer is unstable in our model binary system in that it runs away to ever increasing rates and drives the binary toward merger. This process begins with Roche lobe overflow of the donor star into the vicinity of its companion. In general, mass transfer proceeds unstably when the loss of material from the donor causes the donor star to increasingly overflow its Roche lobe – either because it grows in radius, or because its Roche lobe shrinks. In binary systems such conditions are often realized in binary pairs where a more massive donor star transfers mass onto a less massive accretor, causing the binary separation to shrink.

In Figure 1.1, we show the binary system separation as a function of time in our model system, and snapshots of the gas density distribution in the orbital plane. In

these figures, we have rescaled our dimensionless simulations to a fiducial donor star mass of $30M_\odot$ and radius of $1000R_\odot$. In the upper panel, time is zeroed at the time at which the companion plunges within the original donor-star's radius, t_1, where $a(t_1) = R_*$. Over the preceding 50 years, the binary separation continuously shrinks, at first gradually, but with increasing rapidity (MacLeod et al., 2018b). After the companion object plunges within the donor's envelope it spirals to the inner boundary of our computational domain (at 10% the donor's radius) within about 5 orbital cycles, or two years, approximately the orbital period at the donor star's surface. Projecting the rate of decay forward, the merger is estimated to take place in less than one year.

Mass loss from the donor star at the expense of orbital energy drives this rapid decrease in binary separation and the pair's coalescence. Turning our attention to the lower panels of Figure 1.1, we note that as the donor star overflows its Roche lobe, material is pulled, primarily from the vicinity of the L_1 Lagrange point, toward the companion object. As the orbital separation decreases, from $1500R_\odot$ to $1000R_\odot$ to $500R_\odot$, the breadth and intensity of this mass transfer stream increase dramatically. MacLeod et al. (2018b) studied the dynamics of this runaway, unstable Roche lobe overflow in detail, and found that the mass loss rate from the donor increases by orders of magnitude over this period. However, MacLeod et al. (2018b) also show that the analytic model of Paczyński and Sienkiewicz (1972) coupled to a point-mass binary orbit evolution model captures the key features of these stages once the specific angular momentum of the ejecta has been measured (e.g. Huang, 1963).

These high mass exchange rates quickly exceed the Eddington limit mass accretion rate that material can accrete onto a compact object companion, and much of the material pulled from the donor is lost to the circumbinary environment (as seen in the snapshots of Figure 1.1, though in the case of the simulation this is because accretion onto the companion object is not modeled, see MacLeod et al., 2018a). Much of this mass loss occurs near the L_2 Lagrange point, near the lower-mass companion object (MacLeod et al., 2018a; Metzger & Pejcha, 2017; Pejcha et al., 2016a, 2016b; Shu et al., 1979). By the final panel, where the separation is $100R_\odot$, the core of the original donor and companion object are mutually immersed in a significantly extended common envelope that originated from the donor star (Paczynski, 1976). Once immersed, some binary systems deposit enough energy into their environments to expel this envelope. Others do not, and the companion object merges with the core – powering the sort of

engine-driven explosions discussed in Section 1.2.

Because orbital tightening and coalescence of the binary system is a direct result of angular momentum loss to ejected material, the amount of ejecta relates directly to the binary properties. First using semi-analytic scalings (MacLeod, Macias, et al., 2017), then hydrodynamic simulation results (MacLeod et al., 2018a), we have found that the expelled mass at the onset of coalescence (defined as mass at $r > R_*$ at $t = t_1$) is always on the order of 25% the mass of the merging companion object (Section 4.2 of MacLeod et al., 2018a). In the calculation shown in Figure 1.1, which has a mass ratio $q = 0.1$, at t_1 the ejecta mass (measured as the mass at radius greater than the donor's original radius) is 16% the companion's mass, or approximately $0.49 M_\odot$. At the termination of our calculation, when the separation has decreased by a further factor of ten, the ejecta mass has increased to roughly 150% of the companion object's mass, or $4.45 M_\odot$. By comparison, our calculation with $q = 0.3$ expels nearly identical percentages of mass relative to the more massive black hole: $1.44 M_\odot$ at a separation equal to the donor's radius and $13.9 M_\odot$ in our final snapshot (separation 10% the donor's radius). In the following, we analyze the distribution of this material in the circumstellar environment.

1.3.3 Resultant Circumstellar Distribution

Next, we analyze the three-dimensional distribution of debris expelled by the merger episode. To do so, we analyze the final snapshot of our hydrodynamic simulation, when the separation has tightened to one-tenth the donor's original radius, or $100 R_\odot$ in our fiducial, $30 M_\odot$, $1000 R_\odot$ model. Because the binary separation is tightening extremely rapidly at this phase (the extrapolated time to merger is less than 1 year), material ejected subsequently in the merger does not affect the largest-scale gas distribution prior to the compact object's merger with the core. This, therefore, is the CSM that any explosive outburst will interact with as it expands, particularly when we consider the crucial scales of interest of 10^{14} to 10^{15} cm that lie near the photosphere of the explosive transient.

In Figure 1.2, we show the large-scale density distribution out to 50 times the initial donor radius ($5 \times 10^4 R_\odot$, or approximately 3.5×10^{15} cm). The panels show a slice through the orbital, $x - y$ plane, and an aziumthal average, plotted in $z - R$, perpendicular to the orbital plane. Figure 1.2 shows that a thick, extended circumbinary torus of expelled material from the donor's envelope has formed around the merging

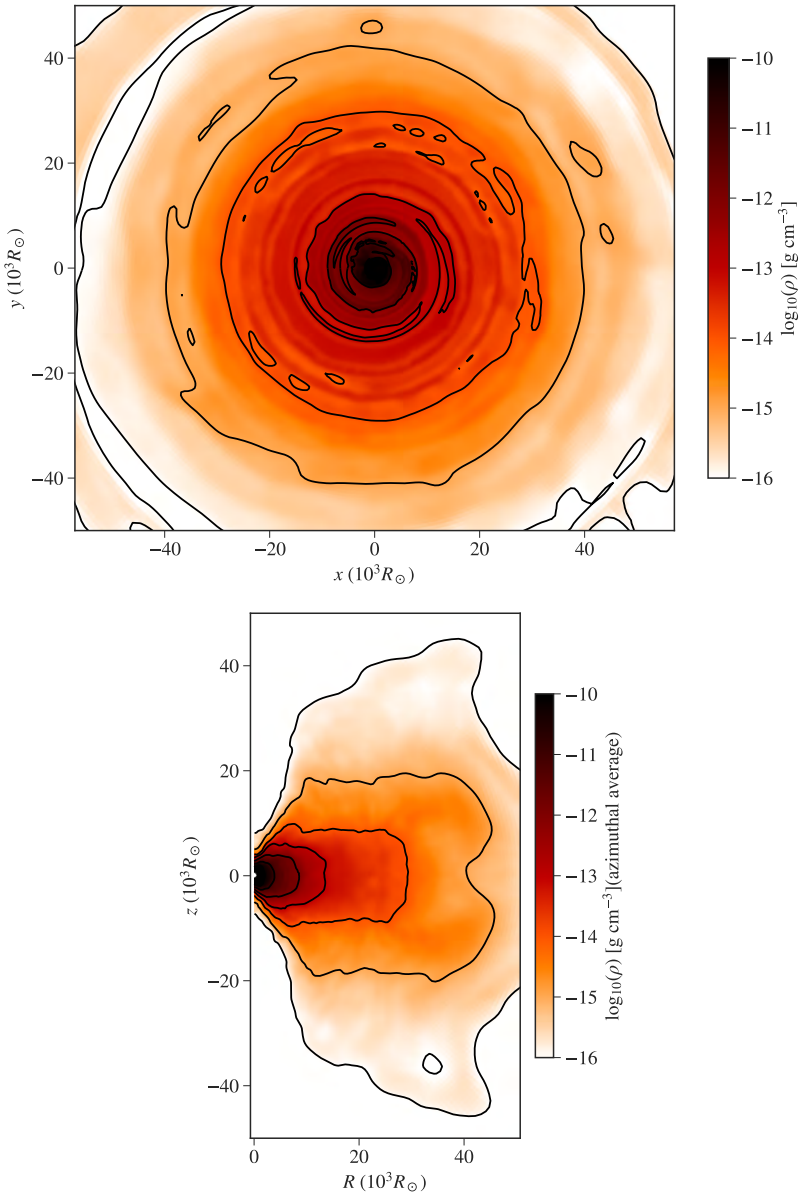

FIGURE 1.2 – Three dimensional distribution of ejecta near the time of merger. As in Figure 1.1, we have scaled to a fiducial donor mass of $30M_\odot$ and radius of $1000R_\odot$. When the compact object merges with the donor's core, it is surrounded by an extensive, thick torus of debris expelled by the merger itself.

pair of stars. This torus is roughly azimuthally symmetric, but has distinct structure in polar angle, with relatively evacuated poles and dense equator, representative of the fact that material is flung away from the merging binary in the equatorial plane. Pejcha et al. (2016a, 2016b), Pejcha et al. (2017) analyzed the thermodynamics of similar outflows and show that heating, arising continuously from internal shocks, and radiative diffusion and cooling very likely regulate the torus scale height. Thus, the precise scale height observed in Figure 1.2, modeled under the simplification of an ideal-gas equation of state, would likely be modified by the inclusion of more detailed physics.

MacLeod et al. (2018a) analyzed the kinematics of this torus material and found that the radial velocities of the most extended material are low relative to the escape velocity of the original donor star (roughly 100 km s^{-1} for our fiducial model). Thus, the majority of these (earlier) ejecta around bound to the merging binary. The implication of this material being bound is that after some expansion it reaches zero radial velocity and settles into some pressure and rotationally supported quasi-static torus, the density of which is highlighted in Figure 1.2. Some of the material at smaller radii (the later ejecta) is moving more rapidly, at velocities similar to the escape velocity. It therefore collides with the earlier, slow moving ejecta (MacLeod et al., 2018a). Qualitatively, these velocities are similar to other sources of stellar mass loss like winds or non-terminal outbursts, in that they are similar to the giant star's escape velocity and are much less than the later explosion's blast wave velocity.

Though the axisymmetric torus structure discussed above is clearly structured in polar angle, for the sake of computational efficiency, we model the interaction of the explosive blast wave with a one-dimensional (spherically-symmetric) density distribution derived from these models. In future work, it may be extremely interesting to relax this simplification. To derive one-dimensional profiles, we spherically-average our model results about the donor star's core.

These 1D density profiles are shown in Figure 1.3, in which we compare the unperturbed envelope profile to the cases disturbed by binaries of $q = 0.1$ and $q = 0.3$. Where the hydrostatic profile has a distinct limb at the donor's radius, the post-merger profiles show a roughly power-law slope in radius, with approximate scaling of r^{-3}, as shown in the lower panel by rescaling with a multipilicative factor proportional to r^3. Comparing the $q = 0.1$ and $q = 0.3$ results shows that in the higher mass-ratio coalescence, more of

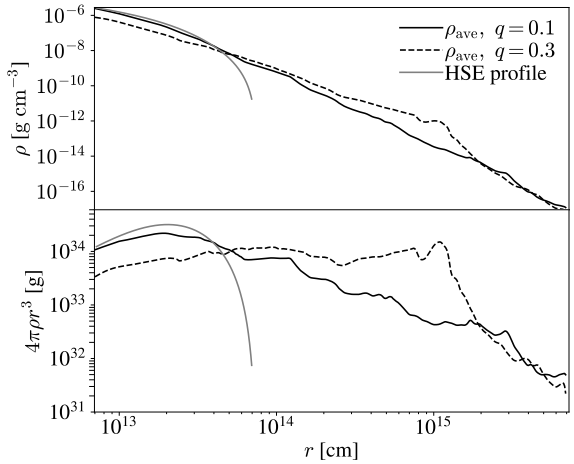

FIGURE 1.3 – Spherically-averaged density distributions, comparing the initial, hydrostatic polytrope (labeled HSE), with merger-simulation snapshots for $q = 0.1$ and $q = 0.3$. As in the previous Figures, we scale our models to a donor of $30M_\odot$ and $1000R_\odot$. The existence of significant quantities of mass near the type II supernova photosphere radius of 10^{15} cm implies that interaction with this medium will play an important role in explosive transient light curves.

the envelope material has been expelled beyond the donor's original radius, yielding a shallower density fall-off with radius and a profile with more mass at large radii. In both cases, we see that the distribution of ejecta extends to roughly 10^{15} cm, with of order a solar mass ($q = 0.3$) or a tenth of a solar mass ($q = 0.1$) on these scales.

1.4 MERGER-DRIVEN LIGHT CURVES

In this section we use analytic and numerical models to understand the properties of merger-driven light curves. We find that the CSM distribution plays a crucial role in shaping these light curves. In Section 1.4.1 we provide some analytic context for the potential role of CSM. In Section 1.4.2, we describe our numerical method for 1D radiative hydrodynamics calculations and light curve generation. Finally, in Sections 1.4.3 and 1.4.4 we describe the key features and variations across parameter space of these numerical model light curves.

1.4.1 Analytic Context for Contribution to Radiative Efficiency from CSM Interaction

In order to provide context for the interpretation of our numerical light curve models, in this section we analyze simplified analytic models of emission powered by CSM interaction. In general, CSM interaction enhances the intrinsic luminosity of "cooling emission" from heated, expanding material like supernova ejecta. As ejecta shock-heat by collisions with CSM, their kinetic energy is dissipated and converted into radiation. Depending on the location of the interaction (within or outside the photosphere), this radiation may either escape immediately or adiabatically decay with expansion in the outflow prior to being free to stream out.

In particular, we focus on different radial density profiles of CSM material and the role this plays in shaping transient light curves. In doing so, we summarize and build on a considerable literature that describes how CSM interaction can form a significant contribution or even dominate the radiative power of a transient under certain conditions (e.g. Chandra, 2018; Chevalier, 2012; Chevalier & Irwin, 2011, 2012; Chugai & Danziger, 1994; Ginzburg & Balberg, 2012, 2014; Kleiser et al., 2018; T. J. Moriya, Blinnikov, et al., 2013; T. J. Moriya & Maeda, 2012; T. J. Moriya, Maeda, et al., 2013; Morozova, Piro, Renzo, Ott, et al., 2015; Morozova et al., 2017, 2018; Morozova & Stone, 2018; Ofek et al., 2014; Pan et al., 2013; Smith & McCray, 2007).

1.4.1.1 *Thin Shell of CSM*

In the simplest version of a CSM interaction, an additional internal energy ΔE is added to ejecta by sweeping up a thin shell of CSM,

$$\Delta E \approx \frac{dM_{\rm CSM}}{M_{\rm tot}} E, \tag{1.4}$$

where $M_{\rm tot}$ is the sum of the explosive ejecta and the swept-up CSM mass internal to the shell, $dM_{\rm CSM}$ is the CSM shell mass, and E is the kinetic energy of the explosive ejecta. If this deposition of internal energy occurs in optically thin regions, all of this energy is radiated, and $\Delta E_{\rm rad} \approx \Delta E$. If the CSM shell lies interior to the photosphere radius, the heated ejecta must continue to expand, with gas internal energy decaying along an adiabat, before they are free to radiate. If we assume that gas specific internal energy

decays adiabatically as r^{-1} prior to reaching the photosphere (which is the case when radiation pressure dominates and $P \propto \rho^{4/3}$ along an adiabat), then $\Delta E_{\rm rad} \approx (r/R_{\rm ph})\Delta E$.

1.4.1.2 *Continuous Distributions of CSM*

The differential radiated energy due to sweeping up a CSM mass $dM_{\rm CSM}$ at radius r interior to the photosphere radius is

$$\frac{dE_{\rm rad}}{dM_{\rm CSM}} \approx \frac{E}{M_{\rm tot}}\frac{r}{R_{\rm ph}}, \tag{1.5}$$

where $E_{\rm rad}$ is the contribution to the radiated energy due to CSM interaction alone. As before, we are also assuming that gas specific internal energy decays adiabatically as r^{-1}. Given a continuous distribution of CSM material distributed between R_* and $R_{\rm ph}$, we can integrate this expression over radius. In what follows, we will assume that E is constant, which is justified only if $M_{\rm CSM} \ll M_{\rm tot}$ and $E_{\rm rad} \ll E$. Otherwise, the losses in kinetic energy to thermal energy or radiation must be taken into account. We replace $dM_{\rm CSM} = 4\pi r^2 \rho dr$, where ρ is the CSM density, to write

$$\begin{aligned}\frac{E_{\rm rad}}{E} &\approx \int_{R_*}^{R_{\rm ph}} \frac{r}{R_{\rm ph}}\frac{4\pi r^2\rho}{M_{\rm tot}}dr,\\ &\approx \frac{4\pi}{R_{\rm ph}M_{\rm tot}}\int_{R_*}^{R_{\rm ph}} \rho r^3 dr.\end{aligned} \tag{1.6}$$

This integral shows that the dependence of $\rho(r)$ will be critical in determining the CSM contribution to the radiated luminosity.

Let us write a general, power law density form for the CSM that applies from the stellar radius, R_*, to the eventual photosphere radius, $R_{\rm ph}$,

$$\rho(r) = \rho_{\rm ph}\left(\frac{r}{R_{\rm ph}}\right)^{-n}, \tag{1.7}$$

where $\rho_{\rm ph}$ is the density at the photosphere radius, and we have chosen $R_{\rm ph}$ as a characteristic radius to normalize the power law. We will further adopt the approximation that $R_{\rm ph} \gg R_*$, under which the total CSM mass can be written,

$$M_{\rm CSM} \approx 4\pi\rho_{\rm ph}R_{\rm ph}^3 \times \begin{cases} 1 & n = 2,\\ \ln(R_{\rm ph}/R_*) & n = 3,\\ R_{\rm ph}/R_* & n = 4,\end{cases} \tag{1.8}$$

for several representative values of n.

The most frequently considered form of ρ is that of a steady, spherical wind, $n = 2$ (Chevalier & Irwin, 2011; Ginzburg & Balberg, 2012). Then, equation (1.6) becomes

$$\begin{aligned}\frac{E_{\rm rad}}{E} &\approx \frac{4\pi\rho_{\rm ph}R_{\rm ph}}{M_{\rm tot}}\int_{R_*}^{R_{\rm ph}} r dr,\\ &\approx \frac{4\pi\rho_{\rm ph}R_{\rm ph}^3}{2M_{\rm tot}},\\ &\approx \frac{1}{2}\frac{M_{\rm CSM}}{M_{\rm tot}} \quad (\text{for } n=2),\end{aligned} \tag{1.9}$$

thus retrieving the often quoted result of the increase in radiated energy scaling with the CSM mass as a fraction of the total mass (Chevalier & Irwin, 2011; Ginzburg & Balberg, 2012; Pan et al., 2013).

In our $q = 0.3$ model, the one-dimensional profile approximates $n = 3$, which yeilds constant mass per logarithmic increase in radius. For $n = 3$, equation (1.6) evaluates to

$$\begin{aligned}\frac{E_{\rm rad}}{E} &\approx \frac{4\pi\rho_{\rm ph}R_{\rm ph}^2}{M_{\rm tot}}\int_{R_*}^{R_{\rm ph}} dr,\\ &\approx \frac{4\pi\rho_{\rm ph}R_{\rm ph}^3}{M_{\rm tot}},\\ &\approx \frac{1}{\ln\left(\frac{R_{\rm ph}}{R_*}\right)}\frac{M_{\rm CSM}}{M_{\rm tot}} \quad (\text{for } n=3),\end{aligned} \tag{1.10}$$

where, in the last line, we have used $M_{\rm CSM}$ from equation (1.8). First, we emphasize that the ratio of $R_{\rm ph}$ to R_* now affects the radiated luminosity arising from CSM interaction, which is not the case for $n = 2$. Therefore, when $R_{\rm ph} \gg R_*$, the radiated energy from this CSM profile is considerably less than that of the $n = 2$ profile. A final way to interpret this result is in terms of the CSM mass at radii similar to the photosphere radius, $r \sim R_{\rm ph}$. From equation (1.8), this is approximately $M_{\rm CSM}/\ln(R_{\rm ph}/R_*)$. Equation (1.10) shows that this is the fraction of the CSM mass that contributes significantly to the radiated energy.

In our $q = 0.1$ merger model, the scaling of the CSM is steeper, approximately $\rho \propto r^{-4}$.

We reevaluate equation (1.6) for $n = 4$ to find,

$$\begin{aligned}\frac{E_{\rm rad}}{E} &\approx \frac{4\pi\rho_{\rm ph}R_{\rm ph}^3}{M_{\rm tot}}\int_{R_*}^{R_{\rm ph}}\frac{1}{r}dr,\\ &\approx \frac{4\pi\rho_{\rm ph}R_{\rm ph}^3}{M_{\rm tot}}\ln\left(\frac{R_{\rm ph}}{R_*}\right),\\ &\approx \left(\frac{R_*}{R_{\rm ph}}\right)\ln\left(\frac{R_{\rm ph}}{R_*}\right)\frac{M_{\rm CSM}}{M_{\rm tot}} \quad \text{(for } n=4\text{).}\end{aligned} \tag{1.11}$$

Thus, for $R_{\rm ph} \gg R_*$, the CSM contribution to radiated luminosity is less for $n = 4$ than either $n = 3$ or $n = 2$ given a CSM mass. This result can be interperted in light of equation 1.8, which shows that the fraction of CSM mass with $r \sim R_{\rm ph}$ is $R_*/R_{\rm ph}$ for $n = 4$.

1.4.1.3 *Interpretation*

In the preceding subsection, we have shown that for CSM density profiles that are sufficiently steep, $n \geq 3$, the CSM contribution to the radiated luminosity $E_{\rm rad}/E$ depends on the ratio of the stellar radius over the photosphere radius – the radial extent of the CSM. This important ratio varies in explosions with different size stars of similar mass, or over the time evolution of a given transient as the photosphere radius increases. If $E_{\rm rad}/E$ becomes too small, then CSM interaction does not contribute significantly to the light curve of the transient at a given phase and the bulk of the radiated luminosity comes instead from the adiabatically-expanding blast wave. In this case, the transient assumes more typical supernovae type IIP properties.

These scalings indicate that we expect the CSM to be an important contribution to the $q = 0.3$ merger case light curve, because the mass in the CSM is a significant fraction of the total envelope mass, and with $n = 3$ there is only logarithmic dependence on $R_{\rm ph}/R_*$, equation (1.10). In the $q = 0.1$ merger case, in which $n = 4$, we expect preferential contribution from CSM interaction at early times in the transient light curves or for particularly extended donors, because either situation maximizes the ratio $R_*/R_{\rm ph}$, see equation (1.11).

Finally, we have so far discussed the case in which the CSM distribution extends out to, and perhaps beyond the photosphere radius. This is not necessarily realized. In the case where the CSM terminates at a radius R_0, for which $R_0 < R_{\rm ph}$, the radiated

luminosity from CSM interaction is computed much as before, but only integrating the mass distribution out to R_0. This reduces the radiated luminosity due to CSM interaction by a factor similar to $R_0/R_{\rm ph} < 1$. In the sections that follow, we use this framework to interpret 1D radiative transfer models of explosions interacting with our model CSM distributions.

1.4.2 1D Radiation Hydrodynamic Models

While the analytic approach highlighted above is useful, it is necessarily simplified. To extend these calculations of the CSM imprint on transient light curves to slightly more realistic scenarios, we need to perform the associated integrations numerically. We utilize the publicly available spherically symmetric (1D) Lagrangian hydrodynamics code SuperNova Explosion Code (SNEC) to calculate bolometric and filtered light curves (Morozova, Ott, et al., 2015; Morozova, Piro, Renzo, Ott, et al., 2015; Morozova et al., 2017). The code uses equilibrium-diffusion radiation transport to follow the time dependent radiation hydrodynamics of the expanding blast wave. We choose to set the equation of state using the built-in version of the Paczynski (1983) equation of state, which includes contributions to the total pressure from radiation, ions and electrons based on the composition.

We map our one-dimensional, spherically-averaged profiles, shown in Figure 1.3, into SNEC. Mass grid cells are customized by the user's choice of binning in mass, and we have found that the density profiles' steep decline is best simulated with increasingly fine mass resolution at larger radii. This means that the shock break out is not well resolved (Ensman & Burrows, 1992; Morozova, Ott, et al., 2015), but light curve calculations after the first day are robust as shown by Morozova, Piro, Renzo, Ott, et al. (2015). We run the simulations for this paper with 456 grid cells.

Even so, the code does not function well for the lowest densities. We therefore are required to restrict the CSM density profile to $\rho > 10^{-12}$ g cm^{-3} (Morozova & Stone, 2018). The outer radius is therefore 2.6×10^{14} cm for the fiducial simulation with $q = 0.1$ and 1.0×10^{15} cm for the simulation with $q = 0.3$. We note that this restriction is not ideal because it limits the potential interaction-driven luminosity of our models, see equations (1.10) and (1.11). In practice, this implies that the CSM maximum radius is often less than the photosphere radius, $R_0 < R_{\rm ph}$, and the CSM contribution to the eventual radiated luminosity is reduced accordingly, see the discussion of Section

1.4.1.3. Nonetheless, the truncated profiles do retain more than 95% of the CSM mass in all parameter variations. We assume a roughly solar isotopic composition that matches the hydrogen envelope of a presupernova stellar model of an initially $15M_\odot$ star evolved with the MESA code (Paxton et al., 2019) that is included in the SNEC distribution.

To drive the explosion of our models, we adopt a thermal bomb at the inner edge of the envelope domain. This broadly mimics the energy deposition of the quenched jet into the hydrogen envelope, as described in Section 1.2. Based on Morozova, Piro, Renzo, Ott, et al. (2015), we deposit the energy over the innermost $\Delta M_{bomb} = 0.1 M_\odot$ over a duration $\Delta t_{bomb} = 0.1$ s (Morozova, Piro, Renzo, Ott, et al., 2015, has shown that the model light curves are not particularly sensitive to these parameters, see their Figure 5). The code also offers the option of adding Nickel to the composition. Though Nickel and lanthanide production is possible in merger-driven explosions (e.g. Grichener & Soker, 2019; Siegel et al., 2019), the quantities are uncertain. Because decay of radioactive ^{56}Ni mainly powers the late-time emission, here we choose to focus on Ni-free models of the early light curve dominated by the CSM and the hydrogen envelope (Morozova, Piro, Renzo, Ott, et al., 2015). Lacking radioactive material in the ejecta, our models decline rapidly after the ejecta become fully transparent. Emission from the photosphere in SNEC is assumed to follow a thermal blackbody, and thus neglects some line-blanketing effects that may be important for iron-rich ejecta in the U and B bands.

Finally, in Appendix A.1, we test the sensitivity of our model results to these choices by varying the inner mass (or equivalently, radius) at which energy is deposited, as well as the mass-resolution of the SNEC calculation.

1.4.3 Imprint of CSM

We begin to explore the imprint of the CSM mass distribution on the explosion light curve in Figure 1.4, in which we plot luminosities, along with photosphere radii, effective temperature, and gas bulk velocity at the photosphere radius for our fiducial case of a $30M_\odot$ and $1000R_\odot$ donor star in its initial, hydrostatic equilibrium state (labeled HSE), and following merger with a $3M_\odot$ ($q = 0.1$) or $9M_\odot$ ($q = 0.3$) black hole. In each case, the explosion energy is taken to be 10^{51} erg, and is injected at 0.1 times the radius of the original donor star, the innermost radius resolved in our hydrodynamical models.

As predicted by the analytic scalings in Section 1.4.1, the models with CSM are

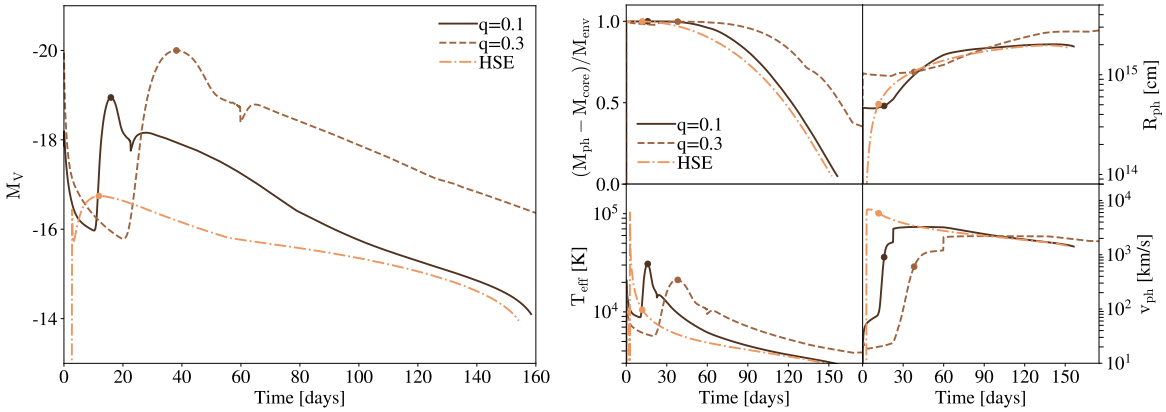

FIGURE 1.4 – Fiducial, $30M_\odot$, $1000R_\odot$ model star undergoing explosion of 10^{51} erg in three scenarios: in its initial hydrostatic state (HSE), after merging with a $3M_\odot$ black hole ($q = 0.1$), and after merging with a $9M_\odot$ black hole ($q = 0.3$). The large panel shows bolometric luminosity, while the smaller panels track the photosphere's properties – its mass element within the ejecta, radius, effective temperature, and bulk velocity at its location. CSM interaction brightens the merger models significantly as compared to the HSE case. Points mark the time of peak V-band brightness.

significantly more luminous at peak (by a factor of roughly 100) than the hydrostatic model. The CSM interaction models also show delayed time of peak brightness, modified colors, and light curve shapes, as we discuss in what follows. Morozova et al. (2017) have recently discussed how rapid mass loss immediately pre-supernova can transform light curves from a IIP shape (at low pre-supernova mass loss rates) to the more luminous type IIL (at higher mass loss rates). This occurs when additional internal energy is added to the ejecta by shock-heating due to the CSM mass as it is swept up. Because the CSM lies outside the stellar radius, this new internal energy does not adiabatically decay as much prior to being radiated from the transient's photosphere. As a result, the radiative efficiency of the models, E_{rad}/E, ranges from 1.4% for the HSE model, to 8.5% for the $q = 0.1$ model, to 23% for the $q = 0.3$ model. We note that these radiative efficiencies are with a factor of two of those prediced by the scaling models of Section 1.4.1, for $n = 4$ and $n = 3$, respectively, equations (1.10) and (1.11).

Many features of our model light curves with merger-ejecta are similar to Morozova et al. (2017)'s model suites including dense CSM distributions of varying mass and power-law slope. In particular, elevated early "plateau" luminosities that decay down to the unperturbed plateau are representative of significant CSM at radii less

than the transient's eventual maximum photosphere radius of approximately 10^{15} cm. Comparing to Figure 1.3, we note that large masses of relatively close-in CSM are the distinguishing features of our models. The resultant light curves, therefore, have typical duration of hundreds of days like normal IIP, not the thousands of days observed in some IIn supernovae with extended CSM distributions like that observed for SN 1988Z and SN 2005ip (Smith, 2017).

Comparing the two mergers, the $q = 0.3$ scenario with larger $M_{\rm CSM}$ has a later and more luminous peak, along with a higher luminosity during the plateau. Because the CSM mass is related to the merger, we find $M_{\rm CSM}/M_{\rm tot} \sim 1.5q$, see Section 1.3. The models of Figure 1.4 for a hydrostatic explosion, $q = 0.1$, and $q = 0.3$, thus provide a context for interpreting the apparent variations in CSM contribution. While the CSM mass plays a primary role in determining the light curve brightness, the distribution of CSM is crucial in shaping the light curves. In the case of the hydrostatic explosion (labeled HSE in Figure 1.4), there is no contribution from CSM interaction. The $q = 0.3$ model shows a light curve that is always elevated by approximately three magnitudes above the HSE model due to CSM interaction (at $t > 30$ d). By contrast, the $q = 0.1$ model is significantly elevated above the HSE model only earlier in the lightcurve, and converges to the HSE plateau luminosity around 100 d. The distinction between these cases lies in the slope of the CSM density and in the outer CSM radius.

For $q = 0.3$, the CSM has $\rho \propto r^{-3}$ ($n = 3$). The total radiative efficiency due to the CSM, $E_{\rm rad}/E$, equation (1.10), only decreases with the logarithm of the ratio of the expanding ejetca photosphere radius, seen in the right hand panels of Figure 1.4, to initial stellar radius (which is the base of the CSM distribution). Further, the outermost radius of the CSM at the moment of energy injection in our numerical model is $R_0 = 10^{15}$ cm. This is larger than the ejecta photosphere radius early in the light curve, and similar to the ejecta photosphere radius later in the light curve, implying that there is not a significant adiabatic degradation of the CSM contribution before light can escape from the expanding ejecta.

We can compare these trends to the $q = 0.1$ model, in which case the overall CSM mass is lower and $\rho \propto r^{-4}$ ($n = 4$). As the photosphere grows with time across the transient duration, the contribution of CSM interaction decreases approximately as $R_*/R_{\rm ph}$, see equation (1.11). Of similar importance, the outermost CSM radius at the moment of energy deposition, $R_0 = 2.6 \times 10^{14}$ cm is a factor of a few less than the ejecta

photosphere radius late in the plateau phase. This effect also decreases the contribution of the CSM to the late-stage light curve compared to an $n = 4$ CSM of infinite extension, e.g. equation (1.11). As a result, the light curve converges to a similar magnitude as the plateau of the hydrostatic explosion late in the light curve.

In addition to brightening the explosion, CSM interaction modifies the object's colors at timescales of days to weeks on which transients are typically discovered. CSM interaction yields bluer colors at time of peak (effective temperatures of several 10^4 K on timescales of tens of days). The photosphere cools to more typical IIP temperatures of thousands of Kelvin only after 50 to 100 days (for the $q = 0.1$ and $q = 0.3$ models, respectively). These higher temperatures are directly representative of the extra internal energy injection due to shock heating of the ejecta by the CSM density distribution.

1.4.4 Implications of Varying Energetics and Donor Star Properties

We expect mergers between compact objects and giant stars to occur at a wide range of donor star and compact object properties because the binaries from which they form have broad distributions of mass, semi-major axis, and mass ratio. Further, the energy of the central engine is unknown, and may, in fact, vary from merger to merger. Here we explore the implications of the parameter space of merger properties on the resultant light curves.

Figure 1.5 shows V-band light curves for a range of models, all $q = 0.1$, in which we vary energy (top panel), mass (center panel) and radius (bottom panel) around our fiducial, $30M_\odot$, $1000R_\odot$ case with 10^{51} erg explosion energy. In all of these cases, because $q = 0.1$, the CSM density profile is roughly $\rho \propto r^{-4}$, and equation (1.11) predicts the approximate contribution of CSM interaction to the radiated energy.

Varying explosion energy with other properties kept fixed yields the qualitatively expected variation in light curve luminosity and duration – higher energy explosions give rise to faster ejecta, with more luminous but shorter duration transients. We note that the relative contribution of the CSM interaction, shown by the early bump in the lightcurve, decreases in the more energetic supernovae. When the explosion energy changes, one consequence is that the photosphere radius during the plateau phase changes, roughly as $R_{\rm ph} \propto E^{5/12}$ (Kasen & Woosley, 2009; Popov, 1993). For higher energies, the larger photosphere radii imply smaller contributions from CSM interaction, because the photosphere is further outside the outermost CSM radius, R_0.

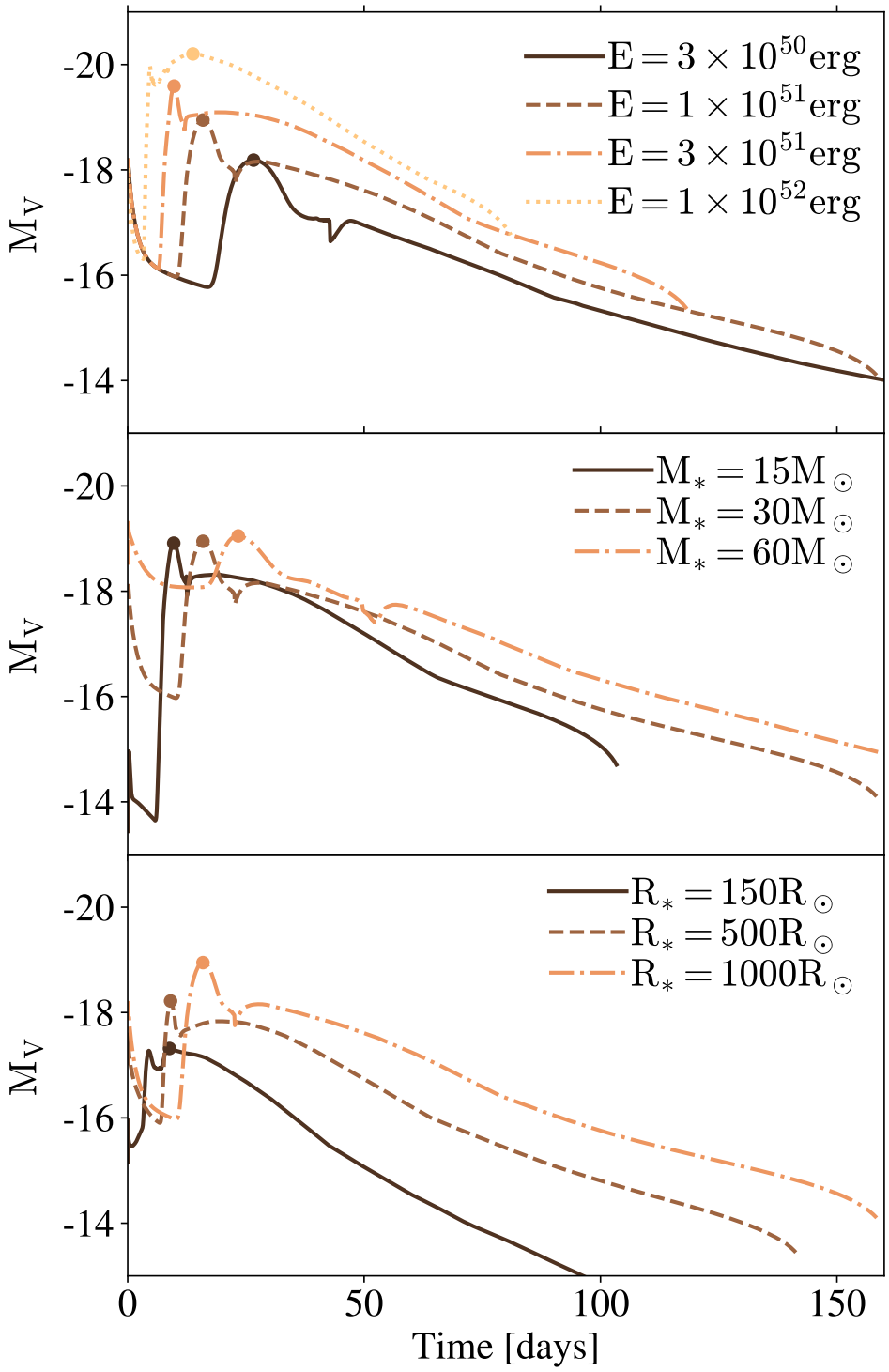

FIGURE 1.5 – Bolometric light curves for $q = 0.1$ transients with varying energy (top panel) mass (center panel) and radius (lower panel). Unless specifically modified, we adopt our fiducial values of a $30M_\odot$ and $1000R_\odot$ donor star and 10^{51} erg explosion. The location of the V-band peak is marked with a dot. Varying energetics and donor star properties create light curves of different duration, peak brightness, and degree of CSM contribution.

In Figure 1.5, we observe that the light curve shape transforms as the energy increases. This is reflective of the decreasing contribution of CSM interaction to the light curve as E increases. Consequently, the radiative efficiency decreases from 10% for the 3×10^{50} erg explosion to 4.7% for the the 10^{52} erg explosion. With this smaller CSM contribution, the 10^{52} erg explosion light curve shows a relatively typical IIP shape, with a small, early bump due to the CSM.

Varying donor star properties, in the form of mass and radius, similarly changes light curve duration, peak brightness, and shape. More massive donor stars yield higher ejecta masses, but constant $M_{\rm CSM}/M_{\rm tot} \propto q$. At fixed energy, the ejecta velocities are lower and light curve durations are correspondingly longer. As mass varies in Figure 1.5, the plateau photosphere radius varies only mildly because the higher ejecta masses are balanced by lower ejecta velocities. Therefore, though these models show different characteristic timescales, they all have very similar peak magnitudes and degrees of CSM contribution to their overall radiated luminosity (total radiative efficiencies range from 11.7% to 9.0%).

Varying donor star radius changes not only the extent of the donor itself but the extent of the CSM, which extends to tens of stellar radii. This, in turn, varies the crucial ratio of maximum CSM radius to transient photosphere radius (because varying donor radius has little effect on $R_{\rm ph}$). When the donor is more compact, for example $150R_\odot$, the CSM extends to approximately 10^{14} cm, and largely affects only the early lightcurve. Progressively larger donors of $500R_\odot$ and $1000R_\odot$ scale the radial size of the CSM distribution. This scaling yields more CSM material at radii closer to the transient's photosphere radius at later times (for example near peak), in turn implying higher radiative efficiencies, and brighter transients. For example, the $150R_\odot$ model has a radiative efficiency of only 1.9%, while the $500R_\odot$ model radiates 5.3% of the explosion energy and the $1000R_\odot$ model radiates 8.5% of the explosion energy.

Figure 1.6 summarizes the parameter space of merger-driven explosions in luminosity, timescale, effective temperature, and radiative efficiency. The majority of merger-driven explosions have radiative efficiency on the order of 10%, much higher than the hydrostatic model with no CSM. The $q = 0.3$ model has even higher radiative efficiency of 25%. However, the more compact $150R_\odot$ donor model and the highest explosion energy model, 10^{52} erg, both show relatively minimal CSM-interaction features in Figure 1.5 and have somewhat lower radiative efficiency (because $R_*/R_{\rm ph}$ and $R_0/R_{\rm ph}$

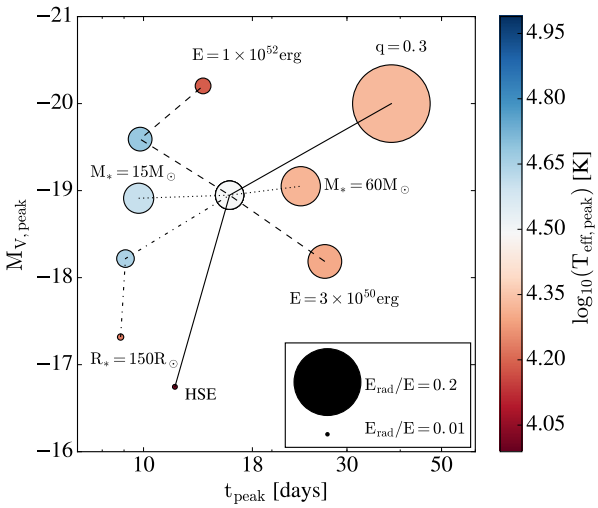

FIGURE 1.6 – Luminosity and timescale of the optical light curves of merger-driven explosions. Here we additionally summarize radiative efficiency with size of the marker and effective temperature at peak with color. The central point is our fiducial model; lines connect the isolated variations of energy (dashed), mass (dotted), radius (dot-dash), and mass ratio (solid).

are reduced, see section 1.4.1).

Together, Figure 1.6 shows that merger-driven explosions occupy a somewhat restricted phase space of luminosity and timescale. Typical models are more luminous than standard type IIP, but less luminous than super-luminous supernovae. In all of the models bearing significant CSM-interaction features, effective temperature varies systematically with time of peak brightness with longer-duration transients appearing redder and shorter-duration transients appearing bluer.

1.5 POPULATION SYNTHESIS OF MERGER-DRIVEN EXPLOSIONS

We use population synthesis models of stellar binary evolution to explore the statistical properties of binary systems at the time of a common envelope phase leading to merger between a compact object and a giant star's core. We then use these models to estimate the population of observable merger-driven explosions.

1.5.1 Population Model

We analyze rapid population synthesis models from the Compact Object Mergers: Population, Astrophysics and Statistics (COMPAS) suite (Barrett et al., 2018; Stevenson, Vigna-Gómez, et al., 2017; Vigna-Gómez et al., 2018). These models employ approximate stellar evolution tracks and parameterized physics in order to facilitate exploration of the statistical properties of binary stellar evolution – including rare outcomes like the formation of double compact object binaries (for a full description of the approach, see Barrett et al., 2018; Stevenson, Vigna-Gómez, et al., 2017; Vigna-Gómez et al., 2018). In particular, we adopt the model parameters of Vigna-Gómez et al. (2018)'s "Fiducial" case and we capitalize on a recent development by Vigna-Gomez et. al. (in preparation) to record the characteristics and outcomes of all common envelope phases experienced by modeled binaries.

Initial distributions of binary properties are sampled at the zero-age main sequence (ZAMS) in COMPAS. In the models we study, the mass of the primary star is drawn from an initial mass function in the form $dN/dm \propto m^{-2.3}$ (Salpeter, 1955) with masses between $5 \leq m/\mathrm{M}_\odot \leq 100$. The mass of the secondary star is then chosen from a flat distribution in mass ratio with $0.1 < q_{\mathrm{ZAMS}} \leq 1$ (Sana et al., 2012). The initial separation is drawn from a flat-in-the-log distribution, $dN/da \propto a^{-1}$, with separations between $0.01 < a_{\mathrm{ZAMS}}/\mathrm{AU} < 1000$ (Sana et al., 2012). All stars in our model population adopt solar metalicity ($Z = 0.0142$). A total of 10^6 binary systems are simulated.

Common envelope phases are identified by conditions for dynamically unstable mass transfer in COMPAS. When a common envelope episode occurs, an energy criterion is used to evaluate the outcome. In particular, the final change in orbital energy is related to the energy needed to unbind the giant star's hydrogen envelope from its core, $\Delta E_{\mathrm{orb}} = -\alpha E_{\mathrm{bind}}$, where $\alpha = 1$ is an efficiency parameter (Webbink, 1984). If the maximal change in orbital energy (defined on the basis of the minimal separation at which the core fills its Roche lobe) is insufficient to unbind the envelope, $|\Delta E_{\mathrm{orb}}| < \alpha |E_{\mathrm{bind}}|$, then a merger between the companion and the core is assumed to result. This scaling implies that more compact stars have higher binding energies and, for a given companion mass, are more likely to result in merger. More extended stars (nearer to the tip of their giant-branch evolution) have lower binding energies and their common envelope phases are more likely to result in envelope ejection (de Kool, 1990; Kruckow et al., 2016).

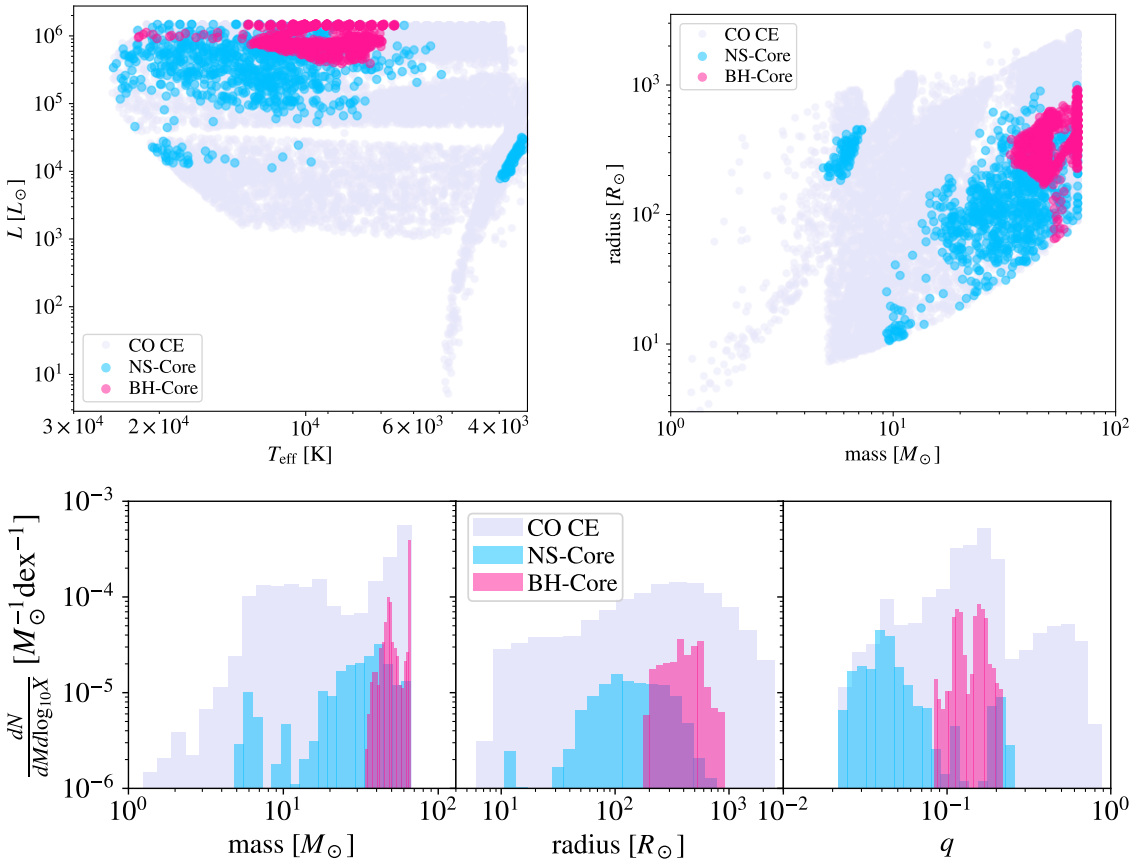

FIGURE 1.7 – Distributions of binary properties at the onset of common envelope phases involving black holes or neutron stars interacting with evolved, massive star donors with mass greater than $10M_\odot$. Here we distinguish between all common envelope phases involving compact objects (labeled CO CE), and cases in which a neutron star merges with the donor's helium core (NS-Core) or a black hole merges with the donor's helium core (BH-Core). Mergers occur in roughly 22% of the compact object common envelope phases, and are split relatively equally between black hole and neutron star events. The companion mass distribution, especially for black hole mergers, favors massive companions. Histograms are plotted in units of events per solar mass of stars formed per logarithmic bin in x-value (mass, radius, or mass ratio).

1.5.2 Compact Object-Core Mergers

The most common evolutionary channel leading to a compact - giant star merger and a merger-driven explosion is as follows. A binary pair in an initially relatively wide orbit evolves, likely going through a dynamically stable mass transfer from the initially

more-massive star onto its companion. That initially more massive star undergoes core collapse, leaving behind either a neutron star or black hole remnant. Because neutron star kicks tend to be large in magnitude (Fryer et al., 2012; Zevin et al., 2019), a relatively small fraction of systems containing newly-formed neutron stars – less than 4% (Vigna-Gómez et al., 2018) – remain bound following the supernova. Of those that remain binaries, a large fraction will undergo a common envelope phase during a reverse episode of mass transfer onto the compact object, initiated by the expansion of the intially less massive companion after it completes core hydrogen fusion. This may result in either a merger or a common envelope ejection. Those that eject their envelopes may go on to form a double compact object binary, as discussed by Vigna-Gómez et al. (2018).

The population of common envelope phases involving compact objects in these models is depicted in Figure 1.7. In what follows, we report on and show only events that involve post-main-sequence donor stars that have developed a distinct core. We show the distribution of these sources in the Hertzsprung-Russell Diagram (HRD) as well as in mass, radius, and mass ratio. We highlight the distinction between all common envelope phases involving compact objects (labeled CO CE), and events resulting in mergers between a neutron star and the donor core (labeled NS-Core) and a black hole and the donor core (labeled BH-Core).

A number of interesting trends emerge from these distributions. While common envelope phases occur throughout the donor star's post-main sequence evolution, and therefore also the HRD, particular criteria are most likely to result in a merger. Merging sources tend to have the more compact radii compared to the overall distribution of common envelope phases. This results in the majority of the population having $T_{\rm eff} \gtrsim 10^4$ K, while a smaller portion of lower-mass donors have lower temperatures. Neutron stars interact with a broad range of stellar companion masses, while black holes common envelope phases tend to involve massive $M \gtrsim 30 M_\odot$ and thus luminous donors. Typical mass ratios of compact-object common envelope phases range from $0.02 \lesssim q \lesssim 0.6$; those resulting in mergers tend to have $q \lesssim 0.2$. The upper limits of these ranges reflect the conditions of dynamical mass transfer stability and envelope ejection, respectively. Of the mergers, the black holes form the higher mass-ratio population, $0.1 \lesssim q \lesssim 0.2$, while neutron stars typically have $q \lesssim 0.1$.

1.5.3 Event Rate

We can estimate the event rate of compact object–giant star mergers using the results of these population synthesis models. We simulate 10^6 binary systems, or approximately $2.08 \times 10^7 M_\odot$ of binary mass. Each solar mass of modeled stars represents $3.8 M_\odot$ of stars formed (Vigna-Gómez et al., 2018). From our models, common envelope phases involving compact objects occur with a frequency of $1.7 \times 10^{-4} M_\odot^{-1}$, where the unit denotes mergers per solar mass of stars formed. Of these, approximately 14% result in mergers. Among the mergers, 46% involve black holes, while 53% involve neutron stars. The rate of black hole–core mergers is approximately $1.35 \times 10^{-5} M_\odot^{-1}$ the rate of neutron star–core mergers is $1.18 \times 10^{-5} M_\odot^{-1}$. The majority of these events occur in a spread of ages between 3 and 40 Myr – a tail of the distribution extends to roughly 100 Myr. Mergers are thus strongly correlated with recent star formation. By comparison, core collapse supernovae occur with a frequency of $5.5 \times 10^{-3} M_\odot^{-1}$ in the model systems. Merger-driven explosions therefore represent on the order of 0.5% of all core collapse events.

1.5.4 Outburst Population

Having assessed the population of donor stars and compact object companions that undergo mergers, we now extend the results of our light curve models to estimate the properties of the population of observable transients. Guided by the results of Sections 1.4.4 and 1.4.1, we note that CSM interaction is most important when the binary mass ratio is larger (yielding more merger ejecta and higher CSM mass) and when the radius is extended (yielding less adiabatic degradation of CSM-interaction energy, proportional to $R_*/R_{\rm ph}$). Comparison to the population properties in Figure 1.7 shows that the systems that tend to have high mass ratios and large radii are predominantly the BH-Core merger group, in which a black hole merges with its giant star companion. By contrast, the typical radii, $R_* \sim 100 R_\odot$, and mass ratios, $q < 0.1$, for the neutron star-core mergers are such that we expect less dramatic signatures of CSM interaction (see Figure 1.5). The higher mass ratios in binaries with BH's are due to greater mass retention in the formation of BH's compared to the formation of neutron stars.

To map our parameter variations onto the modeled population, we estimate the following scalings of M_V with changing model parameters from the results of Figure

1.6,

$$\begin{aligned} M_{V,\mathrm{peak}} \approx -18.9 &- 2.42\log_{10}(R_*/1000R_\odot) \\ &- 0.229\log_{10}(M_*/30M_\odot) \\ &- 1.41\log_{10}(E/10^{51}\ \mathrm{erg}) \\ &- 2.20\log_{10}(q/0.1) \end{aligned} \tag{1.12}$$

An important caveat is that, given our limited model parameter coverage, these numerical scalings represent the individual dependencies on binary properties about our fiducial model rather than the full parameter covariance. We will compare these luminosities to those of standard type IIP supernovae (Popov, 1993),

$$\begin{aligned} M_V \approx -11.42 &- 1.67\log_{10}(R_*/R_\odot) \\ &+ 1.25\log_{10}(M_*/M_\odot) \\ &- 2.08\log_{10}(E/10^{50}\ \mathrm{erg}). \end{aligned} \tag{1.13}$$

We note that the Popov (1993) model accurately predicts the peak V-band luminosity of our hydrostatic model (Figures 1.4 and 1.6).

In Figure 1.8, we apply these scalings to the population of compact-object core mergers. Again we divide the population on the basis of whether a neutron star or a black hole is merging with the core. In the upper panel, we assume that all events have 10^{51} erg explosion energy. We find that CSM interaction (as predicted by equation (1.12)) brightens all merger-driven explosions relative to their hydrostatic equivalents (as estimated from equation (1.13)). The neutron star-core mergers are brighter by approximately 1 magnitude than their Popov-model equivalents. However, the black hole mergers are brightened significantly more, by approximately 3 magnitudes. In this diagram, we observe that the black hole merger-driven explosions form a distinct population more luminous than the non-CSM-interacting IIP population.

In the lower panel of Figure 1.8, we apply the scaling of equation (1.2) to determine the explosion energy. We adopt the fiducial efficiencies and we assume that the entire core mass of the donor star comprises the accreted mass, thus the explosion energy becomes $3\times10^{50}(M_{\mathrm{core}}/2M_\odot)$ erg. This scaling yields a range of energies with a somewhat higher median value of 3.4×10^{51} erg than the upper panel. As a result, we observe that the predicted magnitudes are somewhat brighter, particularly for the black-hole transients, which tend to involve higher-mass cores, and thus higher predicted energies.

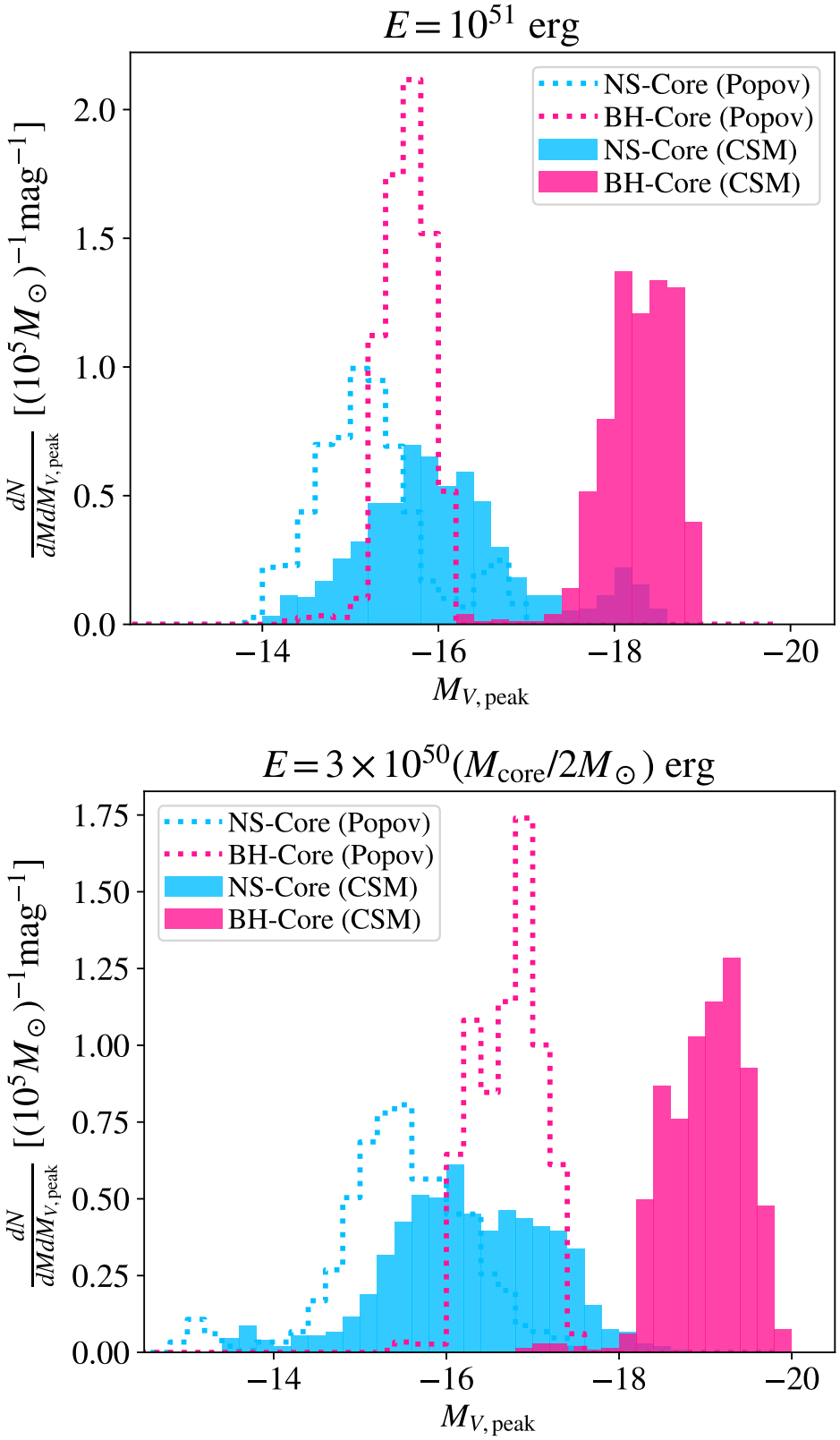

FIGURE 1.8 – Transformation of merger-driven explosions by CSM interaction. We show peak V-band magnitudes of the population of merger-driven explosions using the Popov (1993) model (equation (1.13); dashed lines), then apply our results (equation (1.12); filled histograms) to derive the peak magnitudes including CSM interaction with merger-expelled ejecta. Black hole merger-driven explosions, in particular, form a distinct and luminous group that comprises 49% of the merger-driven explosion transients. The y-axis is shown in units of events per magnitude per $10^5 M_\odot$ of stars formed.

1.6 DISCUSSION

1.6.1 Production of Supernovae-like Transients With Massive, Close CSM

It has recently become apparent that a large fraction of type II supernovae show signs of interaction with CSM of densities much larger than that implied by nominal stellar-wind mass loss. Type IIn supernovae have long been acknowledged to have CSM due to the persistent narrow lines in their spectra. This otherwise diverse class of supernovae occupies approximately 10% of the overall core collapse rate (e.g. Kiewe et al., 2012). More recently, evidence has been emerging that a majority (up to 70%) of type II supernovae show evidence of having at least $0.1 M_{\odot}$ of CSM imprinted on their light curves (Morozova et al., 2018; Morozova & Stone, 2018). For example, Förster et al. (2018) has argued for systematic evidence that most type II shock breakouts are delayed by interaction with dense CSM. A shared feature of the CSM in many type IIP and IIL supernovae is that it is very close to the donor star, indicating its loss in the years immediately prior to the explosion (e.g. Ofek, Sullivan, et al., 2013; Smith & Arnett, 2014).

One proposed explanation for the presence of pre-supernova CSM ejection lies in the phenomenological comparison to luminous blue variable (LBV) outbursts, which are non-terminal outbursts of massive O-type stars. Though the precise cause of these outbursts remains uncertain (e.g. Justham et al., 2014), as does their potential correlation with the evolutionary trend of the core toward collapse, in at least one dramatic example, SN2009ip, both LBV outbursts and a terminal supernova were observed in the same object over the course of a decade (Margutti et al., 2014; Mauerhan et al., 2014; Ofek, Lin, et al., 2013; Prieto et al., 2013; Smith et al., 2014; Smith et al., 2010).

Another possible explanation links the CSM to the vigorous convection due to accelerating nuclear burning in the pre-supernova core. In this case, convection launches gravity waves at the interface between the convective core and an overlying radiative layer. These waves propagate through the radiative zone and dissipate near the base of the convective hydrogen envelope (Fuller, 2017; Quataert & Shiode, 2012; Shiode & Quataert, 2014). The luminosity of these dissipating waves can be highly super Eddington in the year prior to core-collapse, driving extensive mass loss (Quataert et al.,

2016) or outbursts (Fuller, 2017).

An explosion driven by the merger itself also naturally links merger ejecta and CSM with the explosive fate of the star, as we have described in the preceding sections. However, a merger-driven model cannot explain the full diversity of type II supernovae or their CSM properties. In practice, some combination of these processes must be at play in order to explain the abundance and diversity of CSM observed in type II supernovae.

1.6.2 Comparison to Observed Supernovae

We compare our model light curves to two representative, well-studied supernovae. Photometric similarity is insufficient to demonstrate the origin of a given transient, as we discuss further in Section 1.6.3. In this section, we contextualize our model merger-driven explosions by showing that they bear similarities to transients already in the supernovae archives. The supernovae discussed here both showed signs of CSM interaction before transitioning to type IIL supernovae. Type IIL supernovae with steep declines in luminosity resemble the shape of light curves seen in our simulations, whereas the supernovae with wind CSM interaction studied in Morozova et al., 2016 have shapes resembling type IIPs with an extra bumb in the first 50 days.

1.6.2.1 *1979c*

SN1979c, classified as a type IIL, was discovered in April 1979, several weeks after explosion (Mattei et al., 1979). It has been observed extensively at radio wavelengths (Bartel & Bietenholz, 2008; Marcaide et al., 2009; Montes et al., 2000; Weiler et al., 1986), and early modeling suggested a very large progenitor radius of $R \sim 6000 R_\odot$ and CSM extending out to $R \sim 10^5 R_\odot$ (Bartunov & Blinnikov, 1992).

Observations from the following 20 years gave rise to more theoretical discussion. Bartel and Bietenholz (2003) suggested that the remnant is expanding into low density CSM with $\rho \sim r^{-n}$, with $n = 1.94^{+0.10}_{-0.05}$ decreasing to $n < 1.5$ at larger radii. It is not clear the extent to which this slope is in tension with our model predictions. In particular, we predict steeper $n \sim$ 3-4 primarily at radii smaller than those probed by Bartel and Bietenholz (2003)'s measurements. Later Kasen and Bildsten (2010) suggested that the light curve was brightened by the spindown of a magnetar at the center of the

SN remnant. Patnaude et al. (2011) note that, rather than a magnetar, a $5-10M_{\odot}$ BH accreting from fallback material can also explain X-ray data seen from 1995 and 2007.

In the top panel of figure 1.9 we have plotted optical data from the first 100 days of observation (from the open supernova catalog; Guillochon et al., 2017). On top we plot absolute magnitudes from our simulations with $M_* = 30M_{\odot}$ and $R_* = 1000R_{\odot}$ and $E = 3 \times 10^{51}$erg. The plot is not a fit, but shows that the outcome of our simulations can closely replicate observed transients. This, in addition to the potential for a remnant black hole (Patnaude et al., 2011) make SN1979c an interesting candidate for further investigation under the merger-driven hypothesis.

1.6.2.2 *1998s*

SN1998s is one of the most studied type IIn supernovae (Shivvers et al., 2015). From spectral lines, two shells of CSM were identified. Fassia et al. (2001) found that the inner CSM was within 90AU from the center and the outer CSM extended from 185 AU to over 1800 AU. The classification of SN1998s as a IIn is a direct result of the very early spectral observations; the narrow line features disappeared and morphed into the broad lines of a type IIL or IIb within weeks Smith (2017).

SN1998S has later been interpreted as having a red supergiant progenitor with possibly asymmetric CSM consisting of the two separate shells, caused by separate mass-loss events. (Kangas et al., 2016) claims that this type of SN is very common and that many IIL and IIP share spectral features with IIn in early spectra.

In the bottom panel of figure 1.9 we plot the V, R and I band data from SN1998s (data from the open supernova catalog; Guillochon et al., 2017) plotted on top of absolute magnitude from simulations with $M_* = 30M_{\odot}$ and $E = 1 \times 10^{51}$ erg, solid lines for radius scaled to $R_* = 1000R_{\odot}$, and dashed lines for $R_* = 500R_{\odot}$. The light curve we see from from our simulations with $R_* = 1000R_{\odot}$ is similar to SN1998s, though the rate of decline perhaps fits better with our $R_* = 500R_{\odot}$ simulation. Just as with SN1979c, the overall light curve shape, duration, and brightness are well-approximated by our models. The presence of nearby CSM is also consistent with a merger-driven explosion. However, the explanation for two distinct shells of CSM is not immediately apparent given our model predictions, and may be in tension with the merger-driven hypothesis for this transient (though see the discussion of Clayton et al., 2017).

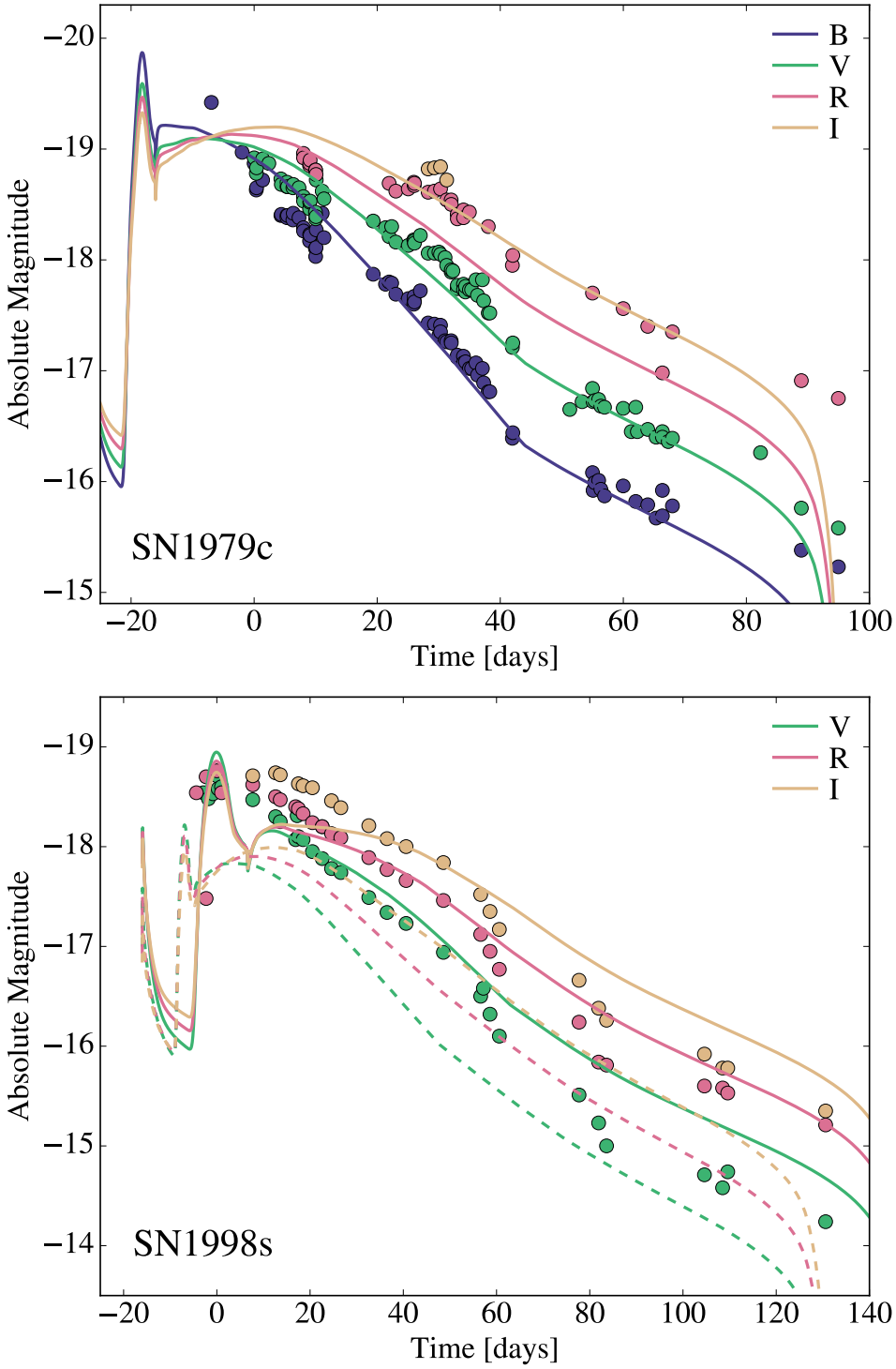

FIGURE 1.9 – *Upper panel:* SN 1979c plotted on top of absolute magnitude from simulations with $q = 0.1$, $M_* = 30M_\odot$, $R_* = 1000R_\odot$ and $E_{SN} = 3 \times 10^{51} erg$. *Lower panel:* SN 1998s plotted on top of absolute magnitude from simulations with $q = 0.1$, $M_* = 30M_\odot$ and radius scaled to $R_* = 1000R_\odot$ (solid lines) and $R_* = 500R_\odot$ (dashed lines).

1.6.3 Identification in Optical Surveys

Having shown that merger-driven explosion models can reproduce the basic, photometric properties of several observed supernovae, we now focus on the prospects for their more secure identification.

The prevalence of merger-driven explosions (of order 0.5% of the core-collapse rate) begs questions about their prior detection in existing datasets and their imprints on future surveys. Current surveys, such as the Zwicky Transient Factory (Bellm & Kulkarni, 2017) and All-Sky Automated Survey for Supernovae (e.g. Holoien et al., 2019) are presently discovering hundreds of new core-collapse supernovae per year. This discovery rate suggests that one or more merger-driven explosions is currently being discovered per year. Efforts at early discovery and spectroscopy of these transients aim to reveal CSM properties through "flash spectroscopy" in which the CSM is ionized prior to being swept up by the blast wave. The Large Synoptic Survey Telescope (LSST) will discover on the order of 10^5 core collapse events per year (LSST Science Collaboration et al., 2009, chapter 8), implying hundreds to thousands of merger-driven explosions detected in a given observing year.

Among this flood of optical transients, the challenge will be unambiguous identification of merger-driven explosions rather than detection. A full consideration is beyond the scope of our initial study, but we speculate on several potential signatures here. The explosion driven by accretion feedback is expected to preferentially expand perpendicularly to the equatorial plane. And as discussed in Section 1.3, the ejecta from the pre-merger common envelope phase are densest in the equatorial plane of the binary. When the supernova explodes into this aspherical density distribution, the blast wave will be shaped by these asymmetrical surroundings (Blondin et al., 1996). Emission from the photosphere will, as a result, be polarized by one to several percent, as has been described in the case of SN2009ip (Mauerhan et al., 2014).

The interacting binary progenitor of the explosion may also offer clues in the identification of merger-driven supernovae, as in ongoing progenitor-monitoring efforts described by Adams et al. (2017) and Kochanek et al. (2008). Drawing parallels to low-mass, Galactic stellar merger events like V1309 Sco (Mason et al., 2010; Tylenda et al., 2011), increasing rates of non-conservative mass transfer (seen in the panels of Figure 1.1) may enshroud the merging binary in dust and cause an optical fading of the progenitor star prior to merger. In V1309 Sco, such a phase of optical dimming

was observed in the phase of 100 to 1000 orbital periods prior to coalescence. In the last orbits leading into the merger (the portion captured by Figure 1.1), V1309 Sco brightened in optical bands as more-and-more emission arose from the outflow from the binary (Pejcha, 2014; Pejcha et al., 2016a, 2016b; Pejcha et al., 2017). Future work is needed to extend these scenarios to detailed predictions for pre-explosive behavior in massive star coalescence.

Multiwavelength, particularly X-ray, signatures, while less frequently available than optical photometry, provide a powerful tool for probing early CSM interaction (e.g. Chevalier & Irwin, 2012; Margutti et al., 2017; Morozova & Stone, 2018). These data can probe the CSM distribuiton in great detail, including the density distribution through the hard to soft emission ratio (Morozova & Stone, 2018). If the CSM is as steep as predicted in the merger-driven models (steeper than $\rho \propto r^{-3}$), it will accelerate the leading edge of the ejecta to high velocities and produce hard x-ray emission (Morozova & Stone, 2018).

Finally, merger-driven explosions will leave a black hole as the remnant of the rapid accretion phase following merger of the compact object with the stellar core. Though black hole formation is common in core-collapse events, it is typically believed to accompany implosion rather than explosions and luminous supernovae (e.g. Sukhbold et al., 2018). If detected, the coexistence of a supernova-like transient and a remnant black hole would thus be consistent with the merger-driven explosion scenario. In theory we might distinguish neutron star and black hole central x-ray sources on the basis of their x-ray specta. In practice, this identification can be ambiguous when the surrounding, absorbing medium is substantial. One such example of a transient harboring an embedded x-ray source is AT 2018cow (Margutti et al., 2019).

1.7 SUMMARY AND CONCLUSION

In this paper, we have presented models for merger-driven explosions that arise from the plunge of a compact object within the helium core of its giant star companion following a common envelope phase (Chevalier, 2012). When a compact object merges with the helium core of a massive, post main-sequence star, the conditions for rapid, neutrino-cooled accretion are met (e.g. W. Zhang & Fryer, 2001). The accompanying release of energy may deposit approximately 10^{51} erg into the surrounding hydrogen

envelope, leading to a merger-driven explosion (Chevalier, 2012). Some key findings of our investigation are:

1. The binary coalescence leading to the merger of the compact object with the core expels slow-moving material into the surrounding environment, forming a dense, toroidal CSM (Figures 1.1 and 1.2). The spherically-averaged density profile has a steep radial slope of $\rho \propto r^{-3}$ or $\rho \propto r^{-4}$ (Figure 1.3).
2. Using 1D radiation hydrodynamic models of the explosions, we find that the CSM distribution is crucial in shaping the transient light curves. Merger-driven explosions are brightened by up to three magnitudes relative to their counterparts in hydrostatic stars (Figure 1.4), with timescale and light curve shape that vary with donor-star mass and radius and explosion energy (Figures 1.5 and 1.6).
3. From population models, we find that black hole and neutron star mergers with giant star companions occur with similar frequency, each with a rate per mass of stars formed of $\sim 1.25 \times 10^{-5} M_{\odot}^{-1}$. The combined rate is 0.5% of the core-collapse rate in our models. Merger-driven explosions occur across a roughly flat distribution of donor-star masses from $10 M_{\odot}$ to $100 M_{\odot}$ (Figure 1.7). CSM interaction brightens neutron star mergers by approximately one magnitude, but brightens the population of black hole mergers by approximately three magnitudes relative to type IIP models with the same energy injection and pre-supernova stellar mass and radius (Figure 1.8).
4. The most luminous transients, those involving black hole mergers, are at least as common as their less luminous neutron star counterparts. Black hole mergers have $M_{V,\mathrm{peak}} \sim -18$ to -20 with $t_{\mathrm{peak}} \sim 20$ to 30 d. The implication for optical surveys is that the brightest, easiest-to-detect events comprise a significant fraction of the entire population.

The calculations presented in this paper have demonstrated that merger-driven explosions provide a natural mechanism for the production of supernovae-like transients with close-in, slow-moving CSM. Future work could improve on the treatment of the stellar model (a polytropic envelope in our approximation) and the details of energy injection into this envelope. At present, we inject energy spherically into the envelope at one tenth the star's overall radius. In practice, the unknown location and asymmetry of energy injection might play a key role in shaping transient light curves, colors, and peak luminosities with respect to the estimates of our current models.

We compare our models to two representative supernovae, SN1979c and SN1998s in Figure 1.9. However, we note that more work is needed to provide unambiguous confirmations of merger-driven explosions. In Section 1.6.3, we discuss additional strategies for the identification of merger-driven explosions including their asymmetry and polarization due to the toroidal CSM, the properties of their progenitor binaries, and their early spectra and X-ray emission. In future work, these signatures can be investigated through multi-dimensional calculations of the explosive evolution and emergent light curve, as well as more detailed modeling of the progenitor system's plunge toward merger.

II

Fallback supernova

CHAPTER 2

Black Hole Formation in Fallback Supernova and the Spins of LIGO Sources

---

This chapter is based on the following article:

"Black Hole Formation in Fallback Supernova and the Spins of LIGO Sources"

APJl, Volume 862, Issue 1, article id. L3, 6 pp. (2018).

ArXiv e-prints: 1805.01269.

Authors: Sophie Lund Schrøder, Aldo Batta, Enrico Ramriez-Ruiz.

ABSTRACT

Here we investigate within the context of field binary progenitors how the the spin of LIGO sources vary when the helium star-descendent black hole (BH) is formed in a failed supernova (SN) explosion rather than by direct collapse. To this end, we make use of 3d hydrodynamical simulations of fallback supernova in close binary systems with properties designed to emulate LIGO sources. By systematically varying the explosion energy and the binary properties, we are able to explore the effects that the companion has on redistributing the angular momentum of the system. We find that, unlike the mass, the spin of the newly formed BH varies only slightly with the currently theoretically unconstrained energy of the SN and is primarily determined by the initial binary separation. In contrast, variations in the initial binary separation yield sizable changes on the resultant effective spin of the system. This implies that the formation pathways of LIGO sources leading to a particular effective spin might be far less restrictive than the standard direct collapse scenario suggests.

2.1 INTRODUCTION

The gravitational wave (GW) signals detected by LIGO (LIGO Scientific & Virgo Collaboration, 2017; LIGO Scientific Collaboration & VIRGO Collaboration, 2016; LIGO Scientific Collaboration & Virgo Collaboration, 2016b; LIGO Scientific Collaboration, Virgo Collaboration, & Burns, 2017; LIGO Scientific Collaboration, Virgo Collaboration, & South Africa/MeerKAT, 2017) have uncovered a population of black holes (BHs) that is significantly more massive than the population known to reside in accreting binaries (Remillard & McClintock, 2006). While there is significant debate in the community about how black hole binaries are assembled (Belczynski et al., 2016; de Mink & Mandel, 2016; Gerosa & Berti, 2017; Kalogera et al., 2007; LIGO Scientific Collaboration & Virgo Collaboration, 2016a; Portegies Zwart & McMillan, 2000; Postnov & Yungelson, 2014; Rodriguez, Zevin, et al., 2016; Sadowski et al., 2008; Wysocki et al., 2018), the classical scenario (Tutukov & Yungelson, 1993; Voss & Tauris, 2003) remains one of the leading candidates. In this channel, a wide massive binary undergoes a series of mass transfer episodes leading to a tight binary comprised of a massive helium star (M_*) and a BH (M_1), prior to the formation of the second BH (M_2). LIGO observations of the mass-weighted angular momentum perpendicular to the orbital plane $\chi_{\rm eff}$, have been argued

to provide constraints on this formation channel (Farr et al., 2017; Rodriguez, Zevin, et al., 2016; Stevenson, Vigna-Gómez, et al., 2017). This is because vital information on the mass transfer history of the binary and the spin of M_* is imprinted on

$$\chi_{\rm eff} = \frac{M_1 \vec{a_1} + M_2 \vec{a_2}}{M_1 + M_2} \cdot \hat{L}. \tag{2.1}$$

Here $\vec{a_1}$ and $\vec{a_2}$ are the dimensionless spins of the BHs and $\hat{L}$ is the direction of the angular momentum in the orbital plane.

The angular momentum of the secondary BH is intimately linked to that of the progenitor helium star, which in turn is determined by its mass-loss history and the torque exerted by the primary black hole (Kushnir et al., 2017; Qin et al., 2018; Zaldarriaga et al., 2018). This torque can effectively drive synchronization of the stellar spin and the orbit in binaries tighter than d_τ, the maximum separation allowed for synchronization within the life of the helium star (Zaldarriaga et al., 2018). The final angular momentum of the star thus provides a reasonable estimate of a_2 when the mass and angular momentum losses from the final supernova explosion are ignored. All previous works have assumed that such effects are small based on the simple expectation that LIGO BHs are formed by direct collapse.

Motivated by the fact that the nature of BH-forming supernova (SN) explosions is not to well understood (Fryer et al., 2012; Pejcha & Thompson, 2015; Ugliano et al., 2012), in this Letter we explore the effects on $\chi_{\rm eff}$ when the second BH M_2 instead is formed by a fallback SN explosion (Batta et al., 2017; Dexter & Kasen, 2013; Fernández et al., 2018; Fryer et al., 2012; Lovegrove & Woosley, 2013; T. Moriya et al., 2010; Perna et al., 2014). For this purpose we make use of 3d hydrodynamical simulations of fallback SN in close binary systems with properties aimed at reproducing LIGO GW signals. The structure of this Letter is as follows. In Section 2.2 we describe the numerical formalism used to initiate the fallback SN explosion and compute the subsequent evolution of the binary. In Section 2.3 we describe the dynamics of the fallback material and its effect on the final spin of both BHs. Lastly, in Section 2.4 we present our key findings and relate them to the current population of LIGO sources.

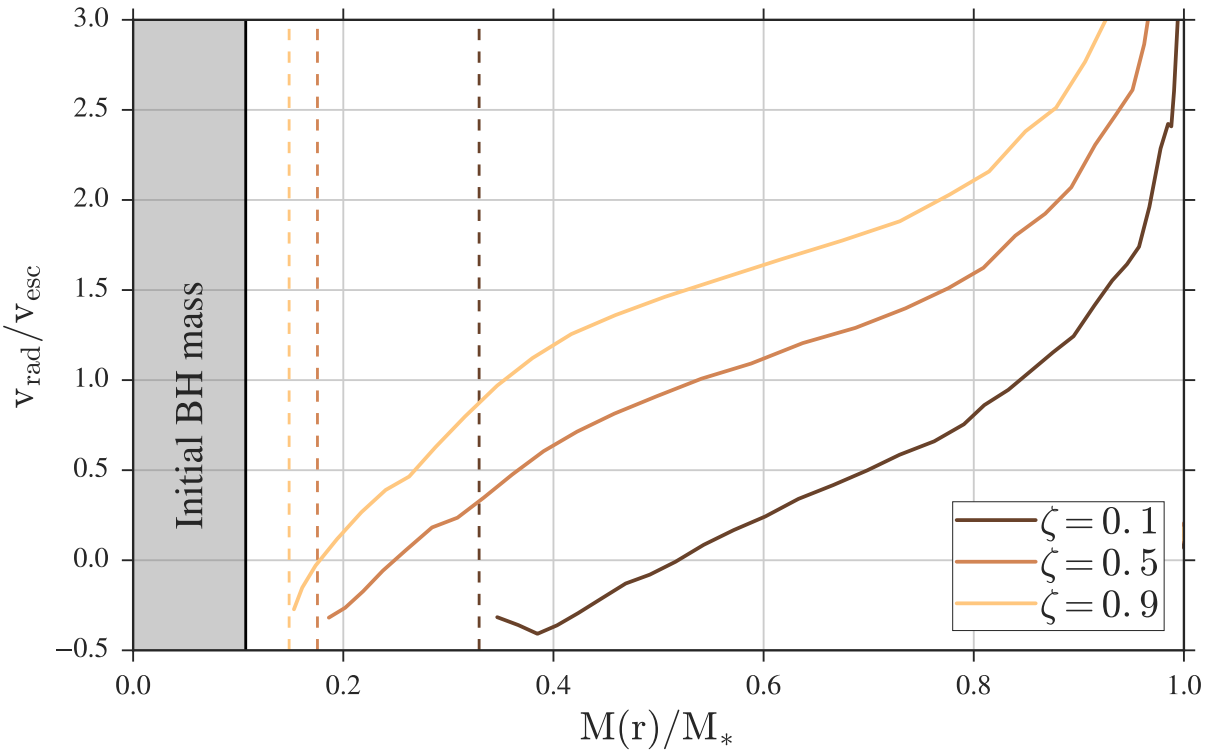

FIGURE 2.1 – The velocity profile of the ejecta at $d_* = 1$ (soon after the shock emerges from the stellar envelope) is plotted in units of the escape velocity for three different initial explosion energies.The shaded region shows the initial BH mass. The subsequent growth of the BH depends on the amount of fallback material, which in turn, depends strongly on the energy injected. The dashed lines show the current mass of the BH for different explosion energies.

2.2 METHODS AND INITIAL SETUP

Here we follow the setup described in Batta et al. (2017) to study the evolution of the progenitor binary system after the birth of M_2. We make use of a modified version of the three-dimensional smoothed particle hydrodynamics (SPH) code GADGET2 (Springel, 2005), with our initial setup consisting of a tidally locked $28M_\odot$ helium star in orbit around a BH of $M_1 = 15M_\odot$. The reader is referred to Batta et al. (2017) for further details on initial particle distribution and numerical accretion. We settled for a resolution of 5×10^5 particles, which showed convergence for a_2 and properly captured the dynamics of the ejecta and the binary system. Higher resolution studies using 2×10^6 particles were carried out to demonstrate convergence and accuracy for representative

cases.

To study the interaction of the fallback material with the newly formed BH binary we explore three sets of simulations. Each set starts with the initial binary in a circular orbit with a separation $d = d_* R_*$, where $d_* = 2$, 3 or 5 and R_* is the pre-SN star's radius. Then for each orbital separation we run simulations with at least four different SN explosion energies. In all cases we assume $a_1 = 0$ based on the results of Qin et al., 2018, and assume that synchronization of the stellar spin and the orbit has taken place, as is expected for the initial separations used in this analysis. Given the large uncertainties in BH natal kick estimations (Mandel, 2016; Repetto & Nelemans, 2015), we assumed the simplest scenario where no natal kick is applied to the recently formed BH. This combined with the synchronization of the stellar spin and the orbit, translates into BH's spins aligned with the orbital angular momentum.

The initial profile of the star was obtained from the 35OC KEPLER model calculated by Woosley and Heger (2006) of a $28M_\odot$ pre-SN helium star with $R_* = 0.76R_\odot$. We considered the innermost $3M_\odot$ of the pre-SN star to be the newly formed BH with $a_2(t = 0) = 0$, which we subsequently treat as a sink particle. After the removal of the inner core, we use a parameterized energy injection routine to mimic the supernova engine and derive the density and velocity profile of the expanding envelope. Specifically, the energy is parametrized as follows: $\mathrm{E_{SN}} = \zeta\ \mathrm{E_G}$, where $E_\mathrm{G} = 2.3 \times 10^{52}$erg is the binding energy of the pre-SN star. This energy is then deposited instantanously in a $1.5M_\odot$ mass shell located at the inner boundary between the BH and the stellar envelope.

The distribution that describe the ejecta is determined solely by the structure of the pre-SN star (Matzner & McKee, 1999; Woosley & Weaver, 1995) and is established by the hydrodynamics of the interaction. Initially, the shock propagates through the stellar material, pressurizing it and setting it into motion. Once the shock wave approaches the surface of the star, a rarefaction stage begins in which stellar material is accelerated by the entropy deposited by the shock. This stage terminates once the pressure ceases to be dynamically important and the material expands freely. Figure 2.1 shows the radial velocity profile of the envelope when the shock surfaces the stellar envelope for three different explosion energies: $\zeta = 0.1, 0.5$ and 0.9. The gray area shows the initial BH mass while the dashed lines show $M_2(t)$ at the time the shock reaches $r = R_*$. Despite the complicated hydrodynamical interaction, the density and pressure approach steep power laws in velocity as the material enters the rarefaction stage and the ejecta begins

to establish homologous expansion (Figure 2.1). For a given progenitor structure, the ensuing ejecta will take similar ejecta distributions.

When $\zeta \lesssim 1$, energy injection fails to unbind the star such that a sizable fraction of its mass eventually fallbacks onto the newly formed BH. If this takes place in a binary system (Batta et al., 2017), a non-negligible fraction of the bound material can expand to a radius comparable or larger than the binary's separation, thus immersing the BH companion in gas. The interaction of fallback material with the binary transfers orbital angular momentum to the gas, which upon accretion onto the orbiting BHs is finally transferred into spin angular momentum. Differences in ζ result in diverse accretion histories, which ultimately regulate the BHs' final masses and spins. It is to this topic that we now draw our attention.

2.3 FALLBACK SUPERNOVA IN BINARIES AND THE SPINS OF LIGO SOURCES

2.3.1 Spin Evolution of the Newly Formed Black Hole

Figure 2.2 shows the gas column density in the equatorial plane of the binary for three different simulations (from *top* to *bottom*) and at three different stages (*left* to *right*). Evolutionary times in Figure 2.2 are measured in units of the dynamical time of the pre-SN star: t_*. All simulations have $\zeta = 0.4$ but differ on the initial separation of the binary: $d_* = 2$ (*top* panel), $d_* = 3$ (*middle* panel) and $d_* = 5$ (*bottom panel*). The frames are centered on the newly formed BH and the dashed circles in the *left* panels show the size of the pre-SN star.

Flow dynamics are similar in all three simulations shown in Figure 2.2. First, the envelope expands to rapidly engulf the companion BH. A bow shock is created as a result of this initial interaction. It is, however, only when the slower moving material reaches the companion that the resulting torque can supply the envelope gas with sizable angular momentum. This envelope material will remain bound to the system and will form a disk around M_2 if restricted to the region within which orbiting gas is gravitationally bound to the newly formed BH. A disk, albeit lighter, also forms around M_1, whose final mass depends sensitively on the initial separation.

The total mass bound to M_2 is the same in all simulations, yet the fraction of angular

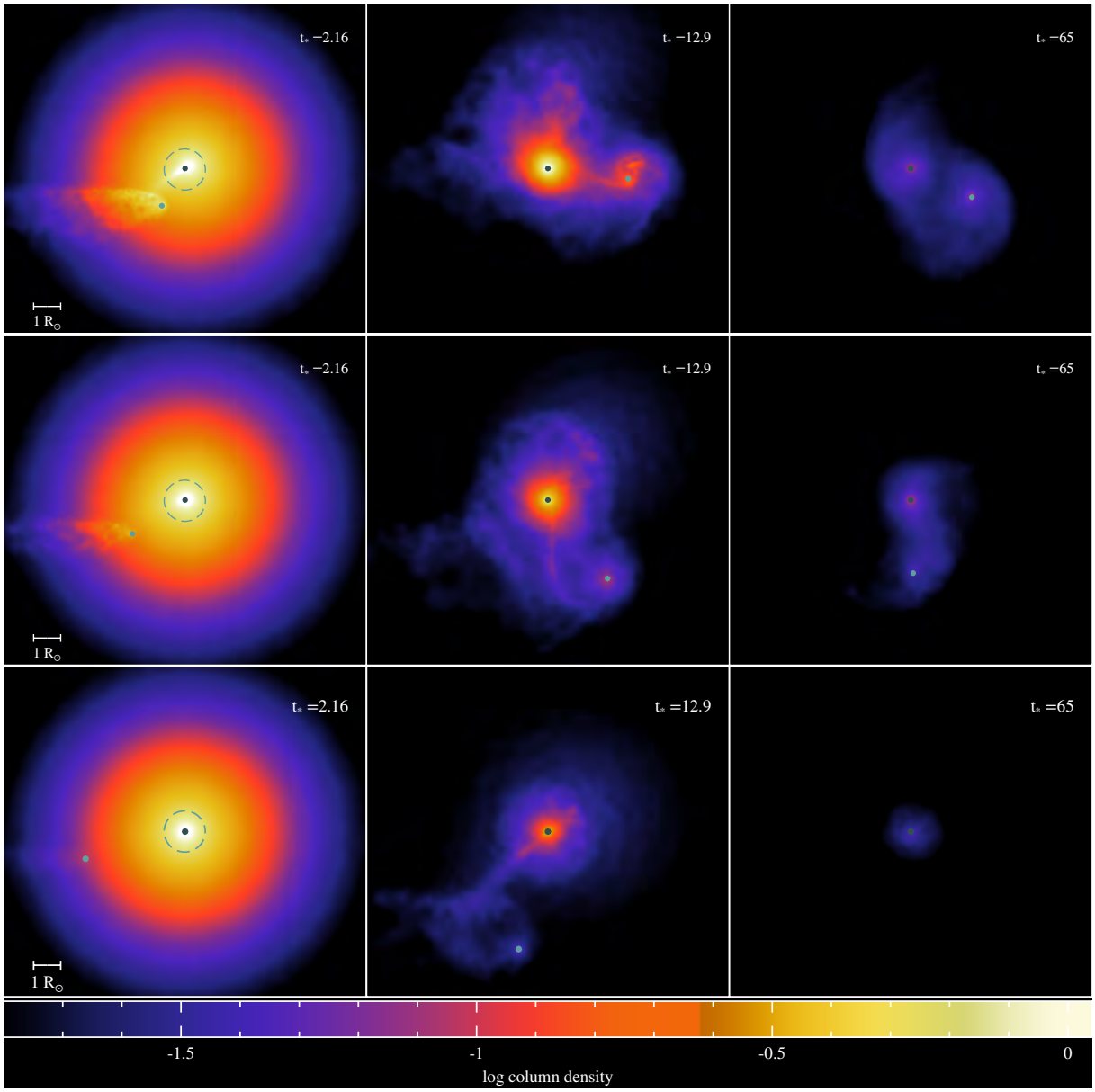

FIGURE 2.2 – Gas column density (code units) in the equatorial plane of the binary for three different initial separations (from *top* to *bottom*) and at three different evolutionary stages (*left* to *right*). The frames are centered on the newly formed BH (*black* circle) and the dashed circles in the left panels show the initial size of the pre-SN star. The *cyan* circle shows the companion BH. Times are measured in units of t_*. All simulations have $\zeta = 0.4$ but differ on the initial separation of the binary: $d_* = 2$ (*top* panel), $d_* = 3$ (*middle* panel) and $d_* = 5$ (*bottom* panel). In the last frame in the *bottom* panel, the resulting large binary separation places the companion outside the frame.

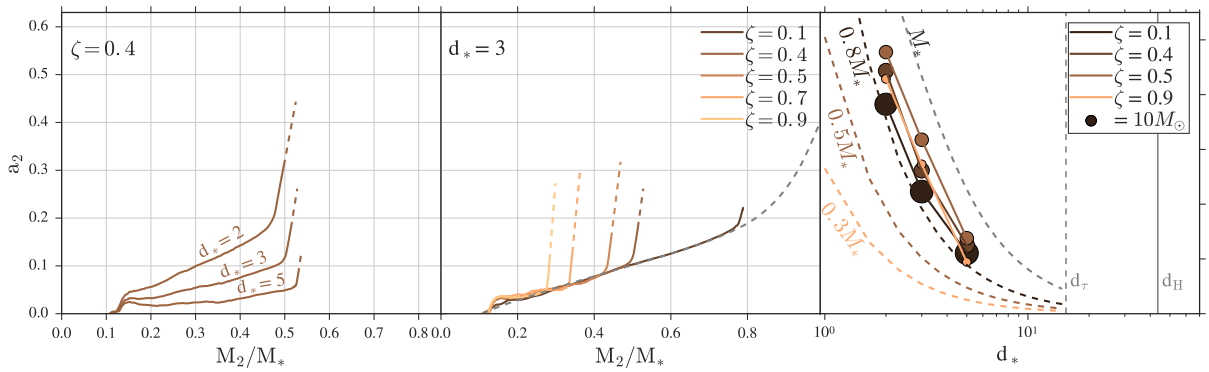

FIGURE 2.3 – The dependence of a_2 on ζ and d. *Left panel:* The spin parameter of M_2 as a function of the accreted mass in units of M_* for the three simulations shown in Figure 2.2. Here all simulations have $\zeta = 0.4$ and, as a result, the total accreted mass is similar. The *solid* lines correspond to the values derived from the simulations while the *dashed* lines indicates the expected mass and angular momentum accretion from material that remains in the disk (Bardeen, 1970; Thorne, 1974) when the simulation ends at $t = 80t_*$. *Middle panel:* The dependence of a_2 on ζ. All simulations shown have the same separation ($d = 3R_*$) but $\zeta = 0.1$, 0.4, 0.5, 0.7 and 0.9. The *dashed* line represents the spin expected from direct collapse (i.e., $\zeta = 0$). *Right panel:* The dependence of a_2 on d_* and ζ. The size of the symbols show the final BH mass, ranging from $8.2M_\odot$ to $22.5M_\odot$. The vertical *dashed* line shows d_τ, the radius for effective tidal synchronization (Zaldarriaga et al., 2018) and the vertical *solid* line shows $d_{\rm H}$, the binary separation required for merging within a Hubble time ($28M_\odot + 15M_\odot$). *Dashed* lines depict the spin expected from the direct collapse of different mass fractions, fM_*, of the pre-SN star with $f = 0.3, 0.5, 0.8, 1$.

momentum accreted increases with decreasing separation. As a result, a_2 is higher for progressively more compact binaries despite the final mass of M_2 reaching similar values. This can be seen in the *left* panel of Figure 2.3, in which we show the evolution of a_2 as a function of the accreted mass in units of M_*. Initially, a_2 increases as envelope material is accreted directly onto the BH. The innate angular momentum in this initial phase is determined by tidal synchronization, which increases as the binary separation decreases (Kushnir et al., 2016, 2017; Zaldarriaga et al., 2018). A transition in the evolution of a_2 is observed in the *left* panel in Figure 2.3 when material that is effectively torqued by the binary is able to form a disk and is subsequently accreted onto M_2. This material has a higher specific angular momentum than the one initially set by tidal synchronization and, when accreted, is able to spin up the newly formed BH at a faster rate. The resultant change in slope observed in the *left* panel in Figure 2.3 due to the

accretion of disk material is observed to occur earlier for smaller separations, which results in higher total spins values than those given by direct collapse of the same fallback material.

At a fixed ζ, the spin of the newly formed BH depends sensitively on d_*. For $d_* \lesssim 5$, the resultant torque on the fallback material can be considerable and, as a result, a_2 can be appreciable larger than the one expected from tidal synchronization. In this case, the final mass of M_2 remains unchanged while the final spin can vary drastically. The final mass of M_2 is, on the other hand, controlled by ζ. The *middle* panel in Figure 2.3 shows the evolution of a_2 for a fixed separation $d_* = 3$ and changing ζ. Initially, the spin evolution follows the trend expected from direct collapse. This is because the torque is unable to modify the original angular momentum of the promptly collapsing stellar material. A transition to disk accretion is seen in all cases, with the shift always occurring late in the mass accretion history of M_2. The resultant spin is similar in all cases due to the self similarity of the mass distribution of the expanding ejecta (Matzner & McKee, 1999), which results in a comparable mass ratio of directly falling stellar material to disk material for different values of ζ. For example this fraction varies from 5.3 % for $\zeta = 0.5$ to 7.6% for $\zeta = 0.9$ (see *middle* panel of Figure 2.3 for $d_* = 3$). This mass ratio is mainly responsible for determining the final spin of the BH and varies only slightly with ζ.

We have discussed, in the context of the *classical scenario*, the effects that the binary separation and the energy of the SN have on the resulting spin of the newly formed BH. The *right* panel of Figure 2.3 provides a clear summary of our findings as it shows the final spin of M_2 as function of d and ζ. The final mass of the newly formed BH is also shown by the size of the symbols. The masses for M_2 range from $22.5 M_\odot$ for $\zeta = 0.1$ ($M_2/M_* \approx 0.8$) to $8.2 M_\odot$ for $\zeta = 0.9$ ($M_2/M_* \approx 0.3$). Together with the results from our simulations we also plot the expected spin obtained from the direct collapse of the pre-SN stellar profile. This formalism makes use of the KEPLER model and assumes solid body rotation determined by tidal synchronization. Then, by assuming the spherical collapse of the star, we obtain the BH's spin a_2 for different fractions $f = 0.3, 0.5, 0.8, 1$ of the collapsed stellar mass M_*. If the entire star was to collapse directly onto a BH, this will give a final spin a_2 solely dependent on d, as predicted by the *dashed* line in Figure 2.3 labeled M_*.

When ζ is small and a significant fraction of the material is promptly accreted by

the BH, the simple direct collapse formalism provides an accurate description of the final spin of the newly formed BH. This can be seen by comparing the *dashed* line in Figure 2.3 labeled $0.8M_*$ with the simulation results obtained for $\zeta = 0.1$, which give BHs with $M_2 \approx 0.8M_*$ and final spins that closely resemble the direct collapse ones. By contrast, when $fM_* \lesssim M_*$, the final spin is significantly higher than the one predicted by direct collapse of the same enclosed material. This is because in such cases the fallback material is effectively torqued by the BH companion, which results in disk formation and consequentially higher final spin values. Binary BH formation in the *classical scenario* depends critically on the currently poorly constrained energy of the resulting SN, which for fallback-mediated remnant growth results in faster spinning BHs than what would have been attainable for a single star progenitor.

2.3.2 Spin Evolution of the Orbiting Black Hole

Figure 2.4 shows the dependence of a_1 and M_1 on ζ and d. In contrast to M_2, the final mass of the companion BH is only weakly altered by changes in ζ. The reason is that a comparatively small mass can be effectively restricted to the region within which the expanding envelope material is gravitationally bound to M_1. This bound material forms a disk whose final mass depends on both d and ζ. The resultant changes in a_1, under the assumption of $a_1(t = 0) = 0$, are observed to be more pronounced when the initial binary separation changes. Although, as expected, no sizable changes take place at large separations given that only a tiny fraction of the companion's envelope can be under the gravitational influence of M_1. We note here that values of $a_1 \lesssim 0.08$, involving the accretion of a small number of particles, are not converged at the resolution used in this study. The final value of a_1 shows a modest variation with SN energy with a small preference for $\zeta \approx 0.5$ at small separations. This indicates that although the ejecta distributions are similar for changing values of ζ, the fraction of bound material to M_1 is largest for this particular explosion energy, although its exact value is likely to change for different pre-SN progenitors.

2.4 DISCUSSION

In this *Letter* we have explored within the *classical* binary scenario how the spin of LIGO sources vary when the remnant BH is formed in weak SN explosions instead of direct

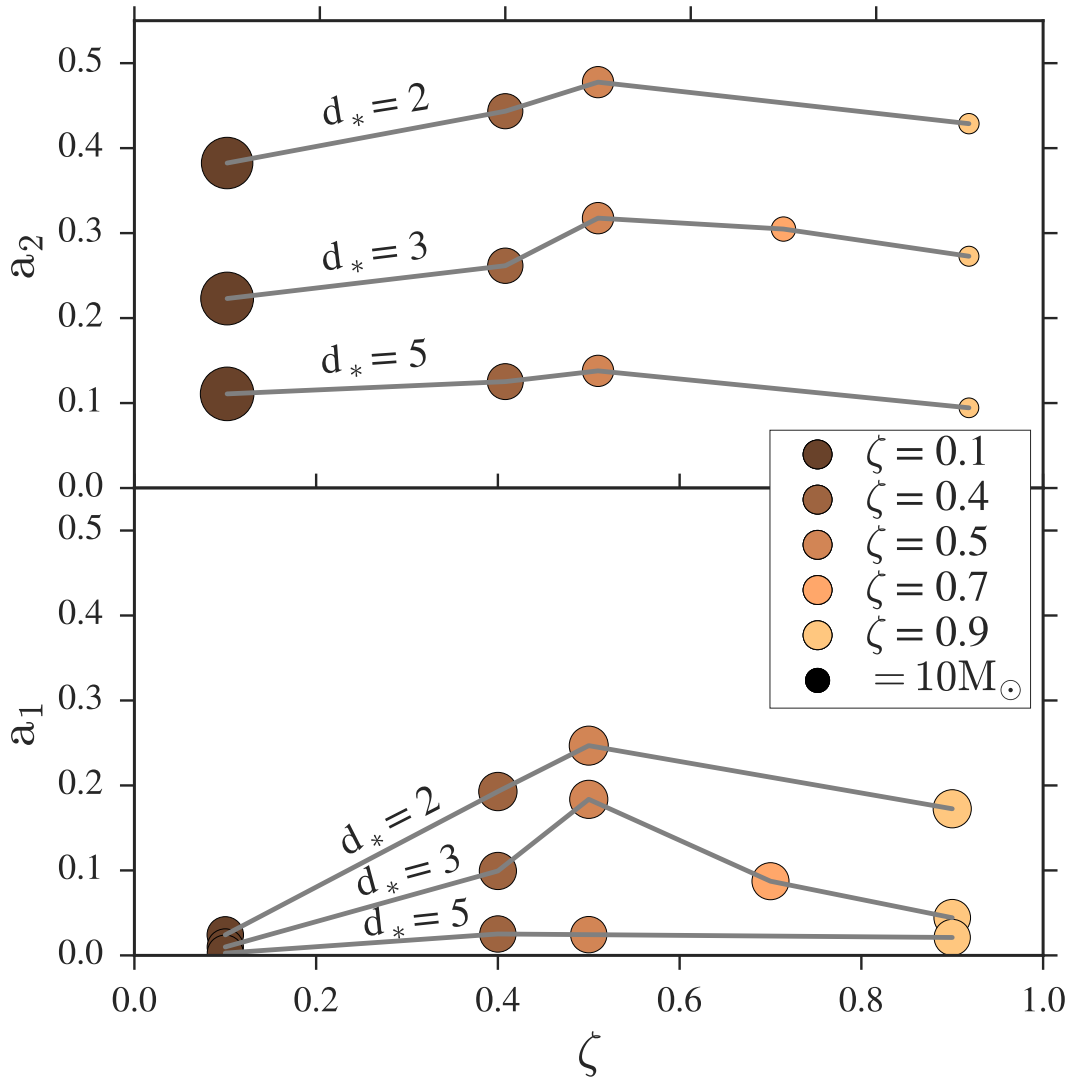

FIGURE 2.4 – The dependence of a_1 and a_2 on both ζ and d. The size of the symbols depicts the value of the final mass of the BH. *Top panel*: a_2 as a function ζ for initial $d_* = 2$, $d_* = 3$ and $d_* = 5$. *Bottom panel*: a_1 as a function ζ for initial $d_* = 2$, $d_* = 3$ and $d_* = 5$, under the assumption that M_1 had no spin before the final SN explosion $a_1(t = 0) = 0$.

collapse. Our key findings are summarized below.

- The final mass of the newly formed BH depends on the explosion energy. Its mass varies from $M_2 \approx 0.8 M_*$ for $\zeta = 0.1$ to $M_2 \approx 0.3 M_*$ for $\zeta = 0.9$ (Figure 2.1).
- At a fixed SN energy, the final spin increases significantly with decreasing d as a larger fraction of the fallback material is torqued by the companion. This results in similar mass BHs but with widely different spins (see *left* panel in Figure 2.3).
- Due to the self similarity of the mass distribution of the expanding ejecta, the final spin of the BH varies only slightly with ζ. This results in BHs with a wide range in masses but similar spins (see *middle* panel in Figure 2.3).
- In the presence of a companion, the final spin of a BH formed by a fallback SN explosion can be significantly higher than the one predicted by direct collapse of the same stellar material (see *right* panel in Figure 2.3).
- The spin of the BH companion, on the other hand, depends on both ζ and d. This is because its accretion history is determined by the amount of fallback material that it is able to seize (Figure 2.4).

In Figure 2.5 we present a comparison of our results (*upper* panel) in the context of both direct collapse solutions and current LIGO observations of binary BHs. Shown are $\chi_{\rm eff}$ as a function of the chirp mass, $\mathcal{M}$, of the resulting BH binary system. The shaded quadrilateral regions (*upper* and *lower* panel) show systems produced by the direct collapse of pre-SN helium stars of varying masses, whose structures have been taken from the KEPLER models of Woosley and Heger (2006). The final spin of M_2 is calculated using the radial stellar profile and assuming rigid body rotation of the tidally synchronized SN progenitor. The pre-SN helium stars (M_*) are assumed to be orbiting around a BH with $M_1 = qM_*$ and a_1=0. The dependence of $\chi_{\rm eff}$ with $\mathcal{M}$ is obtained by varying q from 0.53 to 1 in all cases, while the dependence of $\chi_{\rm eff}$ at a fixed $\mathcal{M}$ is obtained by changing d from $2R_*$ to $5R_*$ at constant q. To facilitate comparisons, we plot as shaded ellipses the 90% credibility intervals of the GW signals measured so far (LIGO Scientific & Virgo Collaboration, 2017; LIGO Scientific Collaboration & VIRGO Collaboration, 2016; LIGO Scientific Collaboration & Virgo Collaboration, 2016b; LIGO Scientific Collaboration, Virgo Collaboration, & Burns, 2017; LIGO Scientific Collaboration, Virgo Collaboration, & South Africa/MeerKAT, 2017) .

Some points should be emphasized. The current LIGO observations are inconsistent with the direct collapse of pre-SN helium stars in close binaries (Hotokezaka & Piran,

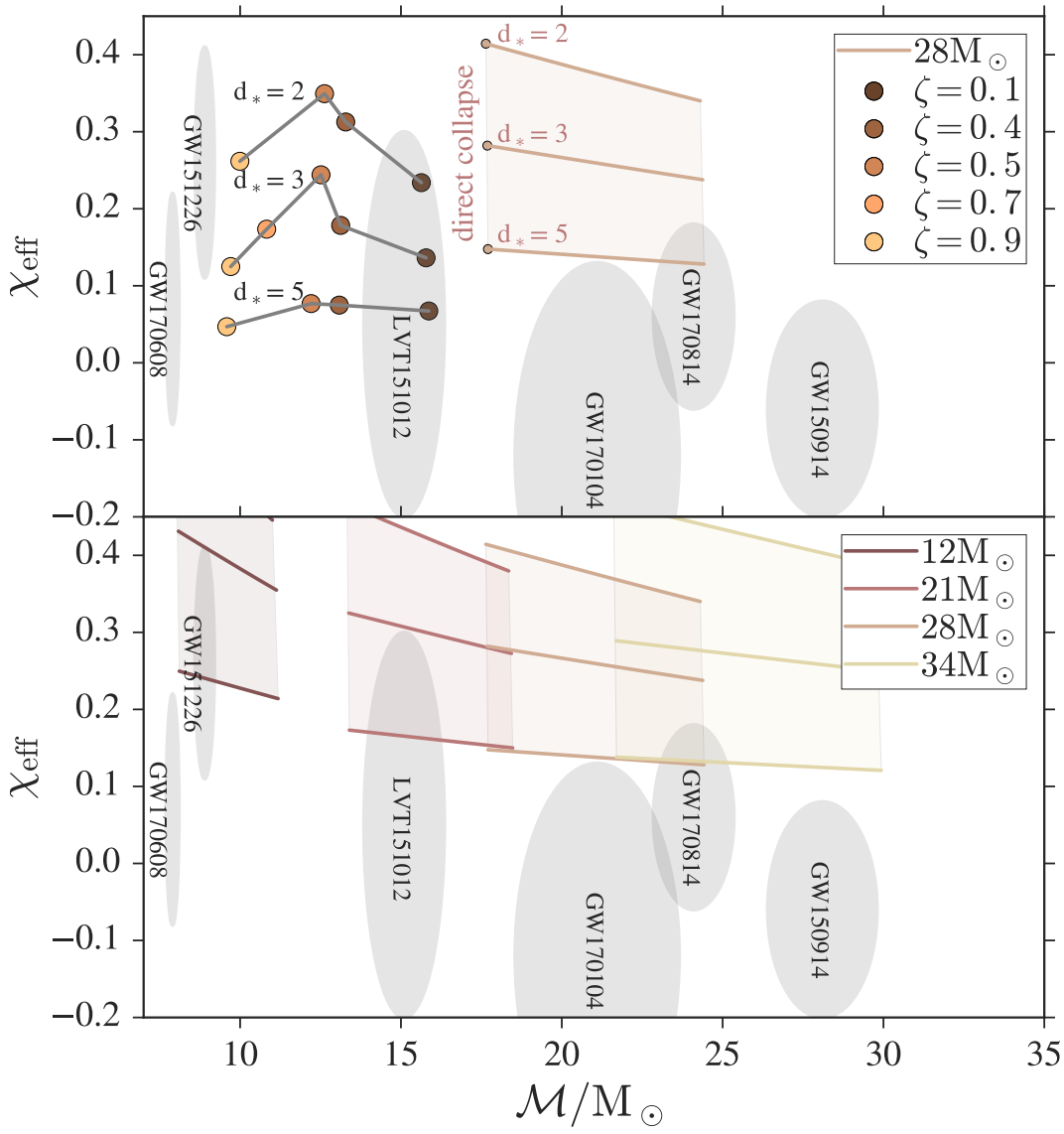

FIGURE 2.5 – $\chi_{\rm eff}$ as a function of $\mathcal{M}$. *Top* panel: The results of our simulations ($28M_\odot + 15M_\odot$, $q = 0.53$) for varying ζ and d. The shaded region show the outcomes produced by the direct collapse of the $28M_\odot$ pre-SN helium star calculated by varying q from 0.53 to 1 and d from $2R_*$ to $5R_*$. *Bottom* panel: The shaded quadrilateral regions show systems produced by the direct collapse of stars of varying $M_* = [12, 34]M_\odot$, $q = [0.53, 1]$ and $d = [2, 5]R_*$. The corresponding stellar radius are $0.66R_\odot(12M_\odot)$, $0.56R_\odot(21M_\odot)$ and $0.49R_\odot(34M_\odot)$. The shaded ellipses in both panels show the 90% credibility intervals of the GW signals measured by LIGO.

2017; Kushnir et al., 2016; Zaldarriaga et al., 2018). When the assumption of direct collapse is relaxed, the mass of M_2 can be altered by small changes on the explosion energy ζ while a_2 and a_1 (to a lesser extent) depend primarily on d (Figure 2.4). For the specific $28M_\odot + 15M_\odot$ system studied here, we show that changes in ζ alone can produce systems like LVT151012 ($\zeta = 0.1$, $d_* = 5$) or GW170608 ($\zeta = 0.9$, $d_* = 5$). For a fixed SN energy of $\zeta = 0.9$, changes in the initial separation can, on the other hand, yield systems like GW170608 ($d_* = 5$) or GW151226 ($d_* = 2$).

Irrespective of the exact progenitor system, the processes discussed here implies that the formation pathways of LIGO binary BHs are more complicated than the standard scenario suggests. But the effects are especially interesting for weak SN explosions taking place in close binary systems. Future LIGO observations can offer clues to the nature of the SN explosion leading to the formation of BHs, which is currently not well understood (Perna et al., 2014; Raithel et al., 2018; Sukhbold et al., 2016). For instance, GW170608 could be indicative of weak SN explosion of a more massive pre-SN progenitor system while GW151226 might arise due to direct collapse of a lighter, yet more compact progenitor system.

The properties of LIGO sources in the $(\chi_{\rm eff}, \mathcal{M})$ plane is diverse. One appealing aspect of the classical scenario is that the great variety of binary and explosion parameters can probably help explain this diversity. Given the need for a large helium core mass in progenitors, BH formation may be favored not only by slow rotation but also by low metallicity (Izzard et al., 2004). Larger mass helium cores might have less energetic explosions but this is currently highly uncertain. Many massive stars may produce supernovae by forming neutron stars in spherically symmetric explosions, but some may fail during neutrino energy deposition, forming BHs in the centre of the star (Fryer et al., 2012; Pejcha & Thompson, 2015; Ugliano et al., 2012) and possibly a wide range of weak SN explosions (Batta et al., 2017; Dexter & Kasen, 2013; Fernández et al., 2018; Fryer et al., 2012; Lovegrove & Woosley, 2013; T. Moriya et al., 2010). Asymmetric SN explosions, which might be a natural consequence of BH formation, could change the results presented in this study. However, Chan et al. (2018) recently showed that the structure of the fallback material can only be significantly modified by asymmetries when the explosion is strong ($\zeta \gtrsim 1$) and, as such, we expect our results to be representative of weak SN models. One expects various outcomes ranging from very massive BHs with low spins (GW150914), to lighter and faster spinning BHs

(GW151226). The number density of binary BHs of different masses and spins would provide a natural test to distinguish between different stellar explosion avenues.

CHAPTER 3

Fallback Supernova Assembly of Heavy Binary Neutron Stars and Light Black Hole-Neutron Star Pairs

---

This chapter is based on the following article:

"Fallback Supernova Assembly of Heavy Binary Neutron Stars and Light Black Hole-Neutron Star Pairs and the Common Stellar Ancestry of GW190425 and GW200115"

APJl, Volume 920, Issue 1, id.L17, 12 pp.(2021)

ArXiv e-prints: arXiv:2106.12381.

Authors: Alejandro Vigna-Gómez, Sophie Lund Schrøder, Enrico Ramirez-Ruiz, David R. Aguilera-Dena, Aldo Batta, Norbert Langer, Reinhold Willcox.

ABSTRACT

The detection of the unusually heavy binary neutron star merger GW190425 marked a stark contrast to the mass distribution from known Galactic pulsars in double neutron star binaries and gravitational-wave source GW170817. We suggest here a formation channel for heavy binary neutron stars and light black hole - neutron star binaries in which massive helium stars, which had their hydrogen envelope removed during a common envelope phase, remain compact and avoid mass transfer onto the neutron star companion, possibly avoiding pulsar recycling. We present three-dimensional simulations of the supernova explosion of the massive stripped helium star and follow the mass fallback evolution and the subsequent accretion onto the neutron star companion. We find that fallback leads to significant mass growth in the newly formed neutron star. This can explain the formation of heavy binary neutron star systems such as GW190425, as well as predict the assembly of light black hole - neutron star systems such as GW200115. This formation avenue is consistent with the observed mass-eccentricity correlation of binary neutron stars in the Milky Way. Finally, avoiding mass transfer suggests an unusually long spin-period population of pulsar binaries in our Galaxy.

3.1 INTRODUCTION

On April 25th, 2019, the LIGO-Virgo network detected its second-ever signal of two neutron stars merging, tagged as GW190425 (B. P. Abbott et al., 2020). But unlike the first detection of a binary neutron star (BNS) merger (GW170817, LIGO Scientific Collaboration & Virgo Collaboration, 2017c), which conformed to expectations, GW190425 was extraordinary. Most of what we know about neutron stars comes primarily from observations of pulsars, magnetized rotating neutron stars, in our own Milky Way. Of the thousands of known pulsars, almost twenty are visible as recycled millisecond pulsars paired with another neutron star companion (J. J. Andrews & Mandel, 2019; Tauris et al., 2017). These light neutron star binaries, including GW170817, weighed the equivalent of about 2.6 solar masses (Farrow et al., 2019; Kiziltan et al., 2013; Özel & Freire, 2016). By contrast, GW190425 has a total mass equal to about 3.4 solar masses (B. P. Abbott et al., 2020).

Since the detection of the Hulse–Taylor binary (Hulse & Taylor, 1975), there is

consensus that the progenitors of BNSs are massive stellar binaries (e.g., van den Heuvel, 1976). A crucial phase in the evolutionary pathway to BNS formation occurs when a giant star fills its Roche lobe and initiates a dynamically-unstable mass-transfer episode onto the neutron star companion (e.g., Bhattacharya & van den Heuvel, 1991). The stellar core and the neutron star become engulfed by the expanding envelope, a process where gas drag dissipates orbital energy of the binary (e.g., Ivanova, Justham, Chen, et al., 2013; MacLeod & Ramirez-Ruiz, 2015). This common envelope phase ends when the hydrogen envelope is ejected and a compact, stripped, helium-rich star of a few solar masses is left to reside in a tight ($\approx R_\odot$) near circular orbit (Fragos et al., 2019; Law-Smith et al., 2020). The subsequent evolution of the binary (Figure 1) depends on the mass and composition of the stripped helium star (Woosley, 2019) after the envelope is ejected. Most low-mass helium stars expand (e.g., Götberg et al., 2017; Laplace et al., 2020; Woosley & Weaver, 1995) and engage in an additional stable mass-transfer episode. During this episode, the mass transferred from the helium-rich donor recycles the pulsar, a process in which the neutron star spin increases to milliseconds and becomes radio visible for several Gyr (e.g., Srinivasan, 2010). Moreover, the donor star becomes an ultra-stripped core (Tauris et al., 2013; Tauris et al., 2015). These low-mass systems lead to BNSs such as GW170817 and those observed in the Milky Way (e.g., Ramirez-Ruiz et al., 2019).

In this *Letter* we propose an alternative channel formation channel for heavy BNSs. In this formation channel, massive ($\gtrsim 9\ M_\odot$) helium stars remain compact and avoid mass transfer onto a neutron star and thus pulsar recycling. Non-recycled, young, pulsars become radio quiet after only tens of Myr (e.g., Lorimer & Kramer, 2012; Tauris et al., 2017) and, as a result, these massive helium stars could lead to radio-quiet compact binaries that can only be detected by gravitational-wave observatories. The structure of the helium star at core collapse will determine if the system will become a BNS or black hole - neutron star (BH-NS) binary. These systems offer an alternative evolutionary pathway which can explain the dichotomy between the observed BNSs hosting recycled pulsars, GW170817, and the unusually heavy gravitational-wave source GW190425 (Figure 3.1).

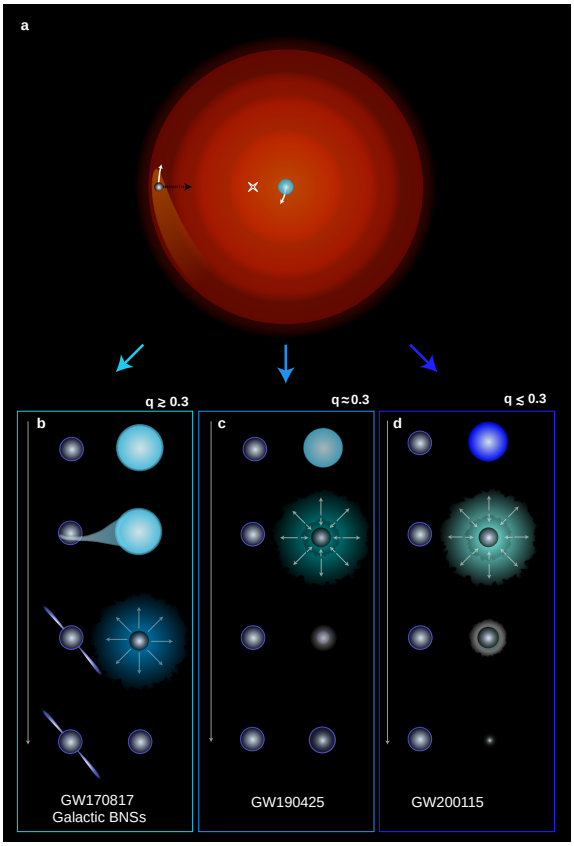

FIGURE 3.1 – Late stages of BNS formation. The giant star expands and engulfs the neutron star companion in an stage commonly referred to as a common-envelope evolution (**a**). A successful ejection of the envelope leaves the neutron star in a close orbit with a stripped-envelope star. The evolution of the system depends on the mass ratio $q = M_{\rm NS}/M_{\rm stripped}$. Less-massive stripped stars with $q \gtrsim 0.3$ experience an additional mass transfer phase that further strips the star and recycles the pulsar companion. Such evolutionary sequence leads to systems such as the observed BNSs in the Milky Way and GW170817 (**b**). More massive stripped stars with $q \approx 0.3$ do not expand as much, therefore avoiding further stripping and companion recycling. Such evolutionary sequence, on the other hand, is expected to lead to BNS systems such as GW190425 (**c**). Finally, even more massive stripped stars with $q \lesssim 0.3$ will lead to BH-NS binaries such as GW200115 (**d**).

3.2 METHODS AND INITIAL CONDITIONS

In this *Letter* we present three-dimensional (3D) hydrodynamic models of GW190425-like progenitor binaries using the smoothed-particle hydrodynamics (SPH) code GADGET-2 (Springel, 2005). Our approach is hybrid, since we approximate the evolution of a star that is stripped by a binary companion through a detailed stellar evolution of a single star, then map the pre-collapse 1D stellar model onto a 3D binary to model the explosion. To generate our initial models we make use of the one-dimensional (1D) stellar evolution code MESA (Paxton et al., 2011) version 10398. In particular, we model the evolution of a 10.0 $M_\odot$ stripped star at $Z = 0.02$ from helium zero-age main sequence to core collapse. At core collapse, the heavy helium star has a mass of $M_{\rm pre-SN} \approx 5.4\ M_\odot$, a radius of $\approx 0.7\ R_\odot$, and more than 95% of its gravitational binding energy contained below a radius of 0.01 $R_\odot$. The reader is refer to Appendix A.3 for specifics. We then map the MESA model into GADGET-2 in order to simulate the supernova explosion of a heavy helium star with a 1.3 $M_\odot$ neutron star companion at a separation of $a_{\rm pre-SN} = 1.4\ R_\odot$ in a circular orbit. Details on the setup and numerical tests can be found in Appendix A.4. The initial proto-neutron-star mass is assumed to be $M_{\rm proto-NS} = 1.3\ M_\odot$, consistent with the observed mass distribution of BNSs (Farrow et al., 2019; Kiziltan et al., 2013; Özel & Freire, 2016) and with the properties of the 1D pre-supernova stellar model (B. Müller et al., 2016). An explosion energy of 1.5 bethes[1], consistent with estimates from a 1D neutrino-hydrodynamics code for a similar progenitor model (Ertl et al., 2020), is deposited in a shell above the proto-neutron star. We focus on the long-term, post-explosion fallback evolution of the ejecta in order to account for mass accretion of the newly born neutron star and for pulsar recycling of the companion. We do not account for magnetic fields.

3.3 NEUTRON STAR BIRTH FROM SUPERNOVA FALLBACK

The resultant hydrodynamical evolution of the explosion is depicted in Figure 2. The shock initially propagates through the iron core until it reaches the envelope, fractions of a second after the explosion. At this point, a reverse shock wave emerges, which propagates back towards the newly-formed neutron star and triggers mass fallback.

[1] 1 bethe := 10^{51} erg.

The fallback mass accretion rate peaks 20 s after the explosion at $\approx 10^{-2}$ $M_\odot$ s^{-1} (Figure 3.2). Approximately 0.8 $M_\odot$ are accreted during the first hundred seconds after the explosion, roughly the same time scale in which the expanding layers of the exploding star reach the neutron star companion (Figure 3.2). The rapid velocity of the expanding shock (≈ 1000 km s^{-1}) and the small cross section of the neutron star companion result in $\lesssim 10^{-3}$ $M_\odot$ of accreted material. The accretion of this small amount of material will not effectively recycle the neutron star companion (e.g., Tauris et al., 2017).

After thousands of seconds the newly formed neutron star approaches a final mass of ≈ 2.1 $M_\odot$, a value in broad agreement with earlier results (Ertl et al., 2020; Fryer et al., 2012) in the literature. During the whole simulation the accretion rate remains above hypercritical (Chevalier, 1993) and neutrinos provide the main cooling mechanism until after $\approx 10^6$ s.

The amount of fallback mass accretion increases with decreasing explosion energy (Figure 3.3). Energies of $E_{\rm exp} \lesssim 0.5$ bethes lead to almost complete fallback while explosions energies of $E_{\rm exp} \gtrsim 2.5$ bethes lead to a complete ejection of the envelope. The fallback-dominated transition from neutron star to black hole remnants occurs at $E_{\rm exp} \lesssim 1.3$ bethes. Explosion energies between $1.3 \lesssim E_{\rm exp} \lesssim 2.4$ bethes lead to remnant masses $1.6 \lesssim M_{\rm rem,exp}/M_\odot \lesssim 2.7$, which are in the inferred range for the heavy neutron star in GW190425 (B. P. Abbott et al., 2020). Future detections of BNSs and BH-NS binaries would thus help improve the so far weak constrains of supernova explosion energies from massive helium stars.

The ejected envelope material during a supernova explosion imparts a recoil kick on the system. Even if the supernova is spherically-symmetric in the frame of reference of the exploding star, the explosion will increase the orbital period and eccentricity (Blaauw, 1961). If, on the other hand, the supernova material is ejected anisotropically, the magnitude of the resultant kick to the newly born neutron star is expected to be of the order of ≈ 100 km s^{-1} for isolated massive stars (e.g., Burrows & Vartanyan, 2021) and reduced to ≈ 10 km s^{-1} for ultra-stripped or electron-capture supernovae (e.g., Vigna-Gómez et al., 2018). BNSs assembled via common-envelope episodes end up in close orbits with relative orbital velocities well in excess of 1000 km s^{-1} and are likely to remain gravitationally bound after the explosion. Depending on the direction and magnitude of the natal kick, some binaries might actually end up shrinking to even closer orbits. The explosion of massive helium stars with a light neutron star companion

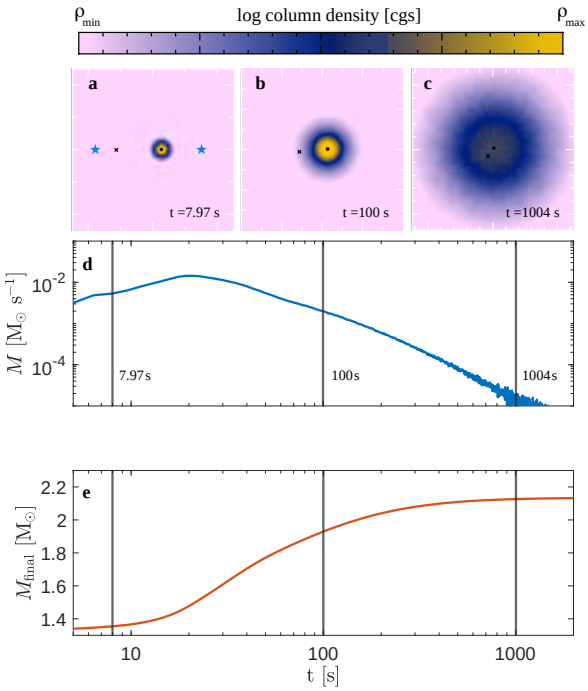

FIGURE 3.2 – The hydrodynamical evolution of the second supernova and the accompanying mass fallback that leads to a heavy BNS merger. Panels **(a)**-**(c)** show the column density (cgs units) in base 10 logarithmic scale and span [-1,3] in **(a)**, [-2,2] in **(b)** and [-3,1] in **(c)**. The location of the newly born neutron star is shown as a filled black circle and the companion neutron star is shown as a black cross. The second and third outer Lagrangian points of the binary are shown as blue stars in panel **(a)**. The tick marks on each panel correspond to a solar-radius scale. The only interaction with the neutron star companion is from the blasted ejecta and there is only a tiny mass of material accreted, implying that the pulsar companion will not be effectively recycled. Panels **(d)** and **(e)** show the fallback mass accretion rate onto the newly born neutron star and its cumulative mass accretion growth, both with vertical lines marking the snapshots from panels **(a)**-**(c)**.

are expected to lead to the formation of more eccentric binaries.

3.4 DISCUSSION AND CONCLUSIONS

3.4.1 Light BH-NS binaries and GW200115

On January 15th, 2020, the LIGO-Virgo network detected GW200115, the second ever confident detection of a BH-NS coalescence (Ligo Scientific Collaboration et al., 2021). GW200115 is composed of a neutron star and a black hole with masses of $1.5^{+0.7}_{-0.3}$ $M_\odot$

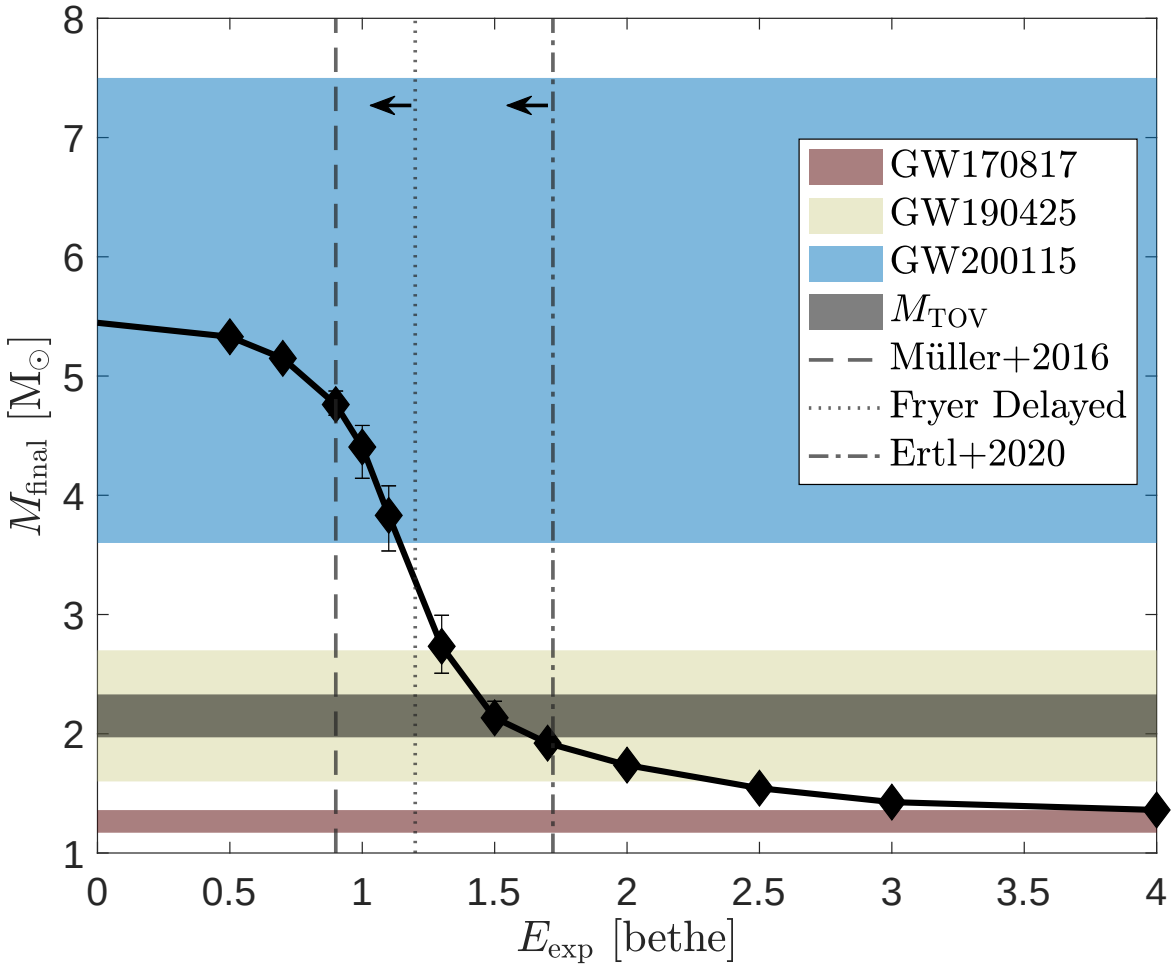

FIGURE 3.3 – Mass of the newly formed remnant as a function of the supernova explosion energy after the fallback accretion has ceased. The black diamonds represent the models explored in this work, and the thick solid black line is a linear interpolation between the values. The range of the component mass for gravitational-wave sources GW170817, GW190425, and GW200115 is shown in pink, beige, and blue, respectively, while the maximum mass of a non-rotating neutron star, $M_{\rm TOV}$ (Rezzolla et al., 2018), in shown in gray. For reference, the birth mass of the neutron star is 1.3 $M_\odot$, same as the mass of the neutron star companion. The semi-analytical prediction (B. Müller et al., 2016) of the explosion energy for this particular model is shown as a dashed black line. The upper limits of supernova models with explosion energies which include fallback are shown as dotted and dash-dotted lines (Ertl et al., 2020; Fryer et al., 2012). Main numerical uncertainties are included as error bars, some of them within the symbols.

and $5.7^{+1.8}_{-2.1}$ $M_\odot$, respectively. Such light BH-NS can be assembled via isolated binary evolution according to population studies (Broekgaarden & Berger, 2021). However, the component masses of GW200115 are peculiar. The mass of the neutron star is marginally more massive the 1.33 $M_\odot$ mean observed in Galactic BNSs mass distribution (Farrow et al., 2019). The black hole is close to lower side of the black hole mass distribution. This mass can be easily explained by the low explosion energies from our model (Figure 3.3).

According to the fallback model presented in this *Letter*, a helium star of 10.0 $M_\odot$ forms either a heavy neutron star or a light black hole. However, semi-analytical and numerical models predict that the remnant mass function does not necessarily increases monotonically with the mass at core collapse (Ertl et al., 2020; B. Müller et al., 2016; Sukhbold et al., 2016), and that the outcome depends on the structure of the stellar model as well as stochasticity in the explosion mechanism. Therefore, similar stars in similar binaries could lead to both heavy BNSs and light BH-NSs, and the fallback explosion mechanism might explain both simultaneously. The absence of one population could serve as a constrain on the explosion energy of stripped stars.

3.4.2 Mass-eccentricity correlation

There are hints of a mass-eccentricity correlation in short period (< 1 day) BNSs in the Milky Way, where millisecond pulsars paired with more massive companions (≈ 1.4 $M_\odot$) are in more eccentric (≈ 0.6) orbits (e.g., J. J. Andrews & Mandel, 2019; Tauris et al., 2017). The formation channel proposed here for GW190425 is consistent with this trend, as mass loss during the second supernova in heavy BNS formation can lead to large eccentricities. In contrast, the formation of light BH-NSs such as GW200115 will result in decreased mass loss during the second supernova, and would lead to low eccentricities at double compact object formation. The fallback scenario presented here thus provides an explanation for the observed mass-eccentricity correlation without the need to rely on a dynamical-formation scenario (J. J. Andrews & Mandel, 2019). To date, there is no evidence of heavy (> 2.9 $M_\odot$) BNSs in the Milky Way. This suggests at least one of the following three things about heavy BNSs: they have very short orbital periods ($\lesssim$ few hours) and thus avoid detection in acceleration searches (B. P. Abbott et al., 2020; Galaudage et al., 2021; Safarzadeh et al., 2020), they are radio quiescent, or such systems are rare in the Milky Way (Galaudage et al., 2021; Kruckow, 2020).

A priori, there is no reason why heavy BNSs should be preferentially born in short orbital periods (but see Romero-Shaw et al., 2020) and standard formation models are unable to predict enough fast mergers to be reconciled with the detection of GW190425 (Safarzadeh et al., 2020).

3.4.3 Electromagnetic counterparts and gravitational waves

The merger of a heavy neutron star pair or a light BH-NS binary is expected to produce an electromagnetic counterpart that will further shed light on its origin (Roberts et al., 2011). Particularly, the merger of a heavy neutron star pair is expected to produce a luminous red kilonova likely powered by an accretion disc wind (Kasen et al., 2017), which might likely be accompanied by a blue kilonova component (Metzger & Fernández, 2014). The merger of a light BH-NS binary, on the other hand, is expected to experience tidal disruption and be only observable as faint red kilonova (Kasen et al., 2017). The accompanying electromagnetic signatures would provide a natural test to distinguish between different compact binary mergers.

The formation channel presented here hints to the presence of heavy BNSs or light BH-NSs in the Milky Way. These and similar systems, such as non-recycled light BNSs (Belczyński & Kalogera, 2001), are expected to be uncovered by the Laser Interferometer Space Antenna (Amaro-Seoane et al., 2017; Lau et al., 2020).

3.4.4 Some open questions in stellar binary evolution

The evolution from zero-age main sequence to double compact formation is rather complex. We have assumed here that the evolution of the system follows the canonical assembly of BNSs (e.g., Bhattacharya & van den Heuvel, 1991; Tauris et al., 2017), which includes a common-envelope phase of a giant star with a neutron star companion (Fragos et al., 2019; Law-Smith et al., 2020). Vigna-Gómez et al., 2020 predicts that, at the onset of the common-envelope phase, only $\lesssim$ 5% of neutron star binary progenitors will have donor stars with masses $\gtrsim$ 20 $M_\odot$. However, that study does not incorporate the recently explored stellar evolution models of stripped stars (Appendix A.3) nor the explosion mechanism explored in this *Letter* (Appendix A.4). These updates are likely to alter the predictions of assembly and merger rates for heavy BNSs and light BH-NS binaries.

Single unperturbed stellar models have been used to explore envelope ejection in massive binaries (Klencki et al., 2021; Kruckow et al., 2016). Heavy ($\gtrsim$ 25 $M_\odot$) progenitors with low-mass (1 $M_\odot$) companions are not likely to eject the envelope at high ($\approx$ solar) metallicities, a scenario which has been predicted to result in Thorne–Żytkow objects (Thorne & Zytkow, 1975, 1977). However, it is possible that modeling of progenitors with more massive companions (cf. Figure 6 of Klencki et al., 2021), lower metallicities, or different assumptions about energy requirements (**2021arXiv210714526V**; Everson et al., 2020), might lead to a successful ejection.

For models considered in this *Letter*, we assumed that the orbit remains effectively unchanged after the envelope ejection. However, the evolution of the post-common-envelope binary can entail energy-momentum transfer and losses via, e.g., stellar winds and tidal dissipation. Mass loss via isotropic winds, aka the *Jeans* mode, can widen the orbit by a factor of $\lesssim 2$, and in some cases counteract stellar expansion and therefore Roche-lobe overflow. This is particularly relevant for stars with mass $6 \lesssim M_{\rm stripped}/M_\odot \lesssim 10$ that will expand by a factor of a few at most. Avoiding Roche-lobe overflow after the common-envelope phase would result in avoiding further pulsar recycling of the companion and leading to remnant masses $M_{\rm rem,exp} > 1.33\ M_\odot$. However, alternative mass loss modes or wind interaction with the companion could decrease the widening of the orbit (e.g., Schrøder et al., 2021).

Throughout this *Letter*, we do not consider tidal dissipation. The dynamical tide is unlikely to play a dominant role in the orbital evolution during late stages of BNS assembly, but it might (partially) counteract the widening of stellar winds.

3.4.5 Mass accretion onto a neutron star and pulsar recycling

A pulsar binary can be spun-up and recycled if angular momentum is efficiently transferred onto the pulsar. This is a complex process that depends on the mass transfer rate, orbital properties of the binary, and accretion physics, as well as on the equation-of-state, magnetic field, and overall properties of the neutron star (Tauris et al., 2017; Tauris et al., 2012). Roche-lobe overflow from a stripped-star with a helium-rich envelope is an efficient way to form an accretion disc around the pulsar that can spin it up to tens of milliseconds and (mildy) recycle it; this is believed to be the preferred spin-up mechanism for Galactic BNSs (Tauris et al., 2017). Avoiding such mass transfer episode, like we suggest in this *Letter*, will avoid the main mass and

angular momentum transfer mechanism, which for Galactic-like BNSs results in a mass growth of $6-9\times10^{-3}$ $M_\odot$ and observed[2] recycled pulsar spins between $17 < P_{\rm spin} < 186$ milliseconds (Stovall et al., 2018; Tauris et al., 2017).

However, post-common-envelope winds can also lead to mass accretion. For the system presented in this *Letter*, the amount of accreted mass $\Delta M_{\rm acc} = f_{\rm acc} \times \Delta M_{\rm winds}$, with $f_{\rm acc} \approx 10^{-4}$ is the estimated wind accretion efficiency (Tauris et al., 2017) and $\Delta M_{\rm winds} \approx 4.6$ $M_\odot$ is the amount of mass lost via stellar winds from the helium zero-age main sequence until core collapse (Appendix A.3), results in $\Delta M_{\rm acc} \approx 4.6\times10^{-4}$ $M_\odot$. This amount of mass increases the spin period to $P_{\rm spin} \approx 683$ milliseconds if this mass is accreted from a neutrino cooled disc (MacLeod & Ramirez-Ruiz, 2015). During the second supernova, a small fraction of the fast ejecta ($\approx 10^{-4}-10^{-3}$ $M_\odot$) is *ballistically* accreted onto the pulsar companion, and therefore we do not expect it to recycle the pulsar.

3.4.6 Conclusions

Our understanding of merging binaries has come a long way since the discovery of gravitational waves almost 6 years ago, but these enigmatic sources continue to offer major puzzles and challenges. Our results suggest that ground-based facilities, like LIGO and Virgo, will detect these merging binary populations which have currently avoided detection in the Milky Way. Space- and ground-based observations over the coming decade should allow us to uncover the detailed nature of these most remarkable systems and provide us with an exciting opportunity to study novel regimes of binary stellar evolution.

[2] We do not consider Galactic BNSs in Globular Clusters.

III

Em Counterparts from BH mergers

CHAPTER 4

Counterparts to LIGO mergers from leftover material in binary evolution

---

This chapter presents the following work in progress:

"Accretion Disk Formation in LIGO Black Hole Binaries and Electromagnetic Counterparts

Authors: Sophie Lund Schrøder, Enrico Ramirez-Ruiz.

4.1 INTRODUCTION

Observational astronomy is on at onset of large-scale, spatially and temporally systematic surveys and are revealing new fascinating transients. One of the uncertain and highly sought pieces in gravitational-wave astronomy is still missing: an electromagnetic counterpart to a binary black hole merger.
The observations of the neutron star (NS) merger GW170817 (LIGO Scientific Collaboration, Virgo Collaboration, & Burns, 2017) has already been a great achievement of multi messenger astronomy. GW170817 is the first NS merger detected both by LIGO, and across the entire optical frequency spectrum in the following kilonova event (Coulter et al., 2017).

GW170817 is also the only gravitational wave observation so far where an accompanying electromagnetic signal has been confirmed (Coulter et al., 2017; Hallinan et al., 2017; Kasliwal et al., 2017; LIGO Scientific Collaboration & Virgo Collaboration, 2017c; LIGO Scientific Collaboration, Virgo Collaboration, & Burns, 2017).

The other types of compact object mergers LIGO can detect are that of a black hole and NS (BHNS) or binary black hole (BBH) mergers. A short γ-ray burst could be produced by a BHNS merger (Foucart, 2021). The requirement for an electromagnetic signal is that there is gas present around the binary at the time of merger. But no NSBH merger has been observed electromagnetically so far, but the search is ongoing (Raaijmakers, Nissanke, et al., 2021).

But a γ-ray transient was observed temporally coincident with the the gravitational wave observation of GW150914, a BBH merger (Connaughton et al., 2018; Connaughton et al., 2016). Mergers from BBHs do not produce an electromagnetic signal, because there is no gas available from the BHs themselves. A BBH merger can only result in a signal, if there is material around the BHs at the time of merger.

GW150914 inspired large amount of work on possible ways to have gas present at the time of the merger. Suggestions include charged BHs (Fraschetti, 2018; Liebling & Palenzuela, 2016; B. Zhang, 2016), mergers in AGN disks (Bartos et al., 2017; Graham et al., 2020; N. C. Stone et al., 2017) or circumbinary disk remnant from field evolution

(de Mink & King, 2017; Kotera & Silk, 2016; Martin et al., 2018; Murase et al., 2016; Perna et al., 2019; Perna et al., 2016).

The large amounts of gas are expelled from the binary during phases om mass transfer would be ideal of building a circum binary disk. During for example a Common Envelope Event or wind mass loss up to ten solar masses worth of material can be ejected. Most of this material will be flung far away from the binary and not interact with the stars anymore, so we will here focus on the last mass loss event of the binary, that is the Supernova forming the second BH. Specifically we look at the formation of second BH formed in mild explosion called fallback supernova, where the stellar envelope is only partially ejected.

In this paper we will investigate the scenario for disk formation in a fallback supernova using Gadget-2 in section 4.2, then in section 4.3 we estimate the strength of the emergent electromagnetic signal from a binary formed in a fallback supernova. In section 4.4 we compare to possible electromagnetic signals for binaries moving through an interstellar medium or an active galactic nuclei disk. And finally in section 4.5 we conclude.

4.2 DISK FORMATION IN FALLBACK SN

The second supernova during the formation of binary BHs happens in a tight binary consisting of the first formed BH and a Helium star. To form the second BH the supernova explosion has to be weak compared to the binding energy of the Helium star, referred to as a fallback supernova, where most the envelope material falls back onto the remnant forming a BH.
To determine the amount of gas around the binary after the second supernova, we run two simulations of a fallback supernova in a binary. The simulations are done in a modified version of Gadget2 Springel, 2005 described in Batta et al., 2017. The initial setup maps the density structure from the 35OC KEPLER model calculated by Woosley and Heger, 2006 of a $28M_{\odot}$ pre-SN helium star with $R = 0.76R_{\odot}$ into a 3D star. In orbit around the Helium star is a BH of $15M_{\odot}$. The separation is set to $a = 2.3R_{\odot}$, making the separtion a three times the size of Helium star prior to explosion. The reader is referred

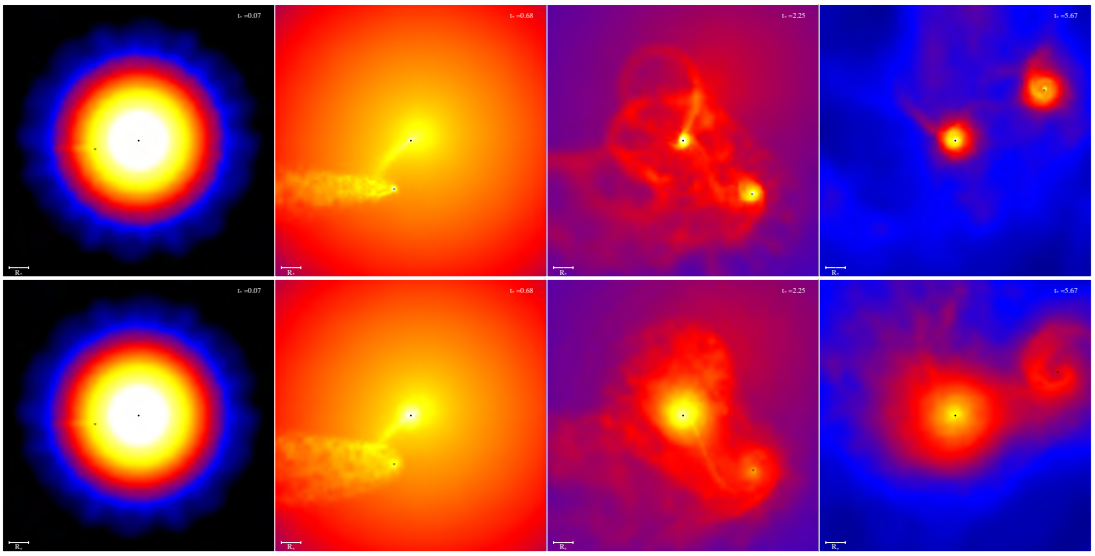

FIGURE 4.1 – Formation of disk during SN in binaries. Time line from simulation with 10^6 particles and adiabatic index $\gamma = 1.1$ and $\gamma = 5/3$. Panel shows log density in the orbital plane during the first orbit after the supernova. The plots are centered on the BH remnant from the exploding star.

to Batta et al., 2017 for further details on initial particle distribution and numerical accretion.

We start our simulations after the collapse of the core and consider the innermost $3M_\odot$ of the Helium star to be the newly formed BH, which is hereafter treated as a sink particle. To enact the supernova explosion we inject kinetic energy in a spherical layer of particles at the bottom of the envelope and proceed with the simulation to obtain the velocity and density profiles of the expanding envelope. We inject half the binding energy of the helium star as our supernova energy which is 1.2×10^{52}erg.

After the supernova shock has surfaced the envelope the ejecta continues to expand beyond the binary separation. The interaction between the supernova ejecta and the two BHs is showed in figure 4.1. We show $\log(\rho)$ in the orbital plane during the first orbit after the supernova. The frames are centered on the remnant from supernova and the timestep is in units of $\sqrt{\frac{R_*^3}{GM_*}}$. After simulating the shock breaking through the surface of the star, we halt the simulation. From here on we restart with two different adiabatic indices γ, one with $\gamma = 1.1$ (top row) and one with $\gamma = 5/3$ (bottom row). We do this to investigate the effect of cooling in the disk accretion without having to factor in different velocity and density profiles of the ejecta.

For both simulations we now follow the interaction of the BHs and gas material. Because the supernova energy is less than the binding energy of the Helium star we expect large amounts of fallback. Material deep within the envelope never gains much kinetic energy despite the shock passing through it. This material falls back immediately and is accreted by the new BH. The outer layers of the envelope has a steeply declining density gradient, where the supernova shock accelerates. This material will be driven to high velocities and be expelled from the binary. The ejecta material on the turning point between direct collapse and strong expulsion has enough kinetic energy to expand, but is still bound to the system. This material will interact with the companion before collapsing on the binary. and is shared between the now two BHs. As we see in the frames of figure 4.1 within the first orbit this material gains enough angular momentum from the binary to settle into disks around the BHs.

The ability to cool and compress changes the extend of the disks. The simulation with $\gamma = 5/3$ has visibly larger accretion disks than the $\gamma = 1.1$ simulation.

The extra pressure support also means that the accretion rate is slower. In figure 4.2 we show the accretion rate of the the remnant and the companion after the explosion has started. Brown lines show the simulations with $\gamma = 1.1$ and yellow lines show accretion rates from the simulation with $\gamma = 5/3$, with the solid lines showing accretion rates for the remnant and dashed lines showing accretion rate for the companion. The gray dashed lines show a fitted power law too the disk accretion.

Initially the accretion on the remnant is the same for both simulations, as the shock breakout is simulated with the same equation of state. After $t = 4 \times 10^{-4}$ days, the simulations are continued with different γ values. Initially the collapsing material has very little angular momentum and is accreted directly by the remnant, and the accretion is very efficient. As more high angular momentum material collapses back on the black hole, the accretion rate slows down towards disk accretion. The last infalling material is shock reversely by the fluffy disk, creating a drastic drop in accretion clearly seen in remnant accretion for the simulation with $\gamma = 5/3$. For the simulation with $\gamma = 1.1$ this reverse shock is not as strong, as the lower pressure balance allow the disk to contract more. After the reverse shock, the disk around the remnant is not fed anymore material, and the accretion rate continues to decrease approximately following a power law slope. Around $t = 10^{-3}$ days the SN shock reaches the companion, and captured material is accreted. The accretion rate increases as the slower moving material behind the shock

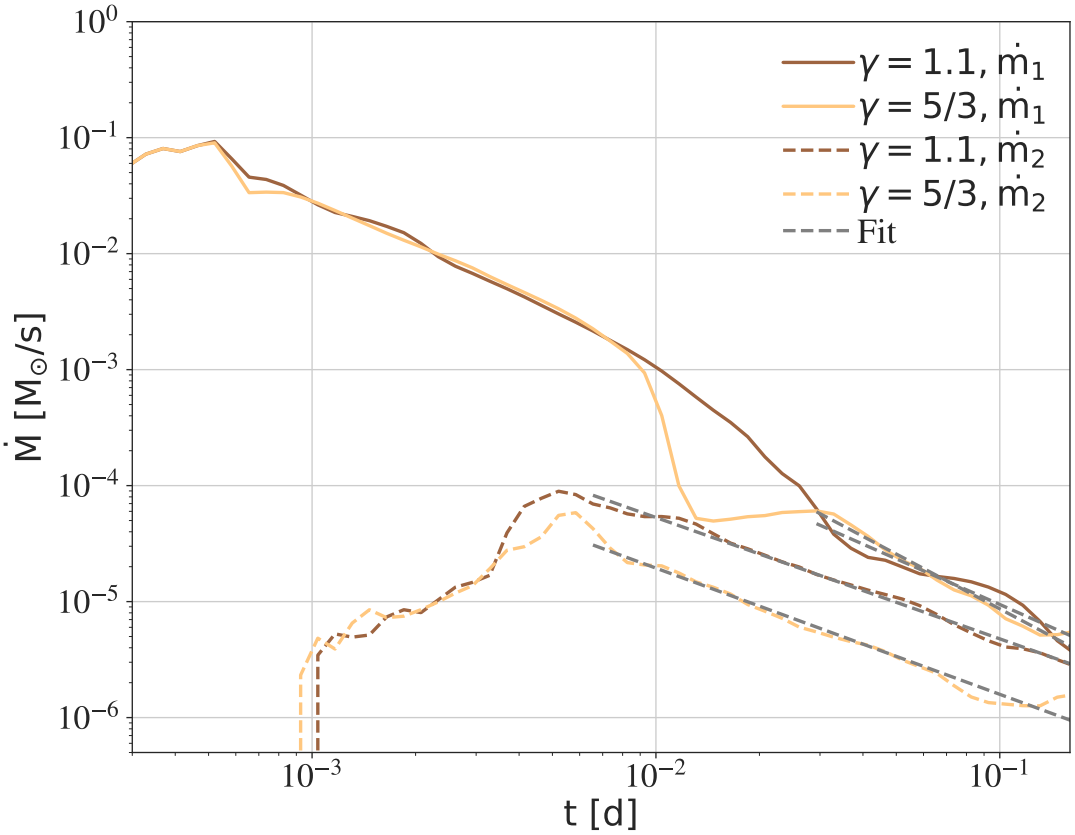

FIGURE 4.2 – Accretion rates from fallback simulations. Solid line show accretion for the young remnant, and dashed lines show accretion for the companion. Gray dashed lines show fit of the accretion rates after disk formation.

also reaches the companion. Around $t = 5 \times 10^{-3}$ days, the ejecta has escaped the binary and what is remaining is the material with high angular momentum, which is accreted viscously from the disk. The simulation with $\gamma = 1.1$ has higher accretion rate as the disk is more compact and the viscous accretion time is shorter.

4.3 LUMINOSITY AT TIME OF MERGER

To Estimate the luminosity at time of merger, we fit the accretion rate after the ejecta has settled into accretion disks. The fit can be seen as gray dashed lines in figure 4.2.

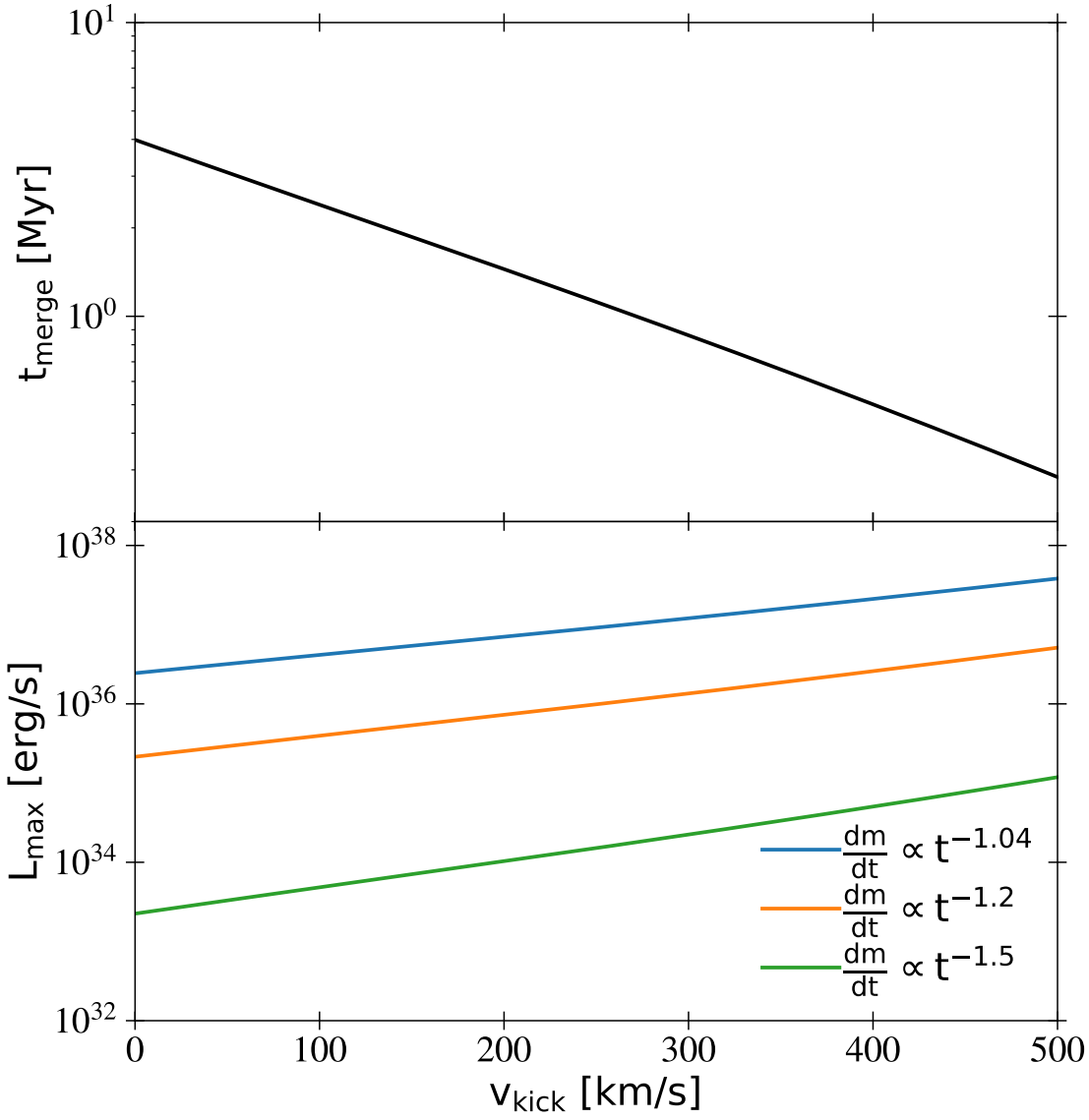

FIGURE 4.3 – Maximum luminosity based on fits of accretion rates during SN fallback at time of merger.

We fit the accretion rate with power laws and find the accretion to decrease $\dot{M}_{\rm BH} \propto t^{-\beta}$, where β ranges from 1.4 to 1.5.
What the exact accretion should be depends on the state of the disk. Perna et al., 2016 argues that accretion turn of when the disks get cold and neutral, because the magneto-rotational instability (MRI) no longer works.However, Perna et al., 2016 does not include the effect of spiral shocks, which can generate an effective α-viscosity similar to that of the MRI.

In the top panel of figure 4.3 we compute the time until merger for our post-SN orbit, now including a supernova kick. The kick is assumed to be in the exact opposite direction of binary, which will give the shortest possible merger time for a given kick velocity, and the merger time gets shorter the larger the kick velocity is.
To get the accretion luminosity at time of merger, we assume the accretion continues to decrease according to our fitted power law from figure 4.2. We assume the luminosity of the accreting black holes to be $L = \eta \dot{m} c^2$, with $\eta = 0.1$. We plot the luminosity at time of merger for different kick velocities in the bottom panel of figure 4.2.

4.4 COMPARING TO ACCRETION FROM SURROUNDING MEDIUM

In figure 4.4 we translate the accretion luminosity from figure 4.2 into a Hoyle Little accretion density. Density is then given by

$$\rho = \frac{\dot{m} v_\infty^3}{4\pi (G(m_1 + m_2)^2} \tag{4.1}$$

where $\dot{m}$ is the accretion according to the fit from figure 4.2 and v_∞ is the center of mass velocity of the system after the supernova including the kick. We plot this density for a range of merger times based on the range of kick velocities shown in figure 4.3. The color sections of figure 4.4 correspond to densities of the inter stellar medium (ISM) and an active galactic nuclei (AGN) disk.

We see that the density from fallback SN fall in between the less dense ISM and the much denser AGN. Luminosities from a binary black hole moving through the ISM would in

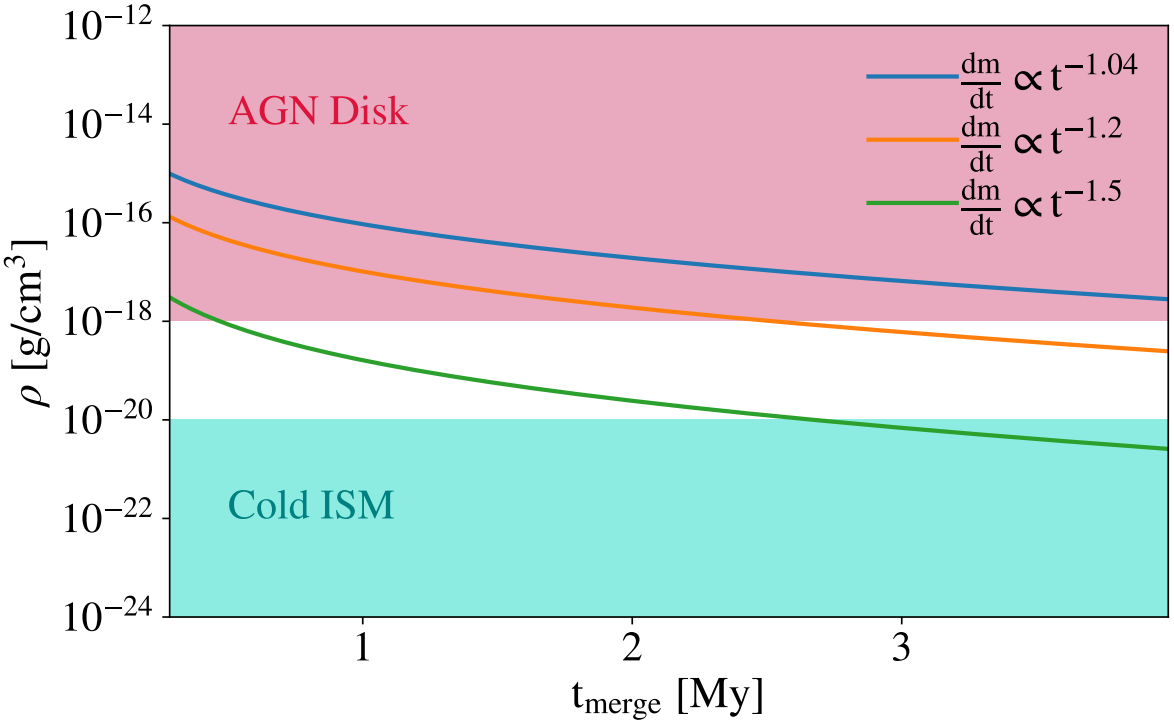

FIGURE 4.4 – Accretion rate density compared to critical density needed from Hoyle Littleton. To get as high accretion and emission as SN fallback disk accretion, ISM is not dense enough and AGN is denser.

general also be smaller than the fallback disk luminosities, whereas luminosities from a binary moving through an AGN disk would be larger than that of fallback SN.

4.5 CONCLUSIONS

In this paper we have investigated the characteristics of an electromagnetic counterpart to a BH merger assuming the second BH was formed in a fallback SN.
In section 4.2 we describe the disk formation from SN ejecta, in the case of a weak fallback SN. The expanding ejecta is torqued by the companion and angular momentum is transferred from the orbit to ejecta material. As the material collapses back on the black holes, it now has high enough angular momentum to settle into mini disks around each BH.
We found that the accretion rate depends on the disk material's ability to cool and settle

in smaller disks with less pressure support (see figure 4.2). By fitting the accretion rate, we predict the accretion luminosity at time of merger for systems formed in symmetric explosions. We also investigate the impact of kicks, and find that favorable kicks can increase the accretion luminosity at time of merger by an order of magnitude as shown in figure **??**.

Lastly we compare to the expected accretion rates for binary BHs moving through either the ISM or orbiting in an AGN disk. We find that systems in the ISM are even less bright than systems in with fallback disks, but that systems orbiting in AGN disk have higher surrounding densities and therefore would result in brighter EM counterparts.

IV

Conclusions

CHAPTER 5

Conclusions & outlook

The aim of this thesis has been to investigate the evolution of compact binary stars to gravitational wave sources via hydrodynamical simulations of interacting stellar binaries. I have studied mass-transfer stability and instability, along with the explosive outcomes of binary mergers within the evolution of compact binaries.

Altogether, the main findings and contributions of the doctoral research to the field are:

In chapter 1, we produced models for merger-driven explosions that arise as a result of the merger between a star and compact object following a CE event. In the case where a compact object merges with the core of a massive, post main-sequence star, accretion onto the compact object is rapid enough to produce a neutrino-cooled a disk. This event is accompanied by the release of approximately 10^{51} erg into the surrounding hydrogen envelope, leading to a merger-induced explosion. The coalescence of star and compact object during the CE phase expels the envelope material into the surrounding environment, forming a dense, toroidal CSM. This CSM distribution is decisive in shaping the transient light curves, with merger-driven explosions brightened by up to three magnitudes relative to their explosions of similar energies in hydrostatic stars.

These light curve shapes vary with the specific donor-star mass and radius and the explosion energy. The interaction with the CSM generally brightens NS mergers by one magnitude and BH mergers by three magnitudes compared to type IIP models with the same explosion energy.
Using population models, we showed that BH and NS mergers with giant star companions happen at similar frequency with a rate per mass of stars formed of $\sim 1.25 \times 10^{-5} M_{\odot}^{-1}$. And in our models, the combined rate of both types of mergers was 0.5% of the total core-collapse rate.
Future work could improve on the treatment of the stellar model and the details of energy injection into the expelled envelope material. In the current study, we inject energy spherically into the envelope at one tenth the star's radius. But the exact location and asymmetry of energy injection might play a key role in shaping transient light curves. In fact one of the possible identifications strategies for finding merger-driven explosions include their asymmetry and polarization of light due to the toroidal CSM, as well as the properties of the progenitor binaries and X-ray emission from the remnant.

In chapter 2 we explored how the spin of LIGO sources vary when the remnant BH is formed in fallback SN explosions instead of direct collapse. We found that the two key parameters are the explosion energy and pre-SN binary separation. The final mass of the newly formed BH depends on the explosion energy, as the more injected energy expels more of the envelope material. The final spin on the other hand depends mostly on the pre-SN binary separation, because a closer in companion can torque more of the collapsing materiel.
Interestingly, the self similarity of the mass distribution of the expanding ejecta makes the final spin of the remnant BH vary only slightly with explosion energy. This is because this particular ejecta distribution causes the ratio of directly collapsing material and material accreted with high angular momentum to be alike for a range of SN energies. The result is a collection of BHs with different masses but similar spins.
The spin of the BH companion depends on both SN energy and pre-SN binary separation, as the fraction of material captured during the explosion determines its final mass and spin. The companions mass and spin has a much more fine tuned link to the specific pre-SN stellar profile, as the exact amount of material arriving within the companions capture radius vary with energy distribution in the ejecta. We also compared

the results to the measured values of $\mathcal{M}$ and $\chi_{\rm eff}$ to observed LIGO sources, and found that the observed BH systems with smaller $\mathcal{M}$ and positive $\chi_{\rm eff}$ fits the systems formed in fallback SN.
In chapter 3 we propose fallback SN to have been present in the formation of GW200115. GW200115 is a BH-NS coalescence and composed of a neutron star and a black hole with masses of $1.5^{+0.7}_{-0.3}$ $M_\odot$ and $5.7^{+1.8}_{-2.1}$ $M_\odot$, respectively. These mass estimates are both peculiar when formed during standard binary evolution. The neutron star mass is slightly more massive the 1.33 $M_\odot$ mean observed for Galactic BNSs. And the BH is close to lower side of the BH mass distribution. We are able to form this system by incorporating fallback SN in the formation, where a helium star of 10.0 $M_\odot$ forms either a heavy neutron star or a light black hole.
The formation channel also hints to the presence of heavy BNSs or light BH-NSs in the Milky Way, which are expected to be observed by the Laser Interferometer Space Antenna.

Future work on the simulations of fallback SN in binaries should be done on including asymmetric explosions, as they are likely in SN explosions. This would redistribute the material and change the amount of high angular momentum fallback. Another improvement would be the inclusion of feedback from the accreting compact objects. This could lower the total amount of accreted material and therefore the final masses and spins of the remnants.

Finally, in chapter 4 we have investigated the characteristics of an electromagnetic counterpart to a BH merger assuming the second BH was formed in a fallback SN.
During a fallback SN, ejecta material settles in mini disks around each BH. We found that the accretion rate depends on the disk material's ability to cool and settle in smaller disks with less pressure support. By fitting the accretion rate, we predict the accretion luminosity at time of merger to be of the order of 10^{35} erg/s for systems formed in symmetric explosions. We also investigate the impact of kicks, and find that favorable kicks can increase the accretion luminosity at time of merger by an order of magnitude. Lastly we compare to the expected accretion rates for binary BHs moving through either the ISM or orbiting in an AGN disk. We find that systems in the ISM are even less bright than systems in with fallback disks, but that systems orbiting in AGN disk have higher

surrounding densities and therefore would result in brighter EM counterparts.

V

Appendices

APPENDIX A

Appendix

A.1 Validation of light curve calculation

In this appendix, we discuss the validation of several numerical choices in the 1D radiation hydrodynamics calculations with SNEC that we use to produce model light curves in chapter 1.

In mapping the 3D hydrodynamics calculation of the merger (Section 1.3) to the 1D explosive calculation, we need to make an assumption about the location (described by radius or mass coordinate) where the explosion energy is deposited. We have argued in Section 1.2 that this deposition location is somewhere within the hydrogen envelope. Here we explore the sensitivity to that choice as follows. Beginning with our fiducial case of a $30M_\odot$ donor star and $3M_\odot$ black hole in a $q = 0.1$ merger, we deposit 10^{51} erg of thermal energy spread over $0.1M_\odot$ at different mass coordinate locations. Our default assumption is $M_{\rm in} = 10.75M_\odot$, which corresponds to the enclosed mass of at $0.1R_*$ of $7.75M_\odot$ plus a $3M_\odot$ black hole. This model in Figure A.1 corresponds to the fiducial simulation presented in Figure 1.4, which is labeled $q = 0.1$. We then vary the mass coordinate at which thermal energy is deposited, moving outward in the star's Hydrogen envelope. Material inside $M_{\rm in}$ acts as a gravitational point mass for

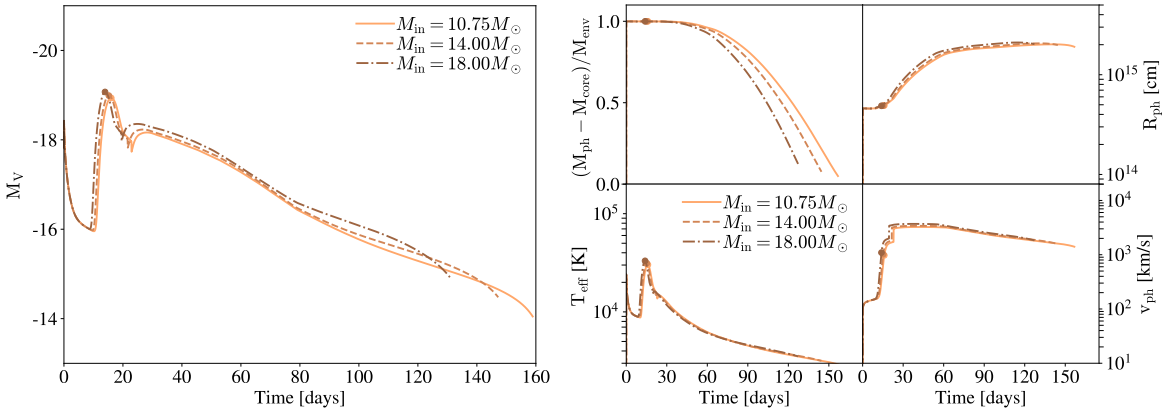

FIGURE A.1 – V-band absolute magnitude (left) and photosphere properties (right) for a $30M_\odot$ donor star involved in a $q = 0.1$ merger, in which we vary the inner mass coordinate of the 10^{51} erg of energy deposition and subsequent ejection within the Hydrogen envelope. Material inside M_{in} does not explode and acts as a gravitational point mass, while material outside M_{in} is expelled. We find that within a factor of two in M_{in}, model light curves are very similar, varying primarily in total plateau duration (which results from differing ejecta masses).

the remainder of the calculation. We find that for $M_{in} = 10.75M_\odot$, $M_{in} = 14M_\odot$, and $M_{in} = 18M_\odot$ (corresponding to radius coordinates of 0.1, 0.16, and 0.24 times the donor star's original radius) the model light curves are very similar indicating only weak dependence on how the energy is spatially deposited within the hydrogen envelope. All of these radii are significantly outside the star's more compact Helium core. We note that for $M_{in} > 20M_\odot$, the case in which > 2/3 of the donor star forms a black hole while only < 1/3 is expelled, we do observe departures in the model light curves, with the bulk of the thermal energy radiated early, and not coupling efficiently to driving envelope expansion.

We also test the dependence of our model results on spatial resolution within the 1D SNEC calculations. Our fiducial case divides the mass into 456 elements. Figure A.2 compares this case to models with twice and four times as many zones (912, 1824, respectively). These tests confirm that our results are converged to within 1% across the light curve duration with any of these resolution choices.

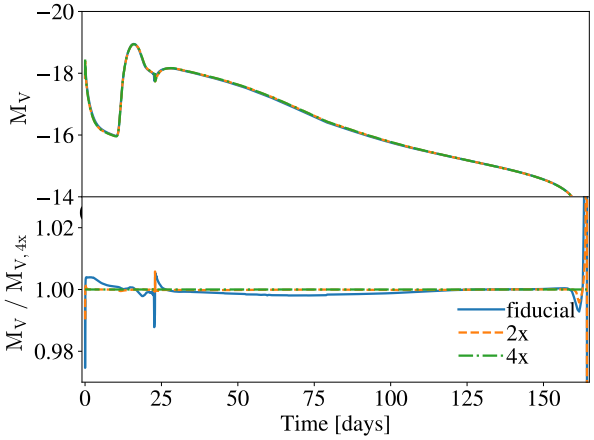

FIGURE A.2 – Absolute V-band magnitude for a $30M_\odot$ donor star involved in a $q = 0.1$ merger. We show models with a fiducial resolution of 456 mass zones, and for mass resolutions of twice and four times as many zones. We find that the light curves are converged to within 1% for the bulk of the model light curves, with the largest variations at shock breakout and near the end of the light curve.

A.2 SUPERNOVA CALCULATIONS IN GADGET 2

In this appendix, we discuss the validation of several numerical choices in the 1D radiation hydrodynamics calculations with SNEC that we use to produce model light curves in chapter 1.

A.3 1D EVOLUTION OF STRIPPED STARS.

We model the evolution of stripped stars using the 1D stellar evolution code MESA (Paxton et al., 2011) version 10398 (Paxton et al., 2013; Paxton et al., 2015; Paxton et al., 2018) as presented in Antoniadis et al., 2022. We follow the evolution from helium zero-age main sequence until the onset of core collapse, which we define as the moment where core infall velocity is larger than 1000 km s^{-1}.

A.3.1 Numerical setup.

The initial models are created by artificially mixing hydrogen-rich models from the pre-main-sequence phase, and until the beginning of helium burning. There is no

mass loss until the beginning of helium burning, but the condition of homogeneity is relaxed at core nitrogen ignition; this guarantees the appropriate CNO element distribution (enhanced N, reduced C and O) for the stripped star. We follow Yoon et al., 2017 to account for mass loss through stellar winds, dependent on the stellar type (WN or WC) and metallicity. We use the `approx21` nuclear network and set resolution variables to `varcontrol_target=1e-5`, and `mesh_delta_coef=0.5`, which results in a finer resolution than MESA's default. Convection was modeled using standard mixing length theory (Böhm-Vitense, 1958) with $\alpha_{MLT} = 2.0$, adopting the Ledoux criterion for instability, employing efficient semiconvection with $\alpha_{SC} = 1.0$ (Schootemeijer et al., 2019), and using predictive mixing in the helium burning regions (Paxton et al., 2018). We use MESA's `mlt++` for the treatment of energy transport in the envelope and neglect radiative acceleration in layers with $T > 10^8$ K during late phases of evolution. This results in compact helium zero-age main sequence radius of $\lesssim 1.2$ $R_\odot$, and a minimum mass threshold of 9.5 $M_\odot$ for the $Z = 0.02$ model. We do not include convective overshooting, which could result in larger core masses for initially less massive stars.

A.3.2 Evolution of two representative models at $Z = 0.02$.

The more massive model is initially 10.0 $M_\odot$ and reaches advanced stages of burning faster and collapses before being able to expand above its initial radius (Figure A.4). A 10.0 $M_\odot$ helium core corresponds, for a single star, to a zero-age main sequence mass of ≈ 32.0 $M_\odot$ (according to the models from Woosley, 2019); however, the models presented here could have accreted matter via mass transfer episodes at some point in their lives. At the end of the evolution, this model has a very compact envelope that decreases sharply in density until reaching the outer layers (Figure A.3). The less massive model is 6.0 $M_\odot$ and is computed to show the contrast with the more massive counterpart. If this less massive model is in a close binary, it is likely to experience a mass transfer episode. This less massive model is more similar to the canonical helium models that explain ultra-stripped stars, the progenitors of ultra-stripped supernovae, Galactic BNSs and GW170817 (LIGO Scientific Collaboration & Virgo Collaboration, 2017c; Tauris et al., 2017; Tauris et al., 2013; Tauris et al., 2015).

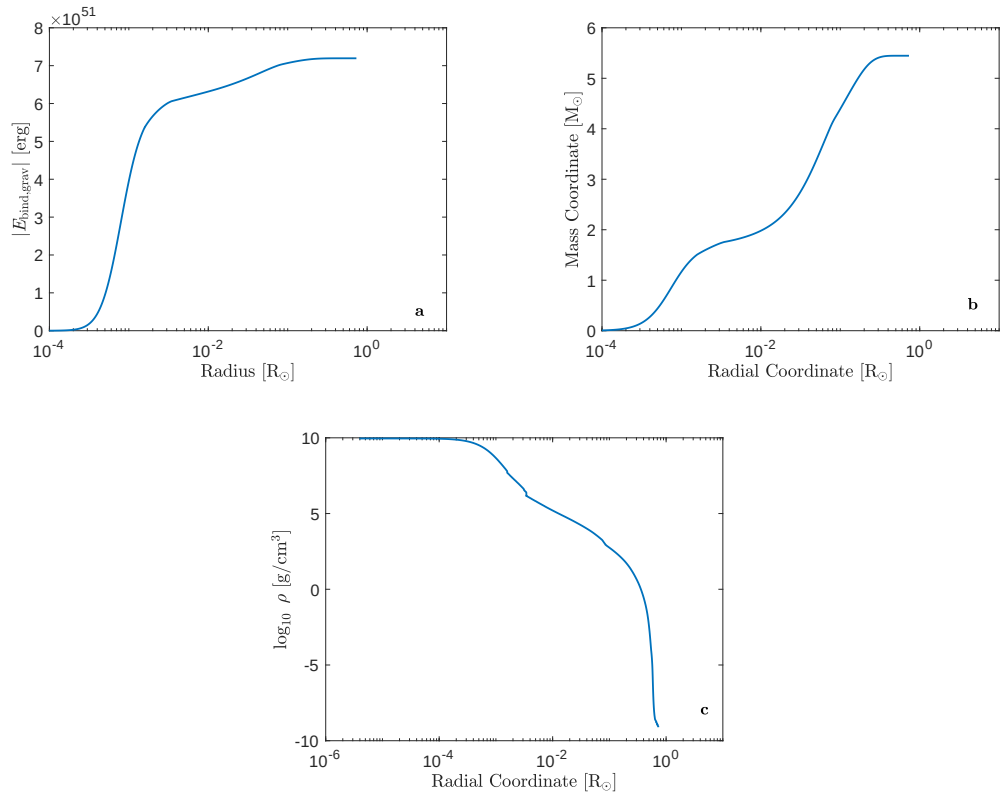

FIGURE A.3 – Stellar structure of exploding model at the onset of core collapse. Gravitational binding energy (**a**), mass coordinate (**b**) and density (**c**) as a function of radial coordinate for the models with helium zero-age main sequence mass of 10.0 $M_\odot$ at metallicity $Z = 0.02$.

A.3.3 Metallicity and mixing study.

There is a dichotomy between stripped stars that do or do not expand which is mass, model and metallicity dependent (Woosley, 2019). To test the mass and metallicity dependence we performed calculations for helium zero-age main sequence masses between $4.0 \leq M/M_\odot \leq 14.0$ in steps of 0.5 $M_\odot$ and at metallicities $Z = \{0.010, 0.015, 0.020, 0.025, 0.030\}$ (Figure A.5). These are a subset of the simulations done in Antoniadis et al., 2022. Stripped stars have helium zero-age main sequence radii of $\lesssim 1.5$ $R_\odot$ and are more compact at lower metallicities. In order to distinguish between stars which significantly expand and those which remain compact, we introduce a dimensionless factor $R_{\rm final}/R_{\rm He-ZAMS}$, where $R_{\rm He-ZAMS}$ is the radius at helium zero-age main sequence and $R_{\rm final}$ is the radius at the moment when the central carbon abundance is $\lesssim 5 \times 10^{-3}$,

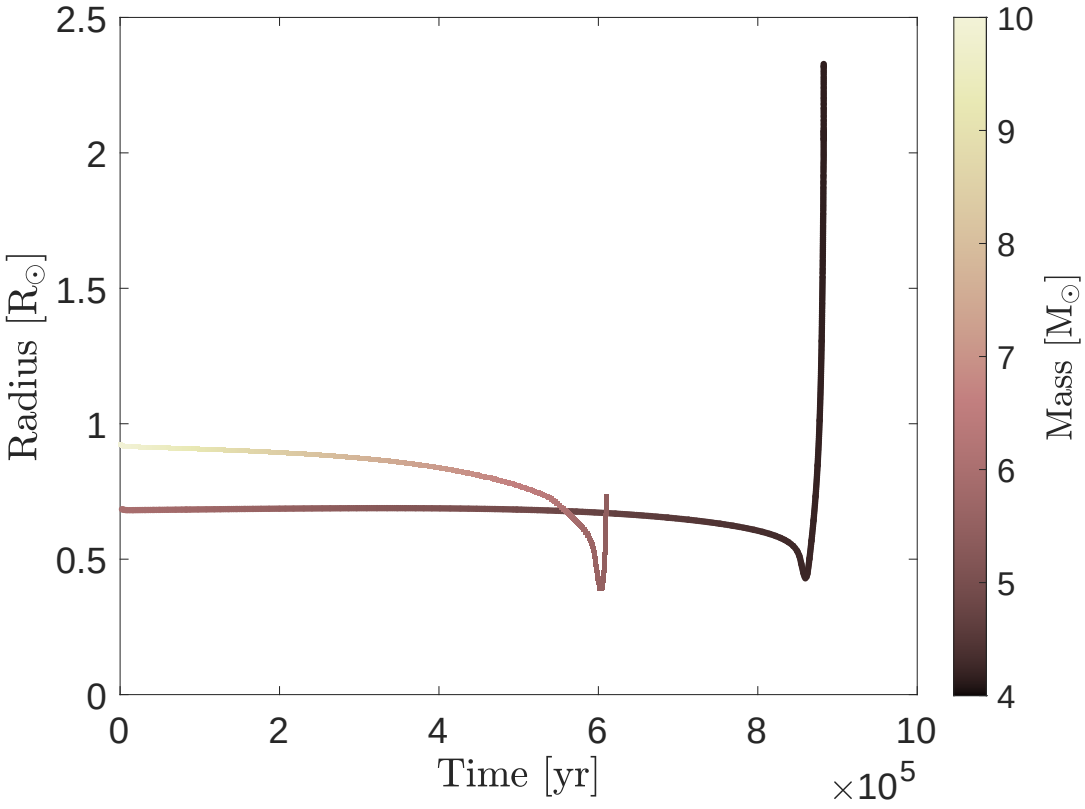

FIGURE A.4 – Time evolution of stripped stars. Radial (y-axis) and mass (colorbar) time evolution (x-axis) of two helium stars, from helium zero-age main sequence to core collapse, at metallicity $Z = 0.02$. The initial helium star masses are 10.0 (initially more expanded) and 6.0 (initially more compact) $M_\odot$, and reach core collapse with masses of 5.4 and 4.2 $M_\odot$, respectively. The initially more expanded star contracts and the initially more compact star expands.

a proxy for central carbon depletion. Stars with $R_{\rm final}/R_{\rm He-ZAMS} \lesssim 1$ remain compact. The minimum mass threshold to remain compact is 9.0 $M_\odot$ at $Z = 0.02$. We test for alternative energy transport envelope treatment by turning off `mlt++` and allowing for radiative acceleration in the envelope. This variation results in helium zero-age main sequence radii of $\lesssim 1.5$ $R_\odot$, and mass threshold of 10.0 $M_\odot$ for the $Z = 0.02$ model. The overall uncertainties on the minimum mass threshold are of order $\lesssim 1.0$ $M_\odot$.

A.4 3D HYDRODYNAMICAL SIMULATION OF FALLBACK SUPERNOVAE.

We study the explosion and fallback accretion of a stripped star with a neutron star companion using the 3D Lagrangian hydrodynamic SPH code GADGET-2 (Springel, 2005). We use a modified version of GADGET-2 that has been previously used to simulate supernovae in binary black hole forming binaries (Batta et al., 2017; Schrøder et al., 2018). Visualization of the hydrodynamical evolution (Figure 3.2) was made using SPLASH (Price, 2007).

A.4.1 Initial conditions and system properties.

Here we describe the initial properties of our fiducial model. The system is initialized as a circular gravitationally bound binary comprised of an exploding star and a neutron star companion at a separation of 1.4 $R_\odot$. The neutron star companion is defined as a sink particle type of mass 1.3 $M_\odot$. In order to build the initial conditions of the exploding star we use a 1D MESA model of a heavy compact progenitor at core collapse (Appendix A.3). This progenitor, with a helium zero-age main sequence mass of 10.0 $M_\odot$ and metallicity of $Z = 0.02$, has mass of 5.4 $M_\odot$ at core collapse. The star's final properties at core collapse are then mapped onto a 3D SPH particle distribution that reproduces the density profile. A million SPH particles are uniformly distributed on spherical shells generated with the HEALPix algorithm. The shells are then spaced according to the local density (Batta et al., 2017). Due to the extremely low densities at the outer layers of the star, mapping with SPH particles became challenging. Therefore, we neglected low density material above 0.5 $R_\odot$ resulting in ≈ 0.1 $M_\odot$ artificially removed from the system (Figure A.3). For the newly born neutron

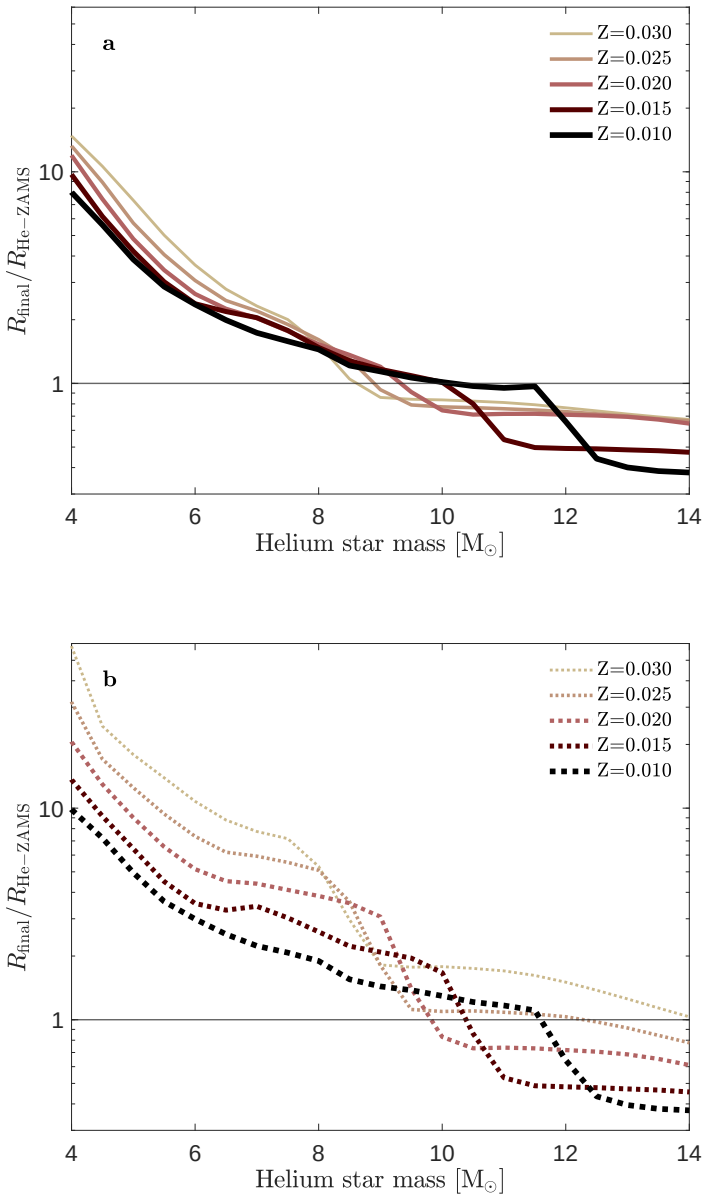

FIGURE A.5 – Summary of radial evolution of stripped helium stars. The behavior of the radial evolution of stripped stars is shown as a function of helium mass (x-axis) and metallicity (color). We parameterize the radii in terms of $R_{\rm He-ZAMS}$ and $R_{\rm final}$ (see Methods). Stars remain compact when $R_{\rm final}/R_{\rm He-ZAMS} < 1$; alternatively, significant expansion occurs when $R_{\rm final}/R_{\rm He-ZAMS} > 1$. The results are shown in solid lines (**a**) for our standard model including `mlt++` and in dashed lines (**b**) for an alternative numerical treatment of mixing (Appendix A.3). The former ultimately leads to stars with less extended envelopes at lower masses.

star, the innermost 1.3 $M_\odot$ of the 3D stellar structure is removed and replaced by a sink particle with the same mass. For our fiducial model (Figure 3.2) a kinetic explosion energy of 1.5 bethes is instantaneously deposited in the shell with mass $dm = 0.7$ $M_\odot$ right above the 1.3 $M_\odot$ that comprises the newly born neutron star. We ran a series of models with different explosion energies (Figure 3.3) spanning from $0.5 \leq E_{\rm exp} \leq 4.0$ bethes resulting in different fallback evolution (Figure A.6).

A.4.2 Resolution study.

We ran simulations for different resolutions to ensure that the remnant mass estimates are accurate for different choices of numerical parameters. For resolutions from $5{\times}10^5$ to $5{\times}10^6$ particles we found remnant mass variations smaller than 0.1 $M_\odot$ and convergence as the number of particles increases (Figure A.7). For our fiducial model we settled for a resolution of 10^6 particles resulting in a mass difference of less than 0.04 $M_\odot$ compared with the highest resolution. The mass of shell in which the kinetic explosion energy is deposited is the main source of physical and numerical uncertainty. For the $E_{51} = 1.5$ model, where $1\,E_{51} = 1$ bethe, thin shell masses of $dm \approx 0.2$ $M_\odot$ lead to remnant masses of ≈ 3 $M_\odot$, more than twice the remnant mass predicted by models which do not incorporate fallback (B. Müller et al., 2016). Thicker shell masses of $dm \approx 0.7$ $M_\odot$ converge to more reasonable remnant masses of ≈ 2.1 $M_\odot$ (Figure A.6). The mapping of 1D stellar models to 3D hydrodynamic ones is known to lead to discretization errors in the hydrostatic equilibrium (Ohlmann et al., 2017). However, the effects of this mapping seem to be negligible in our simulations: while some of the outer layers of the star are artificially ejected because of this, the supernova of a non-exploding model is fully consistent with our lowest explosion energy model, implying complete fallback (see comment about equation on state in Section 3.4). We lastly checked for any effect that a natal kick could have on the remnant mass. Natal kicks of magnitudes of ≈ 10, ≈ 100, and, ≈ 1000 km s^{-1} at random directions, which affect the orbit in timescales longer than the fallback timescale, made little difference with respect to our fiducial model.

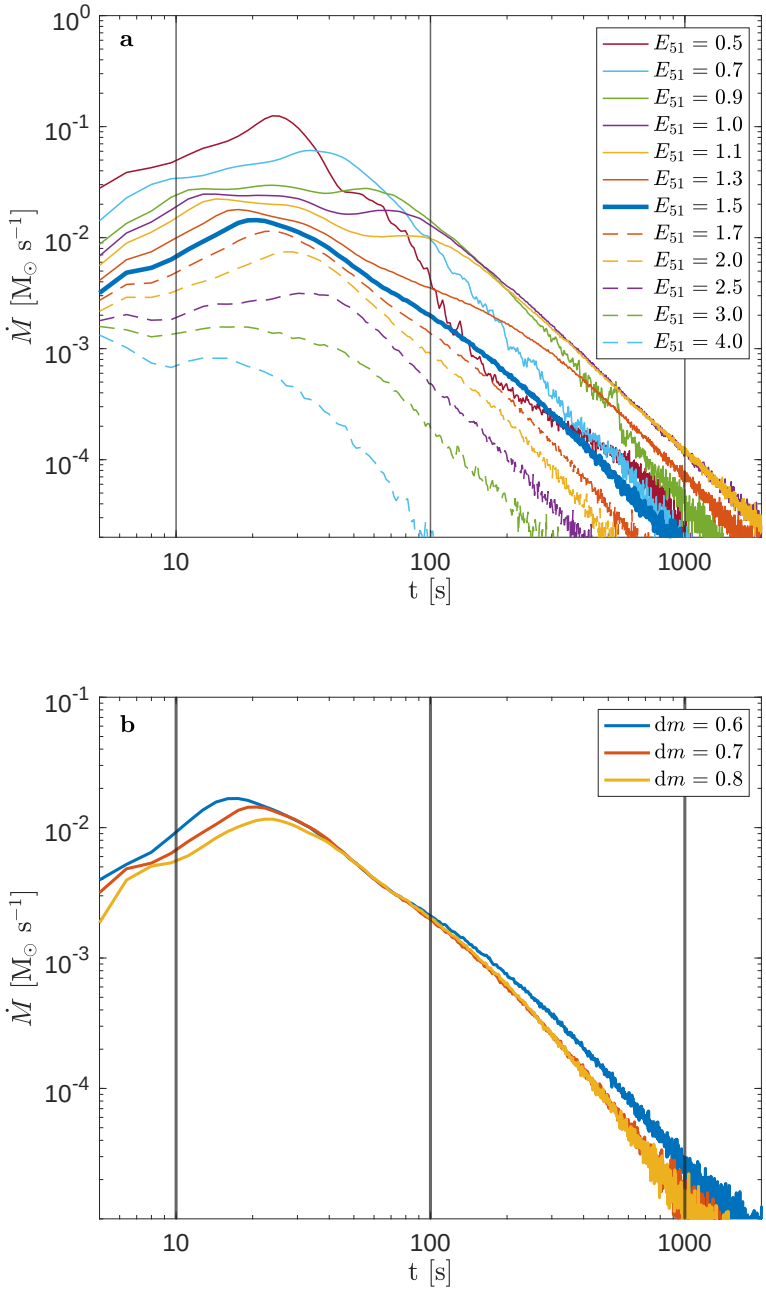

FIGURE A.6 – Fallback mass accretion rate of the exploding star. All models (**a**) and resolution study (**b**) exploring the evolution depending on the size of the mass shell where the kinetic explosion energy is deposited (Appendix A.4).

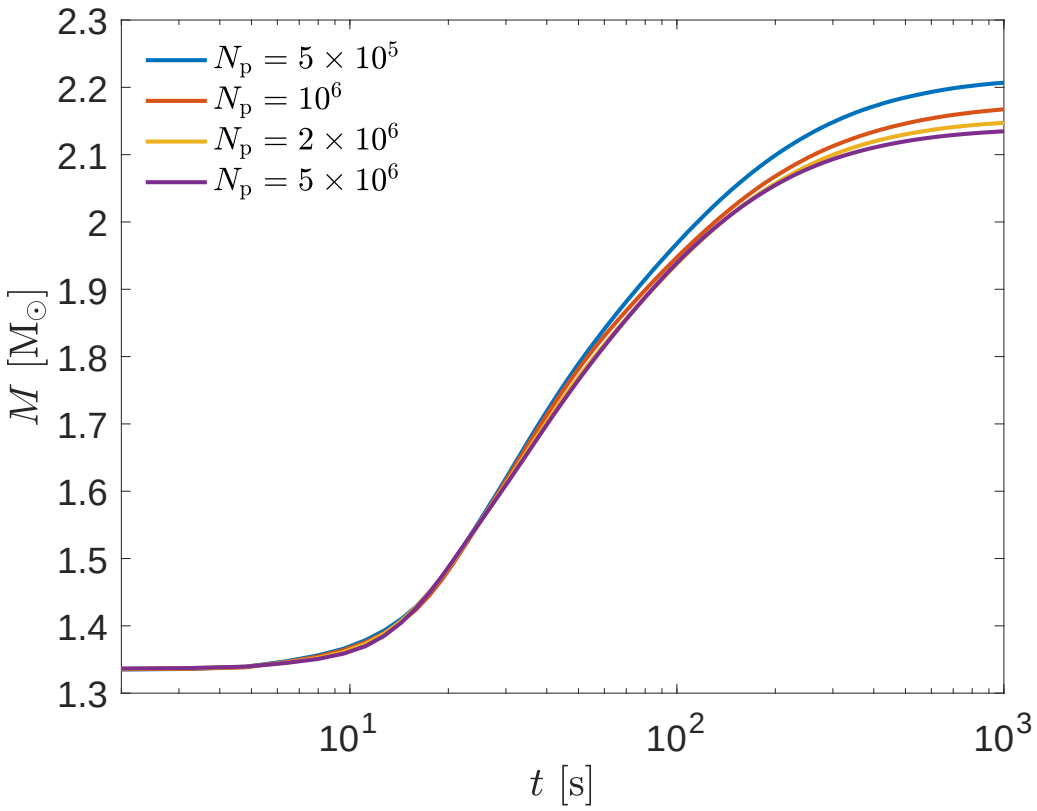

FIGURE A.7 – Post-supernova time evolution, including mass accretion, of the newly born neutron star. Number of particle (N_p) resolution study to determine convergence in our simulations (Appendix A.4).

A.4.3 Open questions in Supernova Explosion Mechanisms

Supernovae are also very complicated processes to model numerically. We do not present a self-consistent explosion model. Instead, we use a simplified approach to study the long-term evolution of supernova fallback in binaries and explore the sensitivity to the currently unknown supernova energy. This allows us to understand the role of fallback in creating light black holes rather than heavy neutron star pairs. These uncertainties in the explosion energy propagate directly into the rates estimates. Moreover, because of the amount of ejected mass, it is more likely to have a binary remain bound the second explosion lead to a black hole instead of a neutron star. Future observations will clarify the most likely outcome of stripped supernovae with

neutron star companions and will allow us to place strict constraints on the explosion mechanism of massive stars.

Here we follow the model from Batta et al., 2017 in order to quantify the accretion history of the newly born neutron star. We define an accretion radius $r_{\rm acc} < 0.01$ $R_\odot$ from the edge of the innermost stable circular orbit (ISCO) of the compact object, in this case the 1.3 $M_\odot$ proto-neutron-star. Particles within the accretion radius and with less specific angular momentum (j) than the one needed to orbit ISCO are considered to be accreted, transferring their entire mass and angular momentum onto the compact object. Particles within the accretion radius and with $j_{\rm ISCO} \leq j < 10 \times j_{\rm ISCO}$ are assumed to be accreted via an accretion disc on a viscous timescale. To this end we neglect any additional feedback from this accretion.

Bibliography

Abbott, B. P., Abbott, R., Abbott, T. D., Abraham, S., Acernese, F., Ackley, K., Adams, C., Adhikari, R. X., Adya, V. B., Affeldt, C., Agathos, M., Agatsuma, K., Aggarwal, N., Aguiar, O. D., Aiello, L., Ain, A., Ajith, P., Allen, G., Allocca, A., ... Zweizig, J. (2020). GW190425: Observation of a Compact Binary Coalescence with Total Mass ~ 3.4 $M_\odot$. *ApJ*, *892*(1), Article L3, L3. https://doi.org/10.3847/2041-8213/ab75f5

Abbott, D. C. (1982). The theory of radiatively driven stellar winds. II. The line acceleration. *ApJ*, *259*, 282–301. https://doi.org/10.1086/160166

Abbott, D. C., Bieging, J. H., Churchwell, E., & Cassinelli, J. P. (1980). VLA radio continuum measurements of mass loss from early-type stars. *ApJ*, *238*, 196–202. https://doi.org/10.1086/157973

Adams, S. M., Kochanek, C. S., Gerke, J. R., & Stanek, K. Z. (2017). The search for failed supernovae with the Large Binocular Telescope: constraints from 7 yr of data. *MNRAS*, *469*(2), 1445–1455. https://doi.org/10.1093/mnras/stx898

Amaro-Seoane, P., Audley, H., Babak, S., Baker, J., Barausse, E., Bender, P., Berti, E., Binetruy, P., Born, M., Bortoluzzi, D., Camp, J., Caprini, C., Cardoso, V., Colpi, M., Conklin, J., Cornish, N., Cutler, C., Danzmann, K., Dolesi, R., ... Zweifel, P. (2017). Laser Interferometer Space Antenna. *arXiv e-prints*, Article arXiv:1702.00786, arXiv:1702.00786.

Andrews, J. J., Farr, W. M., Kalogera, V., & Willems, B. (2015). Evolutionary Channels for the Formation of Double Neutron Stars. *ApJ*, *801*(1), Article 32, 32. https://doi.org/10.1088/0004-637X/801/1/32

Andrews, J. J., & Mandel, I. (2019). Double Neutron Star Populations and Formation Channels. *ApJ*, *880*(1), Article L8, L8. https://doi.org/10.3847/2041-8213/ab2ed1

Andrews, J. E., & Smith, N. (2018). Strong late-time circumstellar interaction in the peculiar supernova iPTF14hls. *MNRAS*, *477*(1), 74–79. https://doi.org/10.1093/mnras/sty584

Antoniadis, J., Aguilera-Dena, D. R., Vigna-Gómez, A., Kramer, M., Langer, N., Müller, B., Tauris, T. M., Wang, C., & Xu, X.-T. (2022). Explodability fluctuations of massive stellar cores enable asymmetric compact object mergers such as GW190814. *A&A*, *657*, Article L6, L6. https://doi.org/10.1051/0004-6361/202142322

Armitage, P. J., & Livio, M. (2000). Black Hole Formation via Hypercritical Accretion during Common-Envelope Evolution. *ApJ*, *532*(1), 540–547. https://doi.org/10.1086/308548

Arzoumanian, Z., Chernoff, D. F., & Cordes, J. M. (2002). The Velocity Distribution of Isolated Radio Pulsars. *ApJ*, *568*(1), 289–301. https://doi.org/10.1086/338805

Ascenzi, S., Oganesyan, G., Branchesi, M., & Ciolfi, R. (2021). Electromagnetic counterparts of compact binary mergers. *Journal of Plasma Physics*, *87*(1), Article 845870102, 845870102. https://doi.org/10.1017/S0022377820001646

Astropy Collaboration, Robitaille, T. P., Tollerud, E. J., Greenfield, P., Droettboom, M., Bray, E., Aldcroft, T., Davis, M., Ginsburg, A., Price-Whelan, A. M., Kerzendorf, W. E., Conley, A., Crighton, N., Barbary, K., Muna, D., Ferguson, H., Grollier, F., Parikh, M. M., Nair, P. H., … Streicher, O. (2013). Astropy: A community Python package for astronomy. *A&A*, *558*, Article A33, A33. https://doi.org/10.1051/0004-6361/201322068

Bardeen, J. M. (1970). Kerr Metric Black Holes. *Nature*, *226*(5240), 64–65. https://doi.org/10.1038/226064a0

Bardeen, J. M., Press, W. H., & Teukolsky, S. A. (1972). Rotating Black Holes: Locally Nonrotating Frames, Energy Extraction, and Scalar Synchrotron Radiation. *ApJ*, *178*, 347–370. https://doi.org/10.1086/151796

Barkov, M. V., & Komissarov, S. S. (2008). Stellar explosions powered by the Blandford-Znajek mechanism. *MNRAS*, *385*(1), L28–L32. https://doi.org/10.1111/j.1745-3933.2008.00427.x

Barkov, M. V., & Komissarov, S. S. (2011). Recycling of neutron stars in common envelopes and hypernova explosions. *MNRAS*, *415*(1), 944–958. https://doi.org/10.1111/j.1365-2966.2011.18762.x

Barrett, J. W., Gaebel, S. M., Neijssel, C. J., Vigna-Gómez, A., Stevenson, S., Berry, C. P. L., Farr, W. M., & Mandel, I. (2018). Accuracy of inference on the physics of binary evolution from gravitational-wave observations. *MNRAS*, *477*(4), 4685–4695. https://doi.org/10.1093/mnras/sty908

Bartel, N., & Bietenholz, M. F. (2008). Shell Revealed in SN 1979C. *ApJ*, *682*(2), 1065–1069. https://doi.org/10.1086/589503

Bartel, N., & Bietenholz, M. F. (2003). SN 1979C VLBI: 22 Years of Almost Free Expansion. *ApJ*, *591*(1), 301–315. https://doi.org/10.1086/375267

Bartos, I., Kocsis, B., Haiman, Z., & Márka, S. (2017). Rapid and Bright Stellar-mass Binary Black Hole Mergers in Active Galactic Nuclei. *ApJ*, *835*(2), Article 165, 165. https://doi.org/10.3847/1538-4357/835/2/165

Bartunov, O. S., & Blinnikov, S. I. (1992). Model of supernova 1979C with radiative transfer in the envelope. *Soviet Astronomy Letters*, *18*, 43.

Batta, A., & Ramirez-Ruiz, E. (2019). Accretion Feedback from newly-formed black holes and its implications for LIGO Sources. *arXiv e-prints*, Article arXiv:1904.04835, arXiv:1904.04835.

Batta, A., Ramirez-Ruiz, E., & Fryer, C. (2017). The Formation of Rapidly Rotating Black Holes in High-mass X-Ray Binaries. *ApJ*, *846*(2), Article L15, L15. https://doi.org/10.3847/2041-8213/aa8506

Belczynski, K., Doctor, Z., Zevin, M., Olejak, A., Banerjee, S., & Chattopadhyay, D. (2022). Black hole - black hole total merger mass and the origin of LIGO/Virgo sources. *arXiv e-prints*, Article arXiv:2204.11730, arXiv:2204.11730.

Belczynski, K., Klencki, J., Fields, C. E., Olejak, A., Berti, E., Meynet, G., Fryer, C. L., Holz, D. E., O'Shaughnessy, R., Brown, D. A., Bulik, T., Leung, S. C., Nomoto, K., Madau, P., Hirschi, R., Kaiser, E., Jones, S., Mondal, S., Chruslinska, M., ... Lasota, J. .-. (2020). Evolutionary roads leading to low effective spins, high black hole masses, and O1/O2 rates for LIGO/Virgo binary black holes. *A&A*, *636*, Article A104, A104. https://doi.org/10.1051/0004-6361/201936528

Belczynski, K., Holz, D. E., Bulik, T., & O'Shaughnessy, R. (2016). The first gravitational-wave source from the isolated evolution of two stars in the 40-100 solar mass range. *Nature*, *534*(7608), 512–515. https://doi.org/10.1038/nature18322

Belczynski, K., Kalogera, V., & Bulik, T. (2002). A Comprehensive Study of Binary Compact Objects as Gravitational Wave Sources: Evolutionary Channels, Rates, and Physical Properties. *ApJ*, *572*(1), 407–431. https://doi.org/10.1086/340304

Belczynski, K., Kalogera, V., Rasio, F. A., Taam, R. E., Zezas, A., Bulik, T., Maccarone, T. J., & Ivanova, N. (2008). Compact Object Modeling with the StarTrack Population Synthesis Code. *ApJS*, *174*(1), 223–260. https://doi.org/10.1086/521026

Belczynski, K., Wiktorowicz, G., Fryer, C. L., Holz, D. E., & Kalogera, V. (2012). Missing Black Holes Unveil the Supernova Explosion Mechanism. *ApJ*, *757*(1), Article 91, 91. https://doi.org/10.1088/0004-637X/757/1/91

Belczyński, K., & Kalogera, V. (2001). A New Formation Channel for Double Neutron Stars Without Recycling: Implications for Gravitational Wave Detection. *ApJ*, *550*(2), L183–L187. https://doi.org/10.1086/319641

Bellm, E., & Kulkarni, S. (2017). The unblinking eye on the sky. *Nature Astronomy*, *1*, Article 0071, 0071. https://doi.org/10.1038/s41550-017-0071

Beniamini, P., & Piran, T. (2016). Formation of double neutron star systems as implied by observations. *MNRAS*, *456*(4), 4089–4099. https://doi.org/10.1093/mnras/stv2903

Berger, E. (2014). Short-Duration Gamma-Ray Bursts. *ARA&A*, *52*, 43–105. https://doi.org/10.1146/annurev-astro-081913-035926

Bhattacharya, D., & van den Heuvel, E. P. J. (1991). Formation and evolution of binary and millisecond radio pulsars. *Phys. Rep.*, *203*(1-2), 1–124. https://doi.org/10.1016/0370-1573(91)90064-S

Bildsten, L., Chakrabarty, D., Chiu, J., Finger, M. H., Koh, D. T., Nelson, R. W., Prince, T. A., Rubin, B. C., Scott, D. M., Stollberg, M., Vaughan, B. A., Wilson, C. A., & Wilson, R. B. (1997). Observations of Accreting Pulsars. *ApJS*, *113*(2), 367–408. https://doi.org/10.1086/313060

Bisnovatyi-Kogan, G. S. (1993). Asymmetric neutrino emission and formation of rapidly moving pulsars. *Astronomical and Astrophysical Transactions*, *3*(4), 287–294. https://doi.org/10.1080/10556799308230566

Blaauw, A. (1961). On the origin of the O- and B-type stars with high velocities (the "run-away" stars), and some related problems. *Bull. Astron. Inst. Netherlands*, *15*, 265.

Blandford, R. D., & Znajek, R. L. (1977). Electromagnetic extraction of energy from Kerr black holes. *MNRAS*, *179*, 433–456. https://doi.org/10.1093/mnras/179.3.433

Blondin, J. M., Kallman, T. R., Fryxell, B. A., & Taam, R. E. (1990). Hydrodynamic Simulations of Stellar Wind Disruption by a Compact X-Ray Source. *ApJ*, *356*, 591. https://doi.org/10.1086/168865

Blondin, J. M., Lundqvist, P., & Chevalier, R. A. (1996). Axisymmetric Circumstellar Interaction in Supernovae. *ApJ*, *472*, 257. https://doi.org/10.1086/178060

Böhm-Vitense, E. (1958). Über die Wasserstoffkonvektionszone in Sternen verschiedener Effektivtemperaturen und Leuchtkräfte. Mit 5 Textabbildungen. *ZAp*, *46*, 108.

Bondi, H. (1952). On spherically symmetrical accretion. *MNRAS*, *112*, 195. https://doi.org/10.1093/mnras/112.2.195

Bondi, H., & Hoyle, F. (1944). On the mechanism of accretion by stars. *MNRAS*, *104*, 273. https://doi.org/10.1093/mnras/104.5.273

Bozzo, E., Oskinova, L., Feldmeier, A., & Falanga, M. (2016). Clumpy wind accretion in supergiant neutron star high mass X-ray binaries. *A&A*, *589*, Article A102, A102. https://doi.org/10.1051/0004-6361/201628341

Brandt, N., & Podsiadlowski, P. (1995). The effects of high-velocity supernova kicks on the orbital properties and sky distributions of neutron-star binaries. *MNRAS*, *274*(2), 461–484. https://doi.org/10.1093/mnras/274.2.461

Broekgaarden, F. S., & Berger, E. (2021). Formation of the First Two Black Hole-Neutron Star Mergers (GW200115 and GW200105) from Isolated Binary Evolution. *ApJ*, *920*(1), Article L13, L13. https://doi.org/10.3847/2041-8213/ac2832

Brookshaw, L., & Tavani, M. (1993). Wind-driven Angular Momentum Loss in Binary Systems. I. Ballistic Case. *ApJ*, *410*, 719. https://doi.org/10.1086/172789

Burrows, A., & Vartanyan, D. (2021). Core-collapse supernova explosion theory. *Nature*, *589*(7840), 29–39. https://doi.org/10.1038/s41586-020-03059-w

Burrows, A., & Hayes, J. (1996). Pulsar Recoil and Gravitational Radiation Due to Asymmetrical Stellar Collapse and Explosion. *Phys. Rev. Lett.*, *76*(3), 352–355. https://doi.org/10.1103/PhysRevLett.76.352

Calderón, D., Cuadra, J., Schartmann, M., Burkert, A., Prieto, J., & Russell, C. M. P. (2020). Three-dimensional simulations of clump formation in stellar wind collisions. *MNRAS*, *493*(1), 447–467. https://doi.org/10.1093/mnras/staa090

Castor, J. I., Abbott, D. C., & Klein, R. I. (1975). Radiation-driven winds in Of stars. *ApJ*, *195*, 157–174. https://doi.org/10.1086/153315

Chan, C., Müller, B., Heger, A., Pakmor, R., & Springel, V. (2018). Black Hole Formation and Fallback during the Supernova Explosion of a 40 $M_\odot$ Star. *ApJ*, *852*(1), Article L19, L19. https://doi.org/10.3847/2041-8213/aaa28c

Chandra, P. (2018). Circumstellar Interaction in Supernovae in Dense Environments—An Observational Perspective. *Space Sci. Rev.*, *214*(1), Article 27, 27. https://doi.org/10.1007/s11214-017-0461-6

Chen, W.-X., & Beloborodov, A. M. (2007). Neutrino-cooled Accretion Disks around Spinning Black Holes. *ApJ*, *657*(1), 383–399. https://doi.org/10.1086/508923

Chen, Z., Blackman, E. G., Nordhaus, J., Frank, A., & Carroll-Nellenback, J. (2018). Wind-accelerated orbital evolution in binary systems with giant stars. *MNRAS*, *473*(1), 747–756. https://doi.org/10.1093/mnras/stx2335

Chevalier, R. A. (1993). Neutron Star Accretion in a Stellar Envelope. *ApJ*, *411*, L33. https://doi.org/10.1086/186905

Chevalier, R. A. (1996). Neutrino-cooled Accretion: Rotation and Stellar Equation of State. *ApJ*, *459*, 322. https://doi.org/10.1086/176895

Chevalier, R. A. (2012). Common Envelope Evolution Leading to Supernovae with Dense Interaction. *ApJ*, *752*(1), Article L2, L2. https://doi.org/10.1088/2041-8205/752/1/L2

Chevalier, R. A., & Irwin, C. M. (2011). Shock Breakout in Dense Mass Loss: Luminous Supernovae. *ApJ*, *729*(1), Article L6, L6. https://doi.org/10.1088/2041-8205/729/1/L6

Chevalier, R. A., & Irwin, C. M. (2012). X-Rays from Supernova Shocks in Dense Mass Loss. *ApJ*, *747*(1), Article L17, L17. https://doi.org/10.1088/2041-8205/747/1/L17

Choi, J., Dotter, A., Conroy, C., Cantiello, M., Paxton, B., & Johnson, B. D. (2016). Mesa Isochrones and Stellar Tracks (MIST). I. Solar-scaled Models. *ApJ*, *823*(2), Article 102, 102. https://doi.org/10.3847/0004-637X/823/2/102

Chugai, N. N. (1997). The origin of supernovae with dense winds. *Astronomy Reports*, *41*(5), 672–681.

Chugai, N. N. (2001). Broad emission lines from the opaque electron-scattering environment of SN 1998S. *MNRAS*, *326*(4), 1448–1454. https://doi.org/10.1111/j.1365-2966.2001.04717.x

Chugai, N. N., & Danziger, I. J. (1994). SN 1988Z: low-mass ejecta colliding with the clumpy wind? *MNRAS*, *268*, 173–180. https://doi.org/10.1093/mnras/268.1.173

Chugai, N. N., Blinnikov, S. I., Cumming, R. J., Lundqvist, P., Bragaglia, A., Filippenko, A. V., Leonard, D. C., Matheson, T., & Sollerman, J. (2004). The Type IIn supernova 1994W: evidence for the explosive ejection of a circumstellar envelope. *MNRAS*, *352*(4), 1213–1231. https://doi.org/10.1111/j.1365-2966.2004.08011.x

Clayton, M., Podsiadlowski, P., Ivanova, N., & Justham, S. (2017). Episodic mass ejections from common-envelope objects. *MNRAS*, *470*(2), 1788–1808. https://doi.org/10.1093/mnras/stx1290

Connaughton, V., Burns, E., Goldstein, A., Blackburn, L., Briggs, M. S., Christensen, N., Hui, C. M., Kocevski, D., Littenberg, T., McEnery, J. E., Racusin, J., Shawhan, P., Veitch, J., Wilson-Hodge, C. A., Bhat, P. N., Bissaldi, E., Cleveland, W., Giles, M. M., Gibby, M. H., … Veres, P. (2018). On the Interpretation of the Fermi-GBM Transient Observed in Coincidence with LIGO Gravitational-wave Event GW150914. *ApJ*, *853*(1), Article L9, L9. https://doi.org/10.3847/2041-8213/aaa4f2

Connaughton, V., Burns, E., Goldstein, A., Blackburn, L., Briggs, M. S., Zhang, B. .-., Camp, J., Christensen, N., Hui, C. M., Jenke, P., Littenberg, T., McEnery, J. E., Racusin, J., Shawhan, P., Singer, L., Veitch, J., Wilson-Hodge, C. A., Bhat, P. N., Bissaldi, E., … Veres, P. (2016). Fermi GBM Observations of LIGO Gravitational-wave Event GW150914. *ApJ*, *826*(1), Article L6, L6. https://doi.org/10.3847/2041-8205/826/1/L6

Conroy, C., & Kratter, K. M. (2012). Runaway Stars and the Escape of Ionizing Radiation from High-redshift Galaxies. *ApJ*, *755*(2), Article 123, 123. https://doi.org/10.1088/0004-637X/755/2/123

Coulter, D. A., Foley, R. J., Kilpatrick, C. D., Drout, M. R., Piro, A. L., Shappee, B. J., Siebert, M. R., Simon, J. D., Ulloa, N., Kasen, D., Madore, B. F., Murguia-Berthier, A., Pan, Y. .-., Prochaska, J. X., Ramirez-Ruiz, E., Rest, A., & Rojas-Bravo, C. (2017). Swope Supernova Survey 2017a (SSS17a), the optical counterpart to a gravitational wave source. *Science*, *358*(6370), 1556–1558. https://doi.org/10.1126/science.aap9811

Das, S., & Ray, A. (2017). Modeling Type II-P/II-L Supernovae Interacting with Recent Episodic Mass Ejections from Their Presupernova Stars with MESA and SNEC. *ApJ*, *851*(2), Article 138, 138. https://doi.org/10.3847/1538-4357/aa97e1

Davidson, K., & Ostriker, J. P. (1973). Neutron-Star Accretion in a Stellar Wind: Model for a Pulsed X-Ray Source. *ApJ*, *179*, 585–598. https://doi.org/10.1086/151897

De, S., MacLeod, M., Everson, R. W., Antoni, A., Mandel, I., & Ramirez-Ruiz, E. (2020). Common Envelope Wind Tunnel: The Effects of Binary Mass Ratio and Implications for the Accretion-driven Growth of LIGO Binary Black Holes. *ApJ*, *897*(2), Article 130, 130. https://doi.org/10.3847/1538-4357/ab9ac6

de Kool, M. (1990). Common Envelope Evolution and Double Cores of Planetary Nebulae. *ApJ*, *358*, 189. https://doi.org/10.1086/168974

De Marco, O., & Izzard, R. G. (2017). Dawes Review 6: The Impact of Companions on Stellar Evolution. *PASA*, *34*, Article e001, e001. https://doi.org/10.1017/pasa.2016.52

de Mink, S. E., & King, A. (2017). Electromagnetic Signals Following Stellar-mass Black Hole Mergers. *ApJ*, *839*(1), Article L7, L7. https://doi.org/10.3847/2041-8213/aa67f3

de Mink, S. E., & Mandel, I. (2016). The chemically homogeneous evolutionary channel for binary black hole mergers: rates and properties of gravitational-wave events detectable by advanced LIGO. *MNRAS*, *460*(4), 3545–3553. https://doi.org/10.1093/mnras/stw1219

de Mink, S. E., Sana, H., Langer, N., Izzard, R. G., & Schneider, F. R. N. (2014). The Incidence of Stellar Mergers and Mass Gainers among Massive Stars. *ApJ*, *782*(1), Article 7, 7. https://doi.org/10.1088/0004-637X/782/1/7

Dessart, L., Audit, E., & Hillier, D. J. (2015). Numerical simulations of superluminous supernovae of type IIn. *MNRAS*, *449*(4), 4304–4325. https://doi.org/10.1093/mnras/stv609

Dexter, J., & Kasen, D. (2013). Supernova Light Curves Powered by Fallback Accretion. *ApJ*, *772*(1), Article 30, 30. https://doi.org/10.1088/0004-637X/772/1/30

Dong, D. Z., Hallinan, G., Nakar, E., Ho, A. Y. Q., Hughes, A. K., Hotokezaka, K., Myers, S. T., De, K., Mooley, K. P., Ravi, V., Horesh, A., Kasliwal, M. M., & Kulkarni, S. R. (2021). A transient radio source consistent with a merger-triggered core collapse supernova. *Science*, *373*(6559), 1125–1129. https://doi.org/10.1126/science.abg6037

Dotter, A. (2016). MESA Isochrones and Stellar Tracks (MIST) 0: Methods for the Construction of Stellar Isochrones. *ApJS*, *222*(1), Article 8, 8. https://doi.org/10.3847/0067-0049/222/1/8

Dray, L. M., & Tout, C. A. (2003). Chemical enrichment by Wolf-Rayet stars: non-solar metallicities. *MNRAS*, *341*(1), 299–325. https://doi.org/10.1046/j.1365-8711.2003.06420.x

Duchêne, G., & Kraus, A. (2013). Stellar Multiplicity. *ARA&A*, *51*(1), 269–310. https://doi.org/10.1146/annurev-astro-081710-102602

Edgar, R. (2004). A review of Bondi-Hoyle-Lyttleton accretion. *New A Rev.*, *48*(10), 843–859. https://doi.org/10.1016/j.newar.2004.06.001

Eggleton, P. P. (1983). Aproximations to the radii of Roche lobes. *ApJ*, *268*, 368–369. https://doi.org/10.1086/160960

El Mellah, I., Bolte, J., Decin, L., Homan, W., & Keppens, R. (2020). Wind morphology around cool evolved stars in binaries. The case of slowly accelerating oxygen-rich outflows. *A&A*, *637*, Article A91, A91. https://doi.org/10.1051/0004-6361/202037492

El Mellah, I., Grinberg, V., Sundqvist, J. O., Driessen, F. A., & Leutenegger, M. A. (2020). Radiography in high mass X-ray binaries. Micro-structure of the stellar wind through variability of the column density. *A&A*, *643*, Article A9, A9. https://doi.org/10.1051/0004-6361/202038791

El Mellah, I., Sander, A. A. C., Sundqvist, J. O., & Keppens, R. (2019). Formation of wind-captured disks in supergiant X-ray binaries. Consequences for Vela X-1 and Cygnus X-1. *A&A*, *622*, Article A189, A189. https://doi.org/10.1051/0004-6361/201834498

El Mellah, I., Sundqvist, J. O., & Keppens, R. (2018). Accretion from a clumpy massive-star wind in supergiant X-ray binaries. *MNRAS*, *475*(3), 3240–3252. https://doi.org/10.1093/mnras/stx3211

Eldridge, J. J., Guo, N. .-., Rodrigues, N., Stanway, E. R., & Xiao, L. (2019). Supernova lightCURVE POPulation Synthesis II: Validation against supernovae with an observed progenitor. *PASA*, *36*, Article e041, e041. https://doi.org/10.1017/pasa.2019.31

Eldridge, J. J., Stanway, E. R., Xiao, L., McClelland, L. A. S., Taylor, G., Ng, M., Greis, S. M. L., & Bray, J. C. (2017). Binary Population and Spectral Synthesis Version 2.1: Construction, Observational Verification, and New Results. *PASA*, *34*, Article e058, e058. https://doi.org/10.1017/pasa.2017.51

Eldridge, J. J., Xiao, L., Stanway, E. R., Rodrigues, N., & Guo, N. .-. (2018). Supernova lightCURVE POPulation Synthesis I: Including interacting binaries is key to understanding the diversity of type II supernova lightcurves. *PASA*, *35*, Article e049, e049. https://doi.org/10.1017/pasa.2018.47

Eldridge, J. J., Fraser, M., Smartt, S. J., Maund, J. R., & Crockett, R. M. (2013). The death of massive stars - II. Observational constraints on the progenitors of Type Ibc supernovae. *MNRAS*, *436*(1), 774–795. https://doi.org/10.1093/mnras/stt1612

Ensman, L., & Burrows, A. (1992). Shock Breakout in SN 1987A. *ApJ*, *393*, 742. https://doi.org/10.1086/171542

Ertl, T., Janka, H. .-., Woosley, S. E., Sukhbold, T., & Ugliano, M. (2016). A Two-parameter Criterion for Classifying the Explodability of Massive Stars by the Neutrino-driven Mechanism. *ApJ*, *818*(2), Article 124, 124. https://doi.org/10.3847/0004-637X/818/2/124

Ertl, T., Woosley, S. E., Sukhbold, T., & Janka, H. .-. (2020). The Explosion of Helium Stars Evolved with Mass Loss. *ApJ*, *890*(1), Article 51, 51. https://doi.org/10.3847/1538-4357/ab6458

Everson, R. W., MacLeod, M., De, S., Macias, P., & Ramirez-Ruiz, E. (2020). Common Envelope Wind Tunnel: Range of Applicability and Self-similarity in Realistic Stellar Envelopes. *ApJ*, *899*(1), Article 77, 77. https://doi.org/10.3847/1538-4357/aba75c

Falanga, M., Bozzo, E., Lutovinov, A., Bonnet-Bidaud, J. M., Fetisova, Y., & Puls, J. (2015). Ephemeris, orbital decay, and masses of ten eclipsing high-mass X-ray binaries. *A&A*, *577*, Article A130, A130. https://doi.org/10.1051/0004-6361/201425191

Farr, W. M., Stevenson, S., Miller, M. C., Mandel, I., Farr, B., & Vecchio, A. (2017). Distinguishing spin-aligned and isotropic black hole populations with gravitational waves. *Nature*, *548*(7667), 426–429. https://doi.org/10.1038/nature23453

Farrow, N., Zhu, X.-J., & Thrane, E. (2019). The Mass Distribution of Galactic Double Neutron Stars. *ApJ*, *876*(1), Article 18, 18. https://doi.org/10.3847/1538-4357/ab12e3

Fassia, A., Meikle, W. P. S., Chugai, N., Geballe, T. R., Lundqvist, P., Walton, N. A., Pollacco, D., Veilleux, S., Wright, G. S., Pettini, M., Kerr, T., Puchnarewicz, E., Puxley, P., Irwin, M., Packham, C., Smartt, S. J., & Harmer, D. (2001). Optical and infrared spectroscopy of the type IIn SN 1998S: days 3-127. *MNRAS*, *325*(3), 907–930. https://doi.org/10.1046/j.1365-8711.2001.04282.x

Feng, E.-H., Shen, R.-F., & Lin, W.-P. (2018). Mechanical Feedback from Black Hole Accretion as an Energy Source of Core-collapse Supernova Explosions. *ApJ*, *867*(2), Article 130, 130. https://doi.org/10.3847/1538-4357/aae385

Fernández, R., Quataert, E., Kashiyama, K., & Coughlin, E. R. (2018). Mass ejection in failed supernovae: variation with stellar progenitor. *MNRAS*, *476*(2), 2366–2383. https://doi.org/10.1093/mnras/sty306

Förster, F., Moriya, T. J., Maureira, J. C., Anderson, J. P., Blinnikov, S., Bufano, F., Cabrera-Vives, G., Clocchiatti, A., de Jaeger, T., Estévez, P. A., Galbany, L., González-Gaitán, S., Gräfener, G., Hamuy, M., Hsiao, E. Y., Huentelemu, P., Huijse, P., Kuncarayakti, H., Martı**********nez, J., ... Young, D. R. (2018). The delay of shock breakout due to circumstellar material evident in most type II supernovae. *Nature Astronomy*, *2*, 808. https://doi.org/10.1038/s41550-018-0563-4

Foucart, F. (2020). A brief overview of black hole-neutron star mergers. *Frontiers in Astronomy and Space Sciences*, *7*, Article 46, 46. https://doi.org/10.3389/fspas.2020.00046

Foucart, F. (2021). Black Hole-Neutron Star Mergers. *Handbook of gravitational wave astronomy* (p. 2). https://doi.org/10.1007/978-981-15-4702-7_14-1

Fragos, T., Andrews, J. J., Ramirez-Ruiz, E., Meynet, G., Kalogera, V., Taam, R. E., & Zezas, A. (2019). The Complete Evolution of a Neutron-star Binary through a Common Envelope Phase Using 1D Hydrodynamic Simulations. *ApJ*, *883*(2), Article L45, L45. https://doi.org/10.3847/2041-8213/ab40d1

Frank, J., King, A., & Raine, D. J. (2002). *Accretion Power in Astrophysics: Third Edition*.

Fraschetti, F. (2018). Possible role of magnetic reconnection in the electromagnetic counterpart of binary black hole merger. *J. Cosmology Astropart. Phys.*, *2018*(4), Article 054, 054. https://doi.org/10.1088/1475-7516/2018/04/054

Friend, D. B., & Abbott, D. C. (1986). The Theory of Radiatively Driven Stellar Winds. III. Wind Models with Finite Disk Correction and Rotation. *ApJ*, *311*, 701. https://doi.org/10.1086/164809

Fryer, C. L., & Woosley, S. E. (1998). Helium Star/Black Hole Mergers: A New Gamma-Ray Burst Model. *ApJ*, *502*(1), L9–L12. https://doi.org/10.1086/311493

Fryer, C. L., Belczynski, K., Wiktorowicz, G., Dominik, M., Kalogera, V., & Holz, D. E. (2012). Compact Remnant Mass Function: Dependence on the Explosion Mechanism and Metallicity. *ApJ*, *749*(1), Article 91, 91. https://doi.org/10.1088/0004-637X/749/1/91

Fryer, C. L., Benz, W., & Herant, M. (1996). The Dynamics and Outcomes of Rapid Infall onto Neutron Stars. *ApJ*, *460*, 801. https://doi.org/10.1086/177011

Fryer, C. L., Rueda, J. A., & Ruffini, R. (2014). Hypercritical Accretion, Induced Gravitational Collapse, and Binary-Driven Hypernovae. *ApJ*, *793*(2), Article L36, L36. https://doi.org/10.1088/2041-8205/793/2/L36

Fryer, C. L., Woosley, S. E., & Hartmann, D. H. (1999). Formation Rates of Black Hole Accretion Disk Gamma-Ray Bursts. *ApJ*, *526*(1), 152–177. https://doi.org/10.1086/307992

Fryer, C. L., Herwig, F., Hungerford, A., & Timmes, F. X. (2006). Supernova Fallback: A Possible Site for the r-Process. *ApJ*, *646*(2), L131–L134. https://doi.org/10.1086/507071

Fuller, J. (2017). Pre-supernova outbursts via wave heating in massive stars - I. Red supergiants. *MNRAS*, *470*(2), 1642–1656. https://doi.org/10.1093/mnras/stx1314

Fürst, F., Kreykenbohm, I., Pottschmidt, K., Wilms, J., Hanke, M., Rothschild, R. E., Kretschmar, P., Schulz, N. S., Huenemoerder, D. P., Klochkov, D., & Staubert, R. (2010). X-ray variation statistics and wind clumping in Vela X-1. *A&A*, *519*, Article A37, A37. https://doi.org/10.1051/0004-6361/200913981

Galaudage, S., Adamcewicz, C., Zhu, X.-J., Stevenson, S., & Thrane, E. (2021). Heavy Double Neutron Stars: Birth, Midlife, and Death. *ApJ*, *909*(2), Article L19, L19. https://doi.org/10.3847/2041-8213/abe7f6

Gerosa, D., & Berti, E. (2017). Are merging black holes born from stellar collapse or previous mergers? *Phys. Rev. D*, *95*(12), Article 124046, 124046. https://doi.org/10.1103/PhysRevD.95.124046

Gies, D. R., Bolton, C. T., Thomson, J. R., Huang, W., McSwain, M. V., Riddle, R. L., Wang, Z., Wiita, P. J., Wingert, D. W., Csák, B., & Kiss, L. L. (2003). Wind Accretion and State Transitions in Cygnus X-1. *ApJ*, *583*(1), 424–436. https://doi.org/10.1086/345345

Gilkis, A., Soker, N., & Kashi, A. (2019). Common envelope jets supernova (CEJSN) impostors resulting from a neutron star companion. *MNRAS*, *482*(3), 4233–4242. https://doi.org/10.1093/mnras/sty3008

Ginzburg, S., & Balberg, S. (2012). Superluminous Light Curves from Supernovae Exploding in a Dense Wind. *ApJ*, *757*(2), Article 178, 178. https://doi.org/10.1088/0004-637X/757/2/178

Ginzburg, S., & Balberg, S. (2014). Light Curves from Supernova Shock Breakout through an Extended Wind. *ApJ*, *780*(1), Article 18, 18. https://doi.org/10.1088/0004-637X/780/1/18

Górski, K. M., Hivon, E., Banday, A. J., Wandelt, B. D., Hansen, F. K., Reinecke, M., & Bartelmann, M. (2005). HEALPix: A Framework for High-Resolution Discretization and Fast Analysis of Data Distributed on the Sphere. *ApJ*, *622*(2), 759–771. https://doi.org/10.1086/427976

Götberg, Y., de Mink, S. E., & Groh, J. H. (2017). Ionizing spectra of stars that lose their envelope through interaction with a binary companion: role of metallicity. *A&A*, *608*, Article A11, A11. https://doi.org/10.1051/0004-6361/201730472

Götberg, Y., de Mink, S. E., Groh, J. H., Leitherer, C., & Norman, C. (2019). The impact of stars stripped in binaries on the integrated spectra of stellar populations. *A&A*, *629*, Article A134, A134. https://doi.org/10.1051/0004-6361/201834525

Götberg, Y., de Mink, S. E., McQuinn, M., Zapartas, E., Groh, J. H., & Norman, C. (2020). Contribution from stars stripped in binaries to cosmic reionization of hydrogen and helium. *A&A*, *634*, Article A134, A134. https://doi.org/10.1051/0004-6361/201936669

Graham, M. J., Ford, K. E. S., McKernan, B., Ross, N. P., Stern, D., Burdge, K., Coughlin, M., Djorgovski, S. G., Drake, A. J., Duev, D., Kasliwal, M., Mahabal, A. A., van Velzen, S., Belecki, J., Bellm, E. C., Burruss, R., Cenko, S. B., Cunningham, V., Helou, G., ... Soumagnac, M. T. (2020). Candidate Electromagnetic Counterpart to the Binary Black Hole Merger Gravitational-Wave Event S190521g*. *Phys. Rev. Lett.*, *124*(25), Article 251102, 251102. https://doi.org/10.1103/PhysRevLett.124.251102

Grichener, A., Sabach, E., & Soker, N. (2018). The limited role of recombination energy in common envelope removal. *MNRAS*, *478*(2), 1818–1824. https://doi.org/10.1093/mnras/sty1178

Grichener, A., & Soker, N. (2019). The Common Envelope Jet Supernova (CEJSN) r-process Scenario. *ApJ*, *878*(1), Article 24, 24. https://doi.org/10.3847/1538-4357/ab1d5d

Guillochon, J., Parrent, J., Kelley, L. Z., & Margutti, R. (2017). An Open Catalog for Supernova Data. *ApJ*, *835*(1), Article 64, 64. https://doi.org/10.3847/1538-4357/835/1/64

Gunn, J. E., & Ostriker, J. P. (1970). On the Nature of Pulsars. III. Analysis of Observations. *ApJ*, *160*, 979. https://doi.org/10.1086/150487

Hadrava, P., & Čechura, J. (2012). Really focused stellar winds in X-ray binaries. *A&A*, *542*, Article A42, A42. https://doi.org/10.1051/0004-6361/201016046

Hallinan, G., Corsi, A., Mooley, K. P., Hotokezaka, K., Nakar, E., Kasliwal, M. M., Kaplan, D. L., Frail, D. A., Myers, S. T., Murphy, T., De, K., Dobie, D., Allison, J. R., Bannister, K. W., Bhalerao, V., Chandra, P., Clarke, T. E., Giacintucci, S., Ho, A. Y. Q., ... Singer, L. P. (2017). A radio counterpart to a neutron star merger. *Science*, *358*(6370), 1579–1583. https://doi.org/10.1126/science.aap9855

Hansen, B. M. S., & Phinney, E. S. (1997). The pulsar kick velocity distribution. *MNRAS*, *291*(3), 569–577. https://doi.org/10.1093/mnras/291.3.569

Hernquist, L., & Katz, N. (1989). TREESPH: A Unification of SPH with the Hierarchical Tree Method. *ApJS*, *70*, 419. https://doi.org/10.1086/191344

Hillel, S., Schreier, R., & Soker, N. (2022). Three-dimensional simulations of the jet feedback mechanism in common envelope jets supernovae. *MNRAS*, *514*(3), 3212–3221. https://doi.org/10.1093/mnras/stac1341

Holgado, A. M., Ricker, P. M., & Huerta, E. A. (2018). Gravitational Waves from Accreting Neutron Stars Undergoing Common-envelope Inspiral. *ApJ*, *857*(1), Article 38, 38. https://doi.org/10.3847/1538-4357/aab6a9

Holoien, T. W. .-., Brown, J. S., Vallely, P. J., Stanek, K. Z., Kochanek, C. S., Shappee, B. J., Prieto, J. L., Dong, S., Brimacombe, J., Bishop, D. W., Bose, S., Beacom, J. F., Bersier, D., Chen, P., Chomiuk, L., Falco, E., Holmbo, S., Jayasinghe, T., Morrell, N., ... Wiethoff, W. S. (2019). The ASAS-SN bright supernova catalogue - IV. 2017. *MNRAS*, *484*(2), 1899–1911. https://doi.org/10.1093/mnras/stz073

Hotokezaka, K., & Piran, T. (2017). Implications of the Low Binary Black Hole Aligned Spins Observed by LIGO. *ApJ*, *842*(2), Article 111, 111. https://doi.org/10.3847/1538-4357/aa6f61

Houck, J. C., & Chevalier, R. A. (1991). Steady Spherical Hypercritical Accretion onto Neutron Stars. *ApJ*, *376*, 234. https://doi.org/10.1086/170272

Hoyle, F., & Lyttleton, R. A. (1939). The effect of interstellar matter on climatic variation. *Proceedings of the Cambridge Philosophical Society*, *35*(3), 405. https://doi.org/10.1017/S0305004100021150

Huang, S.-S. (1963). Modes of Mass Ejection by Binary Stars and the Effect on Their Orbital Periods. *ApJ*, *138*, 471. https://doi.org/10.1086/147659

Huarte-Espinosa, M., Carroll-Nellenback, J., Nordhaus, J., Frank, A., & Blackman, E. G. (2013). The formation and evolution of wind-capture discs in binary systems. *MNRAS*, *433*(1), 295–306. https://doi.org/10.1093/mnras/stt725

Hulse, R. A., & Taylor, J. H. (1975). Discovery of a pulsar in a binary system. *ApJ*, *195*, L51–L53. https://doi.org/10.1086/181708

Hurley, J. R., Tout, C. A., & Pols, O. R. (2002). Evolution of binary stars and the effect of tides on binary populations. *MNRAS*, *329*(4), 897–928. https://doi.org/10.1046/j.1365-8711.2002.05038.x

Iben, J., Icko, & Livio, M. (1993). Common Envelopes in Binary Star Evolution. *PASP*, *105*, 1373. https://doi.org/10.1086/133321

Ivanova, N., Justham, S., Avendano Nandez, J. L., & Lombardi, J. C. (2013). Identification of the Long-Sought Common-Envelope Events. *Science*, *339*(6118), 433. https://doi.org/10.1126/science.1225540

Ivanova, N., Justham, S., Chen, X., De Marco, O., Fryer, C. L., Gaburov, E., Ge, H., Glebbeek, E., Han, Z., Li, X. .-., Lu, G., Marsh, T., Podsiadlowski, P., Potter, A., Soker, N., Taam, R., Tauris, T. M., van den Heuvel, E. P. J., & Webbink, R. F. (2013). Common envelope evolution: where we stand and how we can move forward. *A&A Rev.*, *21*, Article 59, 59. https://doi.org/10.1007/s00159-013-0059-2

Izzard, R. G., Dray, L. M., Karakas, A. I., Lugaro, M., & Tout, C. A. (2006). Population nucleosynthesis in single and binary stars. I. Model. *A&A*, *460*(2), 565–572. https://doi.org/10.1051/0004-6361:20066129

Izzard, R. G., Ramirez-Ruiz, E., & Tout, C. A. (2004). Formation rates of core-collapse supernovae and gamma-ray bursts. *MNRAS*, *348*(4), 1215–1228. https://doi.org/10.1111/j.1365-2966.2004.07436.x

Jahanara, B., Mitsumoto, M., Oka, K., Matsuda, T., Hachisu, I., & Boffin, H. M. J. (2005). Wind accretion in binary stars. II. Angular momentum loss. *A&A*, *441*(2), 589–595. https://doi.org/10.1051/0004-6361:20052828

Janka, H. .-., & Mueller, E. (1994). Neutron star recoils from anisotropic supernovae. *A&A*, *290*, 496–502.

Justham, S., Podsiadlowski, P., & Vink, J. S. (2014). Luminous Blue Variables and Superluminous Supernovae from Binary Mergers. *ApJ*, *796*(2), Article 121, 121. https://doi.org/10.1088/0004-637X/796/2/121

Kalogera, V., Belczynski, K., Kim, C., O'Shaughnessy, R., & Willems, B. (2007). Formation of double compact objects. *Phys. Rep.*, *442*(1-6), 75–108. https://doi.org/10.1016/j.physrep.2007.02.008

Kalogera, V., Kim, C., Lorimer, D. R., Burgay, M., D'Amico, N., Possenti, A., Manchester, R. N., Lyne, A. G., Joshi, B. C., McLaughlin, M. A., Kramer, M., Sarkissian, J. M., & Camilo, F. (2004). The Cosmic Coalescence Rates for Double Neutron Star Binaries. *ApJ*, *601*(2), L179–L182. https://doi.org/10.1086/382155

Kamiński, T., Mason, E., Tylenda, R., & Schmidt, M. R. (2015). Post-outburst spectra of a stellar-merger remnant of V1309 Scorpii: from a twin of V838 Monocerotis to a clone of V4332 Sagittarii. *A&A*, *580*, Article A34, A34. https://doi.org/10.1051/0004-6361/201526212

Kangas, T., Mattila, S., Kankare, E., Lundqvist, P., Väisänen, P., Childress, M., Pignata, G., McCully, C., Valenti, S., Vinkó, J., Pastorello, A., Elias-Rosa, N., Fraser, M., Gal-Yam, A., Kotak, R., Kotilainen, J. K., Smartt, S. J., Galbany, L., Harmanen, J., … Young, D. R. (2016). Supernova 2013fc in a circumnuclear ring of a luminous infrared galaxy: the big brother of SN 1998S. *MNRAS*, *456*(1), 323–346. https://doi.org/10.1093/mnras/stv2567

Kasen, D., & Bildsten, L. (2010). Supernova Light Curves Powered by Young Magnetars. *ApJ*, *717*(1), 245–249. https://doi.org/10.1088/0004-637X/717/1/245

Kasen, D., Metzger, B., Barnes, J., Quataert, E., & Ramirez-Ruiz, E. (2017). Origin of the heavy elements in binary neutron-star mergers from a gravitational-wave event. *Nature*, *551*(7678), 80–84. https://doi.org/10.1038/nature24453

Kasen, D., & Woosley, S. E. (2009). Type II Supernovae: Model Light Curves and Standard Candle Relationships. *ApJ*, *703*(2), 2205–2216. https://doi.org/10.1088/0004-637X/703/2/2205

Kasliwal, M. M., Nakar, E., Singer, L. P., Kaplan, D. L., Cook, D. O., Van Sistine, A., Lau, R. M., Fremling, C., Gottlieb, O., Jencson, J. E., Adams, S. M., Feindt, U., Hotokezaka, K., Ghosh, S., Perley, D. A., Yu, P. .-., Piran, T., Allison, J. R., Anupama, G. C., … Zhao, W. (2017). Illuminating gravitational waves: A concordant picture of photons from a neutron star merger. *Science*, *358*(6370), 1559–1565. https://doi.org/10.1126/science.aap9455

Khan, A., Paschalidis, V., Ruiz, M., & Shapiro, S. L. (2018). Disks around merging binary black holes: From GW150914 to supermassive black holes. *Phys. Rev. D*, *97*(4), Article 044036, 044036. https://doi.org/10.1103/PhysRevD.97.044036

Kiewe, M., Gal-Yam, A., Arcavi, I., Leonard, D. C., Emilio Enriquez, J., Cenko, S. B., Fox, D. B., Moon, D.-S., Sand, D. J., Soderberg, A. M., & CCCP, T. (2012). Caltech Core-Collapse Project (CCCP) Observations of Type IIn Supernovae: Typical Properties and Implications for Their Progenitor Stars. *ApJ*, *744*(1), Article 10, 10. https://doi.org/10.1088/0004-637X/744/1/10

Kiziltan, B., Kottas, A., De Yoreo, M., & Thorsett, S. E. (2013). The Neutron Star Mass Distribution. *ApJ*, *778*(1), Article 66, 66. https://doi.org/10.1088/0004-637X/778/1/66

Kleiser, I. K. W., Kasen, D., & Duffell, P. C. (2018). Models of bright nickel-free supernovae from stripped massive stars with circumstellar shells. *MNRAS*, *475*(3), 3152–3164. https://doi.org/10.1093/mnras/stx3321

Klencki, J., Nelemans, G., Istrate, A. G., & Chruslinska, M. (2021). It has to be cool: Supergiant progenitors of binary black hole mergers from common-envelope evolution. *A&A*, *645*, Article A54, A54. https://doi.org/10.1051/0004-6361/202038707

Kochanek, C. S., Beacom, J. F., Kistler, M. D., Prieto, J. L., Stanek, K. Z., Thompson, T. A., & Yüksel, H. (2008). A Survey About Nothing: Monitoring a Million Supergiants for Failed Supernovae. *ApJ*, *684*(2), 1336–1342. https://doi.org/10.1086/590053

Kotera, K., & Silk, J. (2016). Ultrahigh-energy Cosmic Rays and Black Hole Mergers. *ApJ*, *823*(2), Article L29, L29. https://doi.org/10.3847/2041-8205/823/2/L29

Krtička, J., Kubát, J., & Krtičková, I. (2018). Wind inhibition by X-ray irradiation in HMXBs: the influence of clumping and the final X-ray luminosity. *A&A*, *620*, Article A150, A150. https://doi.org/10.1051/0004-6361/201833419

Kruckow, M. U., Tauris, T. M., Langer, N., Szécsi, D., Marchant, P., & Podsiadlowski, P. (2016). Common-envelope ejection in massive binary stars. Implications for the progenitors of GW150914 and GW151226. *A&A*, *596*, Article A58, A58. https://doi.org/10.1051/0004-6361/201629420

Kruckow, M. U. (2020). Masses of double neutron star mergers. *A&A*, *639*, Article A123, A123. https://doi.org/10.1051/0004-6361/202037519

Kushnir, D., Zaldarriaga, M., Kollmeier, J. A., & Waldman, R. (2016). GW150914: spin-based constraints on the merger time of the progenitor system. *MNRAS*, *462*(1), 844–849. https://doi.org/10.1093/mnras/stw1684

Kushnir, D., Zaldarriaga, M., Kollmeier, J. A., & Waldman, R. (2017). Dynamical tides reexpressed. *MNRAS*, *467*(2), 2146–2149. https://doi.org/10.1093/mnras/stx255

Lamers, H. J. G. L. M., & Cassinelli, J. P. (1999). *Introduction to Stellar Winds*.

Langer, N. (2012). Presupernova Evolution of Massive Single and Binary Stars. *ARA&A*, *50*, 107–164. https://doi.org/10.1146/annurev-astro-081811-125534

Laplace, E., Götberg, Y., de Mink, S. E., Justham, S., & Farmer, R. (2020). The expansion of stripped-envelope stars: Consequences for supernovae and gravitational-wave progenitors. *A&A*, *637*, Article A6, A6. https://doi.org/10.1051/0004-6361/201937300

Laplace, E., Justham, S., Renzo, M., Götberg, Y., Farmer, R., Vartanyan, D., & de Mink, S. E. (2021). Different to the core: The pre-supernova structures of massive single and binary-stripped stars. *A&A*, *656*, Article A58, A58. https://doi.org/10.1051/0004-6361/202140506

Lau, M. Y. M., Mandel, I., Vigna-Gómez, A., Neijssel, C. J., Stevenson, S., & Sesana, A. (2020). Detecting double neutron stars with LISA. *MNRAS*, *492*(3), 3061–3072. https://doi.org/10.1093/mnras/staa002

Law-Smith, J. A. P., Everson, R. W., Ramirez-Ruiz, E., de Mink, S. E., van Son, L. A. C., Götberg, Y., Zellmann, S., Vigna-Gómez, A., Renzo, M., Wu, S., Schrøder, S. L., Foley, R. J., & Hutchinson-Smith, T. (2020). Successful Common Envelope Ejection and Binary Neutron Star Formation in 3D Hydrodynamics. *arXiv e-prints*, Article arXiv:2011.06630, arXiv:2011.06630.

Lee, W. H., & Ramirez-Ruiz, E. (2006). Accretion Modes in Collapsars: Prospects for Gamma-Ray Burst Production. *ApJ*, *641*(2), 961–971. https://doi.org/10.1086/500533

Levesque, E. M., Massey, P., Zytkow, A. N., & Morrell, N. (2014). Discovery of a Thorne-Zytkow object candidate in the Small Magellanic Cloud. *MNRAS*, *443*, L94–L98. https://doi.org/10.1093/mnrasl/slu080

Levine, A., Rappaport, S., Deeter, J. E., Boynton, P. E., & Nagase, F. (1993). Discovery of Orbital Decay in SMC X-1. *ApJ*, *410*, 328. https://doi.org/10.1086/172750

Levine, A. M., Rappaport, S. A., & Zojcheski, G. (2000). Orbital Decay in LMC X-4. *ApJ*, *541*(1), 194–202. https://doi.org/10.1086/309398

Liebling, S. L., & Palenzuela, C. (2016). Electromagnetic luminosity of the coalescence of charged black hole binaries. *Phys. Rev. D*, *94*(6), Article 064046, 064046. https://doi.org/10.1103/PhysRevD.94.064046

LIGO Scientific, & Virgo Collaboration. (2017). GW170104: Observation of a 50-Solar-Mass Binary Black Hole Coalescence at Redshift 0.2. *Phys. Rev. Lett.*, *118*(22), Article 221101, 221101. https://doi.org/10.1103/PhysRevLett.118.221101

LIGO Scientific Collaboration, & VIRGO Collaboration. (2016). GW151226: Observation of Gravitational Waves from a 22-Solar-Mass Binary Black Hole Coalescence. *Phys. Rev. Lett.*, *116*(24), Article 241103, 241103. https://doi.org/10.1103/PhysRevLett.116.241103

LIGO Scientific Collaboration, & Virgo Collaboration. (2016a). Astrophysical Implications of the Binary Black-hole Merger GW150914. *ApJ*, *818*(2), Article L22, L22. https://doi.org/10.3847/2041-8205/818/2/L22

LIGO Scientific Collaboration, & Virgo Collaboration. (2016b). Observation of Gravitational Waves from a Binary Black Hole Merger. *Phys. Rev. Lett.*, *116*(6), Article 061102, 061102. https://doi.org/10.1103/PhysRevLett.116.061102

LIGO Scientific Collaboration, & Virgo Collaboration. (2017a). GW170608: Observation of a 19 Solar-mass Binary Black Hole Coalescence. *ApJ*, *851*(2), Article L35, L35. https://doi.org/10.3847/2041-8213/aa9f0c

LIGO Scientific Collaboration, & Virgo Collaboration. (2017b). GW170814: A Three-Detector Observation of Gravitational Waves from a Binary Black Hole Coalescence. *Phys. Rev. Lett.*, *119*(14), Article 141101, 141101. https://doi.org/10.1103/PhysRevLett.119.141101

LIGO Scientific Collaboration, & Virgo Collaboration. (2017c). GW170817: Observation of Gravitational Waves from a Binary Neutron Star Inspiral. *Phys. Rev. Lett.*, *119*(16), Article 161101, 161101. https://doi.org/10.1103/PhysRevLett.119.161101

LIGO Scientific Collaboration, & Virgo Collaboration. (2019a). Binary Black Hole Population Properties Inferred from the First and Second Observing Runs of

Advanced LIGO and Advanced Virgo. *ApJ*, *882*(2), Article L24, L24. https://doi.org/10.3847/2041-8213/ab3800

LIGO Scientific Collaboration, & Virgo Collaboration. (2019b). GWTC-1: A Gravitational-Wave Transient Catalog of Compact Binary Mergers Observed by LIGO and Virgo during the First and Second Observing Runs. *Physical Review X*, *9*(3), Article 031040, 031040. https://doi.org/10.1103/PhysRevX.9.031040

LIGO Scientific Collaboration, & Virgo Collaboration. (2021). GWTC-2: Compact Binary Coalescences Observed by LIGO and Virgo during the First Half of the Third Observing Run. *Physical Review X*, *11*(2), Article 021053, 021053. https://doi.org/10.1103/PhysRevX.11.021053

LIGO Scientific Collaboration, Virgo Collaboration, & Burns, a. ((2017). Gravitational Waves and Gamma-Rays from a Binary Neutron Star Merger: GW170817 and GRB 170817A. *ApJ*, *848*(2), Article L13, L13. https://doi.org/10.3847/2041-8213/aa920c

Ligo Scientific Collaboration, VIRGO Collaboration, & KAGRA Collaboration. (2021). Observation of Gravitational Waves from Two Neutron Star-Black Hole Coalescences. *ApJ*, *915*(1), Article L5, L5. https://doi.org/10.3847/2041-8213/ac082e

LIGO Scientific Collaboration, Virgo Collaboration, & South Africa/MeerKAT, S. (2017). Multi-messenger Observations of a Binary Neutron Star Merger. *ApJ*, *848*(2), Article L12, L12. https://doi.org/10.3847/2041-8213/aa91c9

Lin, D. N. C. (1977). Angular momentum loss and mass-exchange instability in binary stars. *MNRAS*, *179*, 265–273. https://doi.org/10.1093/mnras/179.2.265

Livio, M., & Soker, N. (1988). The Common Envelope Phase in the Evolution of Binary Stars. *ApJ*, *329*, 764. https://doi.org/10.1086/166419

Lorimer, D. R., & Kramer, M. (2012). *Handbook of Pulsar Astronomy*.

Lovegrove, E., & Woosley, S. E. (2013). Very Low Energy Supernovae from Neutrino Mass Loss. *ApJ*, *769*(2), Article 109, 109. https://doi.org/10.1088/0004-637X/769/2/109

LSST Science Collaboration, Abell, P. A., Allison, J., Anderson, S. F., Andrew, J. R., Angel, J. R. P., Armus, L., Arnett, D., Asztalos, S. J., Axelrod, T. S., Bailey, S., Ballantyne, D. R., Bankert, J. R., Barkhouse, W. A., Barr, J. D., Barrientos, L. F., Barth, A. J., Bartlett, J. G., Becker, A. C., … Zhan, H. (2009). LSST Science Book, Version 2.0. *arXiv e-prints*, Article arXiv:0912.0201, arXiv:0912.0201.

Lucy, L. B., & Solomon, P. M. (1970). Mass Loss by Hot Stars. *ApJ*, *159*, 879. https://doi.org/10.1086/150365

Lyne, A. G., & Lorimer, D. R. (1994). High birth velocities of radio pulsars. *Nature*, *369*(6476), 127–129. https://doi.org/10.1038/369127a0

Ma, X., Hopkins, P. F., Kasen, D., Quataert, E., Faucher-Giguère, C.-A., Kereš, D., Murray, N., & Strom, A. (2016). Binary stars can provide the 'missing photons' needed for reionization. *MNRAS*, *459*(4), 3614–3619. https://doi.org/10.1093/mnras/stw941

MacFadyen, A. I., & Woosley, S. E. (1999). Collapsars: Gamma-Ray Bursts and Explosions in "Failed Supernovae". *ApJ*, *524*(1), 262–289. https://doi.org/10.1086/307790

MacFadyen, A. I., Woosley, S. E., & Heger, A. (2001). Supernovae, Jets, and Collapsars. *ApJ*, *550*(1), 410–425. https://doi.org/10.1086/319698

MacLeod, M., Antoni, A., Murguia-Berthier, A., Macias, P., & Ramirez-Ruiz, E. (2017). Common Envelope Wind Tunnel: Coefficients of Drag and Accretion in a Simplified Context for Studying Flows around Objects Embedded within Stellar Envelopes. *ApJ*, *838*(1), Article 56, 56. https://doi.org/10.3847/1538-4357/aa6117

MacLeod, M., Macias, P., Ramirez-Ruiz, E., Grindlay, J., Batta, A., & Montes, G. (2017). Lessons from the Onset of a Common Envelope Episode: the Remarkable M31 2015 Luminous Red Nova Outburst. *ApJ*, *835*(2), Article 282, 282. https://doi.org/10.3847/1538-4357/835/2/282

MacLeod, M., Ostriker, E. C., & Stone, J. M. (2018a). Bound Outflows, Unbound Ejecta, and the Shaping of Bipolar Remnants during Stellar Coalescence. *ApJ*, *868*(2), Article 136, 136. https://doi.org/10.3847/1538-4357/aae9eb

MacLeod, M., Ostriker, E. C., & Stone, J. M. (2018b). Runaway Coalescence at the Onset of Common Envelope Episodes. *ApJ*, *863*(1), Article 5, 5. https://doi.org/10.3847/1538-4357/aacf08

MacLeod, M., & Ramirez-Ruiz, E. (2015). On the Accretion-fed Growth of Neutron Stars during Common Envelope. *ApJ*, *798*(1), Article L19, L19. https://doi.org/10.1088/2041-8205/798/1/L19

MacLeod, M., Vick, M., Lai, D., & Stone, J. M. (2019). Polygram Stars: Resonant Tidal Excitation of Fundamental Oscillation Modes in Asynchronous Stellar Coalescence. *ApJ*, *877*(1), Article 28, 28. https://doi.org/10.3847/1538-4357/ab184c

Mandel, I. (2016). Estimates of black hole natal kick velocities from observations of low-mass X-ray binaries. *MNRAS*, *456*(1), 578–581. https://doi.org/10.1093/mnras/stv2733

Mandel, I., & Broekgaarden, F. S. (2022). Rates of compact object coalescences. *Living Reviews in Relativity*, *25*(1), Article 1, 1. https://doi.org/10.1007/s41114-021-00034-3

Mandel, I., & Farmer, A. (2022). Merging stellar-mass binary black holes. *Phys. Rep.*, *955*, 1–24. https://doi.org/10.1016/j.physrep.2022.01.003

Mandel, I., & Müller, B. (2020). Simple recipes for compact remnant masses and natal kicks. *MNRAS*, *499*(3), 3214–3221. https://doi.org/10.1093/mnras/staa3043

Mandel, I., Müller, B., Riley, J., de Mink, S. E., Vigna-Gómez, A., & Chattopadhyay, D. (2021). Binary population synthesis with probabilistic remnant mass and kick prescriptions. *MNRAS*, *500*(1), 1380–1384. https://doi.org/10.1093/mnras/staa3390

Marcaide, J. M., Martı**********-Vidal, I., Perez-Torres, M. A., Alberdi, A., Guirado, J. C., Ros, E., & Weiler, K. W. (2009). 1.6 GHz VLBI observations of SN 1979C: almost-free expansion. *A&A*, *503*(3), 869–872. https://doi.org/10.1051/0004-6361/200912485

Margutti, R., Metzger, B. D., Chornock, R., Vurm, I., Roth, N., Grefenstette, B. W., Savchenko, V., Cartier, R., Steiner, J. F., Terreran, G., Margalit, B., Migliori, G., Milisavljevic, D., Alexander, K. D., Bietenholz, M., Blanchard, P. K., Bozzo, E., Brethauer, D., Chilingarian, I. V., … Paterson, K. (2019). An Embedded X-Ray Source Shines through the Aspherical AT 2018cow: Revealing the Inner Workings of the Most Luminous Fast-evolving Optical Transients. *ApJ*, *872*(1), Article 18, 18. https://doi.org/10.3847/1538-4357/aafa01

Margutti, R., Milisavljevic, D., Soderberg, A. M., Chornock, R., Zauderer, B. A., Murase, K., Guidorzi, C., Sanders, N. E., Kuin, P., Fransson, C., Levesque, E. M., Chandra, P., Berger, E., Bianco, F. B., Brown, P. J., Challis, P., Chatzopoulos, E., Cheung, C. C., Choi, C., … Stringfellow, G. (2014). A Panchromatic View of the

Restless SN 2009ip Reveals the Explosive Ejection of a Massive Star Envelope. *ApJ*, *780*(1), Article 21, 21. https://doi.org/10.1088/0004-637X/780/1/21

Margutti, R., Kamble, A., Milisavljevic, D., Zapartas, E., de Mink, S. E., Drout, M., Chornock, R., Risaliti, G., Zauderer, B. A., Bietenholz, M., Cantiello, M., Chakraborti, S., Chomiuk, L., Fong, W., Grefenstette, B., Guidorzi, C., Kirshner, R., Parrent, J. T., Patnaude, D., … Harrison, F. (2017). Ejection of the Massive Hydrogen-rich Envelope Timed with the Collapse of the Stripped SN 2014C. *ApJ*, *835*(2), Article 140, 140. https://doi.org/10.3847/1538-4357/835/2/140

Martin, R. G., Nixon, C., Xie, F.-G., & King, A. (2018). Circumbinary discs around merging stellar-mass black holes. *MNRAS*, *480*(4), 4732–4737. https://doi.org/10.1093/mnras/sty2178

Mason, E., Diaz, M., Williams, R. E., Preston, G., & Bensby, T. (2010). The peculiar nova V1309 Scorpii/nova Scorpii 2008. A candidate twin of V838 Monocerotis. *A&A*, *516*, Article A108, A108. https://doi.org/10.1051/0004-6361/200913610

Mattei, J., Johnson, G. E., Rosino, L., Rafanelli, P., & Kirshner, R. (1979). Supernova in NGC 4321. *IAU Circ.*, *3348*, 1.

Matzner, C. D. (2003). Supernova hosts for gamma-ray burst jets: dynamical constraints. *MNRAS*, *345*(2), 575–589. https://doi.org/10.1046/j.1365-8711.2003.06969.x

Matzner, C. D., & McKee, C. F. (1999). The Expulsion of Stellar Envelopes in Core-Collapse Supernovae. *ApJ*, *510*(1), 379–403. https://doi.org/10.1086/306571

Mauerhan, J., Williams, G. G., Smith, N., Smith, P. S., Filippenko, A. V., Hoffman, J. L., Milne, P., Leonard, D. C., Clubb, K. I., Fox, O. D., & Kelly, P. L. (2014). Multi-epoch spectropolarimetry of SN 2009ip: direct evidence for aspherical circumstellar material. *MNRAS*, *442*(2), 1166–1180. https://doi.org/10.1093/mnras/stu730

McDowell, A. T., Duffell, P. C., & Kasen, D. (2018). Interaction of a Supernova with a Circumstellar Disk. *ApJ*, *856*(1), Article 29, 29. https://doi.org/10.3847/1538-4357/aaa96e

Metzger, B. D., Giannios, D., & Spiegel, D. S. (2012). Optical and X-ray transients from planet-star mergers. *MNRAS*, *425*(4), 2778–2798. https://doi.org/10.1111/j.1365-2966.2012.21444.x

Metzger, B. D. (2022). Luminous Fast Blue Optical Transients and Type Ibn/Icn SNe from Wolf-Rayet/Black Hole Mergers. *arXiv e-prints*, Article arXiv:2203.04331, arXiv:2203.04331.

Metzger, B. D., & Fernández, R. (2014). Red or blue? A potential kilonova imprint of the delay until black hole formation following a neutron star merger. *MNRAS*, *441*(4), 3444–3453. https://doi.org/10.1093/mnras/stu802

Metzger, B. D., & Pejcha, O. (2017). Shock-powered light curves of luminous red novae as signatures of pre-dynamical mass-loss in stellar mergers. *MNRAS*, *471*(3), 3200–3211. https://doi.org/10.1093/mnras/stx1768

Miller-Jones, J. C. A., Bahramian, A., Orosz, J. A., Mandel, I., Gou, L., Maccarone, T. J., Neijssel, C. J., Zhao, X., Ziółkowski, J., Reid, M. J., Uttley, P., Zheng, X., Byun, D.-Y., Dodson, R., Grinberg, V., Jung, T., Kim, J.-S., Marcote, B., Markoff, S., … Wilms, J. (2021). Cygnus X-1 contains a 21-solar mass black hole—Implications for massive star winds. *Science*, *371*(6533), 1046–1049. https://doi.org/10.1126/science.abb3363

Moe, M., & Di Stefano, R. (2017). Mind Your Ps and Qs: The Interrelation between Period (P) and Mass-ratio (Q) Distributions of Binary Stars. *ApJS*, *230*(2), Article 15, 15. https://doi.org/10.3847/1538-4365/aa6fb6

Mohamed, S., & Podsiadlowski, P. (2011). Wind Roche-Lobe Overflow: A New Mass Transfer Mode for Mira-type Binaries. In F. Kerschbaum, T. Lebzelter, & R. F. Wing (Eds.), *Why galaxies care about agb stars ii: Shining examples and common inhabitants* (p. 355).

Montes, M. J., Weiler, K. W., Van Dyk, S. D., Panagia, N., Lacey, C. K., Sramek, R. A., & Park, R. (2000). Radio Observations of SN 1979C: Evidence for Rapid Presupernova Evolution. *ApJ*, *532*(2), 1124–1131. https://doi.org/10.1086/308602

Moriya, T., Tominaga, N., Tanaka, M., Nomoto, K., Sauer, D. N., Mazzali, P. A., Maeda, K., & Suzuki, T. (2010). Fallback Supernovae: A Possible Origin of Peculiar Supernovae with Extremely Low Explosion Energies. *ApJ*, *719*(2), 1445–1453. https://doi.org/10.1088/0004-637X/719/2/1445

Moriya, T. J. (2018). Explosions of Thorne-Żytkow objects. *MNRAS*, *475*(1), L49–L51. https://doi.org/10.1093/mnrasl/sly005

Moriya, T. J., Blinnikov, S. I., Tominaga, N., Yoshida, N., Tanaka, M., Maeda, K., & Nomoto, K. (2013). Light-curve modelling of superluminous supernova 2006gy:

collision between supernova ejecta and a dense circumstellar medium. *MNRAS*, *428*(2), 1020–1035. https://doi.org/10.1093/mnras/sts075

Moriya, T. J., & Maeda, K. (2012). A Dip after the Early Emission of Superluminous Supernovae: A Signature of Shock Breakout within Dense Circumstellar Media. *ApJ*, *756*(1), Article L22, L22. https://doi.org/10.1088/2041-8205/756/1/L22

Moriya, T. J., Maeda, K., Taddia, F., Sollerman, J., Blinnikov, S. I., & Sorokina, E. I. (2013). An analytic bolometric light curve model of interaction-powered supernovae and its application to Type IIn supernovae. *MNRAS*, *435*(2), 1520–1535. https://doi.org/10.1093/mnras/stt1392

Moriya, T. J., Mazzali, P. A., Tominaga, N., Hachinger, S., Blinnikov, S. I., Tauris, T. M., Takahashi, K., Tanaka, M., Langer, N., & Podsiadlowski, P. (2017). Light-curve and spectral properties of ultrastripped core-collapse supernovae leading to binary neutron stars. *MNRAS*, *466*(2), 2085–2098. https://doi.org/10.1093/mnras/stw3225

Morozova, V., Ott, C. D., & Piro, A. L. (2015). SNEC: SuperNova Explosion Code.

Morozova, V., Piro, A. L., Renzo, M., & Ott, C. D. (2016). Numerical Modeling of the Early Light Curves of Type IIP Supernovae. *ApJ*, *829*(2), Article 109, 109. https://doi.org/10.3847/0004-637X/829/2/109

Morozova, V., Piro, A. L., Renzo, M., Ott, C. D., Clausen, D., Couch, S. M., Ellis, J., & Roberts, L. F. (2015). Light Curves of Core-collapse Supernovae with Substantial Mass Loss Using the New Open-source SuperNova Explosion Code (SNEC). *ApJ*, *814*(1), Article 63, 63. https://doi.org/10.1088/0004-637X/814/1/63

Morozova, V., Piro, A. L., & Valenti, S. (2017). Unifying Type II Supernova Light Curves with Dense Circumstellar Material. *ApJ*, *838*(1), Article 28, 28. https://doi.org/10.3847/1538-4357/aa6251

Morozova, V., Piro, A. L., & Valenti, S. (2018). Measuring the Progenitor Masses and Dense Circumstellar Material of Type II Supernovae. *ApJ*, *858*(1), Article 15, 15. https://doi.org/10.3847/1538-4357/aab9a6

Morozova, V., & Stone, J. M. (2018). Theoretical X-Ray Light Curves of Young SNe. II. The Example of SN 2013ej. *ApJ*, *867*(1), Article 4, 4. https://doi.org/10.3847/1538-4357/aae2b3

Müller, B. (2020). Hydrodynamics of core-collapse supernovae and their progenitors. *Living Reviews in Computational Astrophysics*, *6*(1), Article 3, 3. https://doi.org/10.1007/s41115-020-0008-5

Müller, B., Heger, A., Liptai, D., & Cameron, J. B. (2016). A simple approach to the supernova progenitor-explosion connection. *MNRAS*, *460*(1), 742–764. https://doi.org/10.1093/mnras/stw1083

Müller, P. E., & Vink, J. S. (2008). A consistent solution for the velocity field and mass-loss rate of massive stars. *A&A*, *492*(2), 493–509. https://doi.org/10.1051/0004-6361:20078798

Murase, K., Kashiyama, K., Mészáros, P., Shoemaker, I., & Senno, N. (2016). Ultrafast Outflows from Black Hole Mergers with a Minidisk. *ApJ*, *822*(1), Article L9, L9. https://doi.org/10.3847/2041-8205/822/1/L9

Murguia-Berthier, A., MacLeod, M., Ramirez-Ruiz, E., Antoni, A., & Macias, P. (2017). Accretion Disk Assembly During Common Envelope Evolution: Implications for Feedback and LIGO Binary Black Hole Formation. *ApJ*, *845*(2), Article 173, 173. https://doi.org/10.3847/1538-4357/aa8140

Murguia-Berthier, A., Montes, G., Ramirez-Ruiz, E., De Colle, F., & Lee, W. H. (2014). Necessary Conditions for Short Gamma-Ray Burst Production in Binary Neutron Star Mergers. *ApJ*, *788*(1), Article L8, L8. https://doi.org/10.1088/2041-8205/788/1/L8

Nagakura, H., Morinaga, T., Kato, C., & Yamada, S. (2019). Fast-pairwise Collective Neutrino Oscillations Associated with Asymmetric Neutrino Emissions in Core-collapse Supernovae. *ApJ*, *886*(2), Article 139, 139. https://doi.org/10.3847/1538-4357/ab4cf2

Nagakura, H., Sumiyoshi, K., & Yamada, S. (2019). Possible Early Linear Acceleration of Proto-neutron Stars via Asymmetric Neutrino Emission in Core-collapse Supernovae. *ApJ*, *880*(2), Article L28, L28. https://doi.org/10.3847/2041-8213/ab30ca

Nakamura, K., Takiwaki, T., Kuroda, T., & Kotake, K. (2015). Systematic features of axisymmetric neutrino-driven core-collapse supernova models in multiple progenitors. *PASJ*, *67*(6), Article 107, 107. https://doi.org/10.1093/pasj/psv073

O'Connor, E., & Ott, C. D. (2011). Black Hole Formation in Failing Core-Collapse Supernovae. *ApJ*, *730*(2), Article 70, 70. https://doi.org/10.1088/0004-637X/730/2/70

Ofek, E. O., Fox, D., Cenko, S. B., Sullivan, M., Gnat, O., Frail, D. A., Horesh, A., Corsi, A., Quimby, R. M., Gehrels, N., Kulkarni, S. R., Gal-Yam, A., Nugent, P. E., Yaron, O., Filippenko, A. V., Kasliwal, M. M., Bildsten, L., Bloom, J. S., Poznanski, D., ... Surace, J. (2013). X-Ray Emission from Supernovae in Dense Circumstellar Matter Environments: A Search for Collisionless Shocks. *ApJ*, *763*(1), Article 42, 42. https://doi.org/10.1088/0004-637X/763/1/42

Ofek, E. O., Lin, L., Kouveliotou, C., Younes, G., Göğüş, E., Kasliwal, M. M., & Cao, Y. (2013). SN 2009ip: Constraints on the Progenitor Mass-loss Rate. *ApJ*, *768*(1), Article 47, 47. https://doi.org/10.1088/0004-637X/768/1/47

Ofek, E. O., Sullivan, M., Cenko, S. B., Kasliwal, M. M., Gal-Yam, A., Kulkarni, S. R., Arcavi, I., Bildsten, L., Bloom, J. S., Horesh, A., Howell, D. A., Filippenko, A. V., Laher, R., Murray, D., Nakar, E., Nugent, P. E., Silverman, J. M., Shaviv, N. J., Surace, J., & Yaron, O. (2013). An outburst from a massive star 40 days before a supernova explosion. *Nature*, *494*(7435), 65–67. https://doi.org/10.1038/nature11877

Ofek, E. O., Arcavi, I., Tal, D., Sullivan, M., Gal-Yam, A., Kulkarni, S. R., Nugent, P. E., Ben-Ami, S., Bersier, D., Cao, Y., Cenko, S. B., De Cia, A., Filippenko, A. V., Fransson, C., Kasliwal, M. M., Laher, R., Surace, J., Quimby, R., & Yaron, O. (2014). Interaction-powered Supernovae: Rise-time versus Peak-luminosity Correlation and the Shock-breakout Velocity. *ApJ*, *788*(2), Article 154, 154. https://doi.org/10.1088/0004-637X/788/2/154

Offner, S. S. R., Moe, M., Kratter, K. M., Sadavoy, S. I., Jensen, E. L. N., & Tobin, J. J. (2022). The Origin and Evolution of Multiple Star Systems. *arXiv e-prints*, Article arXiv:2203.10066, arXiv:2203.10066.

Ohlmann, S. T., Röpke, F. K., Pakmor, R., & Springel, V. (2017). Constructing stable 3D hydrodynamical models of giant stars. *A&A*, *599*, Article A5, A5. https://doi.org/10.1051/0004-6361/201629692

Özel, F., & Freire, P. (2016). Masses, Radii, and the Equation of State of Neutron Stars. *ARA&A*, *54*, 401–440. https://doi.org/10.1146/annurev-astro-081915-023322

Paczynski, B. (1976). Common Envelope Binaries. In P. Eggleton, S. Mitton, & J. Whelan (Eds.), *Structure and evolution of close binary systems* (p. 75).

Paczynski, B. (1983). Models of X-ray bursters with radius expansion. *ApJ*, *267*, 315–321. https://doi.org/10.1086/160870

Paczyński, B., & Sienkiewicz, R. (1972). Evolution of Close Binaries VIII. Mass Exchange on the Dynamical Time Scale. *Acta Astron.*, *22*, 73–91.

Pan, T., Patnaude, D., & Loeb, A. (2013). Superluminous X-ray emission from the interaction of supernova ejecta with dense circumstellar shells. *MNRAS*, *433*(1), 838–848. https://doi.org/10.1093/mnras/stt780

Patnaude, D. J., Loeb, A., & Jones, C. (2011). Evidence for a possible black hole remnant in the Type IIL Supernova 1979C. *New A*, *16*(3), 187–190. https://doi.org/10.1016/j.newast.2010.09.004

Paxton, B., Bildsten, L., Dotter, A., Herwig, F., Lesaffre, P., & Timmes, F. (2011). Modules for Experiments in Stellar Astrophysics (MESA). *ApJS*, *192*(1), Article 3, 3. https://doi.org/10.1088/0067-0049/192/1/3

Paxton, B., Cantiello, M., Arras, P., Bildsten, L., Brown, E. F., Dotter, A., Mankovich, C., Montgomery, M. H., Stello, D., Timmes, F. X., & Townsend, R. (2013). Modules for Experiments in Stellar Astrophysics (MESA): Planets, Oscillations, Rotation, and Massive Stars. *ApJS*, *208*(1), Article 4, 4. https://doi.org/10.1088/0067-0049/208/1/4

Paxton, B., Marchant, P., Schwab, J., Bauer, E. B., Bildsten, L., Cantiello, M., Dessart, L., Farmer, R., Hu, H., Langer, N., Townsend, R. H. D., Townsley, D. M., & Timmes, F. X. (2015). Modules for Experiments in Stellar Astrophysics (MESA): Binaries, Pulsations, and Explosions. *ApJS*, *220*(1), Article 15, 15. https://doi.org/10.1088/0067-0049/220/1/15

Paxton, B., Schwab, J., Bauer, E. B., Bildsten, L., Blinnikov, S., Duffell, P., Farmer, R., Goldberg, J. A., Marchant, P., Sorokina, E., Thoul, A., Townsend, R. H. D., & Timmes, F. X. (2018). Modules for Experiments in Stellar Astrophysics (MESA): Convective Boundaries, Element Diffusion, and Massive Star Explosions. *ApJS*, *234*(2), Article 34, 34. https://doi.org/10.3847/1538-4365/aaa5a8

Paxton, B., Smolec, R., Schwab, J., Gautschy, A., Bildsten, L., Cantiello, M., Dotter, A., Farmer, R., Goldberg, J. A., Jermyn, A. S., Kanbur, S. M., Marchant, P., Thoul, A., Townsend, R. H. D., Wolf, W. M., Zhang, M., & Timmes, F. X. (2019). Mod-

ules for Experiments in Stellar Astrophysics (MESA): Pulsating Variable Stars, Rotation, Convective Boundaries, and Energy Conservation. *ApJS*, *243*(1), Article 10, 10. https://doi.org/10.3847/1538-4365/ab2241

Pejcha, O. (2014). Burying a Binary: Dynamical Mass Loss and a Continuous Optically thick Outflow Explain the Candidate Stellar Merger V1309 Scorpii. *ApJ*, *788*(1), Article 22, 22. https://doi.org/10.1088/0004-637X/788/1/22

Pejcha, O., Metzger, B. D., & Tomida, K. (2016a). Binary stellar mergers with marginally bound ejecta: excretion discs, inflated envelopes, outflows, and their luminous transients. *MNRAS*, *461*(3), 2527–2539. https://doi.org/10.1093/mnras/stw1481

Pejcha, O., Metzger, B. D., & Tomida, K. (2016b). Cool and luminous transients from mass-losing binary stars. *MNRAS*, *455*(4), 4351–4372. https://doi.org/10.1093/mnras/stv2592

Pejcha, O., Metzger, B. D., Tyles, J. G., & Tomida, K. (2017). Pre-explosion Spiral Mass Loss of a Binary Star Merger. *ApJ*, *850*(1), Article 59, 59. https://doi.org/10.3847/1538-4357/aa95b9

Pejcha, O., & Thompson, T. A. (2012). The Physics of the Neutrino Mechanism of Core-collapse Supernovae. *ApJ*, *746*(1), Article 106, 106. https://doi.org/10.1088/0004-637X/746/1/106

Pejcha, O., & Thompson, T. A. (2015). The Landscape of the Neutrino Mechanism of Core-collapse Supernovae: Neutron Star and Black Hole Mass Functions, Explosion Energies, and Nickel Yields. *ApJ*, *801*(2), Article 90, 90. https://doi.org/10.1088/0004-637X/801/2/90

Perna, R., Duffell, P., Cantiello, M., & MacFadyen, A. I. (2014). The Fate of Fallback Matter around Newly Born Compact Objects. *ApJ*, *781*(2), Article 119, 119. https://doi.org/10.1088/0004-637X/781/2/119

Perna, R., Lazzati, D., & Farr, W. (2019). Limits on Electromagnetic Counterparts of Gravitational-wave-detected Binary Black Hole Mergers. *ApJ*, *875*(1), Article 49, 49. https://doi.org/10.3847/1538-4357/ab107b

Perna, R., Lazzati, D., & Giacomazzo, B. (2016). Short Gamma-Ray Bursts from the Merger of Two Black Holes. *ApJ*, *821*(1), Article L18, L18. https://doi.org/10.3847/2041-8205/821/1/L18

Podsiadlowski, P. (2007). Massive Binary Mergers and Thorne-Zytkow Objects. In N. St. -Louis & A. F. J. Moffat (Eds.), *Massive stars in interactive binaries* (p. 541).

Podsiadlowski, P., Joss, P. C., & Hsu, J. J. L. (1992). Presupernova Evolution in Massive Interacting Binaries. *ApJ*, *391*, 246. https://doi.org/10.1086/171341

Podsiadlowski, P., Cannon, R. C., & Rees, M. J. (1995). The evolution and final fate of massive Thorne-Zytkow objects. *MNRAS*, *274*(2), 485–490. https://doi.org/10.1093/mnras/274.2.485

Podsiadlowski, P., Ivanova, N., Justham, S., & Rappaport, S. (2010). Explosive common-envelope ejection: implications for gamma-ray bursts and low-mass black-hole binaries. *MNRAS*, *406*(2), 840–847. https://doi.org/10.1111/j.1365-2966.2010.16751.x

Poniatowski, L. G., Sundqvist, J. O., Kee, N. D., Owocki, S. P., Marchant, P., Decin, L., de Koter, A., Mahy, L., & Sana, H. (2021). Dynamically inflated wind models of classical Wolf-Rayet stars. *A&A*, *647*, Article A151, A151. https://doi.org/10.1051/0004-6361/202039595

Popham, R., Woosley, S. E., & Fryer, C. (1999). Hyperaccreting Black Holes and Gamma-Ray Bursts. *ApJ*, *518*(1), 356–374. https://doi.org/10.1086/307259

Popov, D. V. (1993). An Analytical Model for the Plateau Stage of Type II Supernovae. *ApJ*, *414*, 712. https://doi.org/10.1086/173117

Portegies Zwart, S. F., & McMillan, S. L. W. (2000). Black Hole Mergers in the Universe. *ApJ*, *528*(1), L17–L20. https://doi.org/10.1086/312422

Postnov, K. A., & Yungelson, L. R. (2014). The Evolution of Compact Binary Star Systems. *Living Reviews in Relativity*, *17*(1), Article 3, 3. https://doi.org/10.12942/lrr-2014-3

Price, D. J. (2007). splash: An Interactive Visualisation Tool for Smoothed Particle Hydrodynamics Simulations. *PASA*, *24*(3), 159–173. https://doi.org/10.1071/AS07022

Prieto, J. L., Brimacombe, J., Drake, A. J., & Howerton, S. (2013). The 2012 Rise of the Remarkable Type IIn SN 2009ip. *ApJ*, *763*(2), Article L27, L27. https://doi.org/10.1088/2041-8205/763/2/L27

Puls, J., Vink, J. S., & Najarro, F. (2008). Mass loss from hot massive stars. *A&A Rev.*, *16*(3-4), 209–325. https://doi.org/10.1007/s00159-008-0015-8

Qin, Y., Fragos, T., Meynet, G., Andrews, J., Sørensen, M., & Song, H. F. (2018). The spin of the second-born black hole in coalescing binary black holes. *A&A*, *616*, Article A28, A28. https://doi.org/10.1051/0004-6361/201832839

Quataert, E., & Kasen, D. (2012). Swift 1644+57: the longest gamma-ray burst? *MNRAS*, *419*(1), L1–L5. https://doi.org/10.1111/j.1745-3933.2011.01151.x

Quataert, E., & Shiode, J. (2012). Wave-driven mass loss in the last year of stellar evolution: setting the stage for the most luminous core-collapse supernovae. *MNRAS*, *423*(1), L92–L96. https://doi.org/10.1111/j.1745-3933.2012.01264.x

Quataert, E., Fernández, R., Kasen, D., Klion, H., & Paxton, B. (2016). Super-Eddington stellar winds driven by near-surface energy deposition. *MNRAS*, *458*(2), 1214–1233. https://doi.org/10.1093/mnras/stw365

Raaijmakers, G., Greif, S. K., Hebeler, K., Hinderer, T., Nissanke, S., Schwenk, A., Riley, T. E., Watts, A. L., Lattimer, J. M., & Ho, W. C. G. (2021). Constraints on the Dense Matter Equation of State and Neutron Star Properties from NICER's Mass-Radius Estimate of PSR J0740+6620 and Multimessenger Observations. *ApJ*, *918*(2), Article L29, L29. https://doi.org/10.3847/2041-8213/ac089a

Raaijmakers, G., Nissanke, S., Foucart, F., Kasliwal, M. M., Bulla, M., Fernández, R., Henkel, A., Hinderer, T., Hotokezaka, K., Lukošiūtė, K., Venumadhav, T., Antier, S., Coughlin, M. W., Dietrich, T., & Edwards, T. D. P. (2021). The Challenges Ahead for Multimessenger Analyses of Gravitational Waves and Kilonova: A Case Study on GW190425. *ApJ*, *922*(2), Article 269, 269. https://doi.org/10.3847/1538-4357/ac222d

Raithel, C. A., Sukhbold, T., & Özel, F. (2018). Confronting Models of Massive Star Evolution and Explosions with Remnant Mass Measurements. *ApJ*, *856*(1), Article 35, 35. https://doi.org/10.3847/1538-4357/aab09b

Ramirez-Ruiz, E., Andrews, J. J., & Schrøder, S. L. (2019). Did GW170817 Harbor a Pulsar? *ApJ*, *883*(1), Article L6, L6. https://doi.org/10.3847/2041-8213/ab3f2c

Remillard, R. A., & McClintock, J. E. (2006). X-Ray Properties of Black-Hole Binaries. *ARA&A*, *44*(1), 49–92. https://doi.org/10.1146/annurev.astro.44.051905.092532

Repetto, S., & Nelemans, G. (2015). Constraining the formation of black holes in short-period black hole low-mass X-ray binaries. *MNRAS*, *453*(3), 3341–3355. https://doi.org/10.1093/mnras/stv1753

Rezzolla, L., Most, E. R., & Weih, L. R. (2018). Using Gravitational-wave Observations and Quasi-universal Relations to Constrain the Maximum Mass of Neutron Stars. *ApJ*, *852*(2), Article L25, L25. https://doi.org/10.3847/2041-8213/aaa401

Roberts, L. F., Kasen, D., Lee, W. H., & Ramirez-Ruiz, E. (2011). Electromagnetic Transients Powered by Nuclear Decay in the Tidal Tails of Coalescing Compact Binaries. *ApJ*, *736*(1), Article L21, L21. https://doi.org/10.1088/2041-8205/736/1/L21

Rodriguez, C. L., Haster, C.-J., Chatterjee, S., Kalogera, V., & Rasio, F. A. (2016). Dynamical Formation of the GW150914 Binary Black Hole. *ApJ*, *824*(1), Article L8, L8. https://doi.org/10.3847/2041-8205/824/1/L8

Rodriguez, C. L., Zevin, M., Pankow, C., Kalogera, V., & Rasio, F. A. (2016). Illuminating Black Hole Binary Formation Channels with Spins in Advanced LIGO. *ApJ*, *832*(1), Article L2, L2. https://doi.org/10.3847/2041-8205/832/1/L2

Rodr1**********guez-González, A., Esquivel, A., Raga, A. C., & Cantó, J. (2008). The Formation of Filamentary Structures in Radiative Cluster Winds. *ApJ*, *684*(2), 1384–1389. https://doi.org/10.1086/590071

Romero-Shaw, I. M., Farrow, N., Stevenson, S., Thrane, E., & Zhu, X.-J. (2020). On the origin of GW190425. *MNRAS*, *496*(1), L64–L69. https://doi.org/10.1093/mnrasl/slaa084

Rosdahl, J., Katz, H., Blaizot, J., Kimm, T., Michel-Dansac, L., Garel, T., Haehnelt, M., Ocvirk, P., & Teyssier, R. (2018). The SPHINX cosmological simulations of the first billion years: the impact of binary stars on reionization. *MNRAS*, *479*(1), 994–1016. https://doi.org/10.1093/mnras/sty1655

Sadowski, A., Belczynski, K., Bulik, T., Ivanova, N., Rasio, F. A., & O'Shaughnessy, R. (2008). The Total Merger Rate of Compact Object Binaries in the Local Universe. *ApJ*, *676*(2), 1162–1169. https://doi.org/10.1086/528932

Safarzadeh, M., Ramirez-Ruiz, E., & Berger, E. (2020). Does GW190425 Require an Alternative Formation Pathway than a Fast-merging Channel? *ApJ*, *900*(1), Article 13, 13. https://doi.org/10.3847/1538-4357/aba596

Saladino, M. I., & Pols, O. R. (2019). The eccentric behaviour of windy binary stars. *A&A*, *629*, Article A103, A103. https://doi.org/10.1051/0004-6361/201935625

Saladino, M. I., Pols, O. R., & Abate, C. (2019). Slowly, slowly in the wind. 3D hydrodynamical simulations of wind mass transfer and angular-momentum loss in AGB binary systems. *A&A*, *626*, Article A68, A68. https://doi.org/10.1051/0004-6361/201834598

Saladino, M. I., Pols, O. R., van der Helm, E., Pelupessy, I., & Portegies Zwart, S. (2018). Gone with the wind: the impact of wind mass transfer on the orbital evolution of AGB binary systems. *A&A*, *618*, Article A50, A50. https://doi.org/10.1051/0004-6361/201832967

Salpeter, E. E. (1955). The Luminosity Function and Stellar Evolution. *ApJ*, *121*, 161. https://doi.org/10.1086/145971

Sana, H., de Mink, S. E., de Koter, A., Langer, N., Evans, C. J., Gieles, M., Gosset, E., Izzard, R. G., Le Bouquin, J. .-., & Schneider, F. R. N. (2012). Binary Interaction Dominates the Evolution of Massive Stars. *Science*, *337*(6093), 444. https://doi.org/10.1126/science.1223344

Schneider, F. R. N., Podsiadlowski, P., & Müller, B. (2021). Pre-supernova evolution, compact-object masses, and explosion properties of stripped binary stars. *A&A*, *645*, Article A5, A5. https://doi.org/10.1051/0004-6361/202039219

Schootemeijer, A., Langer, N., Grin, N. J., & Wang, C. (2019). Constraining mixing in massive stars in the Small Magellanic Cloud. *A&A*, *625*, Article A132, A132. https://doi.org/10.1051/0004-6361/201935046

Schrøder, S. L., Batta, A., & Ramirez-Ruiz, E. (2018). Black Hole Formation in Fallback Supernova and the Spins of LIGO Sources. *ApJ*, *862*(1), Article L3, L3. https://doi.org/10.3847/2041-8213/aacf8d

Schrøder, S. L., MacLeod, M., Ramirez-Ruiz, E., Mandel, I., Fragos, T., Loeb, A., & Everson, R. W. (2021). The Evolution of Binaries under the Influence of Radiation-Driven Winds from a Stellar Companion. *arXiv e-prints*, Article arXiv:2107.09675, arXiv:2107.09675.

Schwarz, D. H., & Pringle, J. E. (1996). A self-colliding stellar wind model for SN 1979C. *MNRAS*, *282*(3), 1018–1026. https://doi.org/10.1093/mnras/282.3.1018

Senno, N., Murase, K., & Mészáros, P. (2016). Choked jets and low-luminosity gamma-ray bursts as hidden neutrino sources. *Phys. Rev. D*, *93*(8), Article 083003, 083003. https://doi.org/10.1103/PhysRevD.93.083003

Shima, E., Matsuda, T., Takeda, H., & Sawada, K. (1985). Hydrodynamic calculations of axisymmetric accretion flow. *MNRAS*, *217*, 367–386. https://doi.org/10.1093/mnras/217.2.367

Shiode, J. H., & Quataert, E. (2014). Setting the Stage for Circumstellar Interaction in Core-Collapse Supernovae. II. Wave-driven Mass Loss in Supernova Progenitors. *ApJ*, *780*(1), Article 96, 96. https://doi.org/10.1088/0004-637X/780/1/96

Shivvers, I., Groh, J. H., Mauerhan, J. C., Fox, O. D., Leonard, D. C., & Filippenko, A. V. (2015). Early Emission from the Type IIn Supernova 1998S at High Resolution. *ApJ*, *806*(2), Article 213, 213. https://doi.org/10.1088/0004-637X/806/2/213

Shu, F. H., Lubow, S. H., & Anderson, L. (1979). On the structure of contact binaries. III. Mass and energy flow. *ApJ*, *229*, 223–241. https://doi.org/10.1086/156948

Siegel, D. M., Barnes, J., & Metzger, B. D. (2019). Collapsars as a major source of r-process elements. *Nature*, *569*(7755), 241–244. https://doi.org/10.1038/s41586-019-1136-0

Smith, N. (2014). Mass Loss: Its Effect on the Evolution and Fate of High-Mass Stars. *ARA&A*, *52*, 487–528. https://doi.org/10.1146/annurev-astro-081913-040025

Smith, N. (2017). Interacting Supernovae: Types IIn and Ibn. In A. W. Alsabti & P. Murdin (Eds.), *Handbook of supernovae* (p. 403). https://doi.org/10.1007/978-3-319-21846-5_38

Smith, N., & Arnett, W. D. (2014). Preparing for an Explosion: Hydrodynamic Instabilities and Turbulence in Presupernovae. *ApJ*, *785*(2), Article 82, 82. https://doi.org/10.1088/0004-637X/785/2/82

Smith, N., Mauerhan, J. C., & Prieto, J. L. (2014). SN 2009ip and SN 2010mc: core-collapse Type IIn supernovae arising from blue supergiants. *MNRAS*, *438*(2), 1191–1207. https://doi.org/10.1093/mnras/stt2269

Smith, N., & McCray, R. (2007). Shell-shocked Diffusion Model for the Light Curve of SN 2006gy. *ApJ*, *671*(1), L17–L20. https://doi.org/10.1086/524681

Smith, N., Miller, A., Li, W., Filippenko, A. V., Silverman, J. M., Howard, A. W., Nugent, P., Marcy, G. W., Bloom, J. S., Ghez, A. M., Lu, J., Yelda, S., Bernstein, R. A., & Colucci, J. E. (2010). Discovery of Precursor Luminous Blue Variable Outbursts in Two Recent Optical Transients: The Fitfully Variable Missing Links UGC 2773-OT and SN 2009ip. *AJ*, *139*(4), 1451–1467. https://doi.org/10.1088/0004-6256/139/4/1451

Socrates, A., Blaes, O., Hungerford, A., & Fryer, C. L. (2005). The Neutrino Bubble Instability: A Mechanism for Generating Pulsar Kicks. *ApJ*, *632*(1), 531–562. https://doi.org/10.1086/431786

Soker, N. (2019). The class of supernova progenitors that result from fatal common envelope evolution. *Science China Physics, Mechanics, and Astronomy*, *62*(11), Article 119501, 119501. https://doi.org/10.1007/s11433-019-9402-x

Soker, N., & Gilkis, A. (2018). Explaining iPTF14hls as a common-envelope jets supernova. *MNRAS*, *475*(1), 1198–1202. https://doi.org/10.1093/mnras/stx3287

Soker, N., Grichener, A., & Gilkis, A. (2019). Diversity of common envelope jets supernovae and the fast transient AT2018cow. *MNRAS*, *484*(4), 4972–4979. https://doi.org/10.1093/mnras/stz364

Soker, N., Grichener, A., & Sabach, E. (2018). Radiating the Hydrogen Recombination Energy during Common Envelope Evolution. *ApJ*, *863*(1), Article L14, L14. https://doi.org/10.3847/2041-8213/aad736

Soker, N., & Tylenda, R. (2006). Violent stellar merger model for transient events. *MNRAS*, *373*(2), 733–738. https://doi.org/10.1111/j.1365-2966.2006.11056.x

Song, C.-Y., & Liu, T. (2019). Black Hole Hyperaccretion Inflow-Outflow Model. II. Long-duration Gamma-Ray Bursts and Supernova ^{56}Ni Bumps. *ApJ*, *871*(1), Article 117, 117. https://doi.org/10.3847/1538-4357/aaf6ae

Springel, V. (2005). The cosmological simulation code GADGET-2. *MNRAS*, *364*(4), 1105–1134. https://doi.org/10.1111/j.1365-2966.2005.09655.x

Srinivasan, G. (2010). Recycled pulsars. *New A Rev.*, *54*(3-6), 93–100. https://doi.org/10.1016/j.newar.2010.09.026

Stevenson, S., Berry, C. P. L., & Mandel, I. (2017). Hierarchical analysis of gravitational-wave measurements of binary black hole spin-orbit misalignments. *MNRAS*, *471*(3), 2801–2811. https://doi.org/10.1093/mnras/stx1764

Stevenson, S., Vigna-Gómez, A., Mandel, I., Barrett, J. W., Neijssel, C. J., Perkins, D., & de Mink, S. E. (2017). Formation of the first three gravitational-wave observations through isolated binary evolution. *Nature Communications*, *8*, Article 14906, 14906. https://doi.org/10.1038/ncomms14906

Stone, J. M., Gardiner, T. A., Teuben, P., Hawley, J. F., & Simon, J. B. (2008). Athena: A New Code for Astrophysical MHD. *ApJS*, *178*(1), 137–177. https://doi.org/10.1086/588755

Stone, J. M., Tomida, K., White, C. J., & Felker, K. G. (2020). The Athena++ Adaptive Mesh Refinement Framework: Design and Magnetohydrodynamic Solvers. *ApJS*, *249*(1), Article 4, 4. https://doi.org/10.3847/1538-4365/ab929b

Stone, N. C., Metzger, B. D., & Haiman, Z. (2017). Assisted inspirals of stellar mass black holes embedded in AGN discs: solving the 'final au problem'. *MNRAS*, *464*(1), 946–954. https://doi.org/10.1093/mnras/stw2260

Stovall, K., Freire, P. C. C., Chatterjee, S., Demorest, P. B., Lorimer, D. R., McLaughlin, M. A., Pol, N., van Leeuwen, J., Wharton, R. S., Allen, B., Boyce, M., Brazier, A., Caballero, K., Camilo, F., Camuccio, R., Cordes, J. M., Crawford, F., Deneva, J. S., Ferdman, R. D., … Zhu, W. W. (2018). PALFA Discovery of a Highly Relativistic Double Neutron Star Binary. *ApJ*, *854*(2), Article L22, L22. https://doi.org/10.3847/2041-8213/aaad06

Sugimoto, J., Kitamoto, S., Mihara, T., & Matsuoka, M. (2017). Orbital modulations of X-ray light curves of Cygnus X-1 in its low/hard and high/soft states. *PASJ*, *69*(3), Article 52, 52. https://doi.org/10.1093/pasj/psx028

Sukhbold, T., & Adams, S. (2020). Missing red supergiants and carbon burning. *MNRAS*, *492*(2), 2578–2587. https://doi.org/10.1093/mnras/staa059

Sukhbold, T., Ertl, T., Woosley, S. E., Brown, J. M., & Janka, H. .-. (2016). Core-collapse Supernovae from 9 to 120 Solar Masses Based on Neutrino-powered Explosions. *ApJ*, *821*(1), Article 38, 38. https://doi.org/10.3847/0004-637X/821/1/38

Sukhbold, T., & Woosley, S. E. (2014). The Compactness of Presupernova Stellar Cores. *ApJ*, *783*(1), Article 10, 10. https://doi.org/10.1088/0004-637X/783/1/10

Sukhbold, T., Woosley, S. E., & Heger, A. (2018). A High-resolution Study of Presupernova Core Structure. *ApJ*, *860*(2), Article 93, 93. https://doi.org/10.3847/1538-4357/aac2da

Taam, R. E., Bodenheimer, P., & Ostriker, J. P. (1978). Double core evolution. I. A 16 M sun star with a 1 M sun neutron-star companion. *ApJ*, *222*, 269–280. https://doi.org/10.1086/156142

Taam, R. E., & Sandquist, E. L. (2000). Common Envelope Evolution of Massive Binary Stars. *ARA&A*, *38*, 113–141. https://doi.org/10.1146/annurev.astro.38.1.113

Taddia, F., Stritzinger, M. D., Sollerman, J., Phillips, M. M., Anderson, J. P., Boldt, L., Campillay, A., Castellón, S., Contreras, C., Folatelli, G., Hamuy, M., Heinrich-Josties, E., Krzeminski, W., Morrell, N., Burns, C. R., Freedman, W. L., Madore, B. F., Persson, S. E., & Suntzeff, N. B. (2013). Carnegie Supernova Project: Observations of Type IIn supernovae. *A&A*, *555*, Article A10, A10. https://doi.org/10.1051/0004-6361/201321180

Tauris, T. M., Kramer, M., Freire, P. C. C., Wex, N., Janka, H. .-., Langer, N., Podsiadlowski, P., Bozzo, E., Chaty, S., Kruckow, M. U., van den Heuvel, E. P. J., Antoniadis, J., Breton, R. P., & Champion, D. J. (2017). Formation of Double Neutron Star Systems. *ApJ*, *846*(2), Article 170, 170. https://doi.org/10.3847/1538-4357/aa7e89

Tauris, T. M., Langer, N., & Kramer, M. (2012). Formation of millisecond pulsars with CO white dwarf companions - II. Accretion, spin-up, true ages and comparison to MSPs with He white dwarf companions. *MNRAS*, *425*(3), 1601–1627. https://doi.org/10.1111/j.1365-2966.2012.21446.x

Tauris, T. M., Langer, N., Moriya, T. J., Podsiadlowski, P., Yoon, S. .-., & Blinnikov, S. I. (2013). Ultra-stripped Type Ic Supernovae from Close Binary Evolution. *ApJ*, *778*(2), Article L23, L23. https://doi.org/10.1088/2041-8205/778/2/L23

Tauris, T. M., Langer, N., & Podsiadlowski, P. (2015). Ultra-stripped supernovae: progenitors and fate. *MNRAS*, *451*(2), 2123–2144. https://doi.org/10.1093/mnras/stv990

Terman, J. L., Taam, R. E., & Hernquist, L. (1995). Double Core Evolution. VII. The Infall of a Neutron Star through the Envelope of Its Massive Star Companion. *ApJ*, *445*, 367. https://doi.org/10.1086/175702

The LIGO Scientific Collaboration, the Virgo Collaboration, & ., t. (2021). GWTC-3: Compact Binary Coalescences Observed by LIGO and Virgo During the Second Part of the Third Observing Run. *arXiv e-prints*, Article arXiv:2111.03606, arXiv:2111.03606.

Thorne, K. S., & Zytkow, A. N. (1975). Red giants and supergiants with degenerate neutron cores. *ApJ*, *199*, L19–L24. https://doi.org/10.1086/181839

Thorne, K. S., & Zytkow, A. N. (1977). Stars with degenerate neutron cores. I. Structure of equilibrium models. *ApJ*, *212*, 832–858. https://doi.org/10.1086/155109

Thorne, K. S. (1974). Disk-Accretion onto a Black Hole. II. Evolution of the Hole. *ApJ*, *191*, 507–520. https://doi.org/10.1086/152991

Tutukov, A. V., & Yungelson, L. R. (1993). The merger rate of neutron star and black hole binaries. *MNRAS*, *260*, 675–678. https://doi.org/10.1093/mnras/260.3.675

Tylenda, R., Hajduk, M., Kamiński, T., Udalski, A., Soszyński, I., Szymański, M. K., Kubiak, M., Pietrzyński, G., Poleski, R., Wyrzykowski, Ł., & Ulaczyk, K. (2011). V1309 Scorpii: merger of a contact binary. *A&A*, *528*, Article A114, A114. https://doi.org/10.1051/0004-6361/201016221

Ugliano, M., Janka, H.-T., Marek, A., & Arcones, A. (2012). Progenitor-explosion Connection and Remnant Birth Masses for Neutrino-driven Supernovae of Iron-core Progenitors. *ApJ*, *757*(1), Article 69, 69. https://doi.org/10.1088/0004-637X/757/1/69

van den Heuvel, E. P. J. (1976). Late Stages of Close Binary Systems. In P. Eggleton, S. Mitton, & J. Whelan (Eds.), *Structure and evolution of close binary systems* (p. 35).

van Kerkwijk, M. H., van Paradijs, J., Zuiderwijk, E. J., Hammerschlag-Hensberge, G., Kaper, L., & Sterken, C. (1995). Spectroscopy of HD77581 and the mass of VELA X-1. *A&A*, *303*, 483.

Verbunt, F., Igoshev, A., & Cator, E. (2017). The observed velocity distribution of young pulsars. *A&A*, *608*, Article A57, A57. https://doi.org/10.1051/0004-6361/201731518

Vigna-Gómez, A., MacLeod, M., Neijssel, C. J., Broekgaarden, F. S., Justham, S., Howitt, G., de Mink, S. E., Vinciguerra, S., & Mandel, I. (2020). Common envelope episodes that lead to double neutron star formation. *PASA*, *37*, Article e038, e038. https://doi.org/10.1017/pasa.2020.31

Vigna-Gómez, A., Neijssel, C. J., Stevenson, S., Barrett, J. W., Belczynski, K., Justham, S., de Mink, S. E., Müller, B., Podsiadlowski, P., Renzo, M., Szécsi, D., & Mandel, I. (2018). On the formation history of Galactic double neutron stars. *MNRAS*, *481*(3), 4009–4029. https://doi.org/10.1093/mnras/sty2463

Vigna-Gómez, A., Wassink, M., Klencki, J., Istrate, A., Nelemans, G., & Mandel, I. (2022). Stellar response after stripping as a model for common-envelope outcomes. *MNRAS*, *511*(2), 2326–2338. https://doi.org/10.1093/mnras/stac237

Vink, J. S. (2007). Mass-loss Predictions for Hot Stars. In R. J. Stancliffe, G. Houdek, R. G. Martin, & C. A. Tout (Eds.), *Unsolved problems in stellar physics: A conference in honor of douglas gough* (pp. 389–396). https://doi.org/10.1063/1.2818998

Vink, J. S. (2018). Very massive stars: a metallicity-dependent upper-mass limit, slow winds, and the self-enrichment of globular clusters. *A&A*, *615*, Article A119, A119. https://doi.org/10.1051/0004-6361/201832773

Vink, J. S., Heger, A., Krumholz, M. R., Puls, J., Banerjee, S., Castro, N., Chen, K. .-., Chenè, A. .-., Crowther, P. A., Daminelli, A., Gräfener, G., Groh, J. H., Hamann, W. .-., Heap, S., Herrero, A., Kaper, L., Najarro, F., Oskinova, L. M., Roman-Lopes, A., … Zhang, Y. (2015). Very Massive Stars in the local Universe. *Highlights of Astronomy*, *16*, 51–79. https://doi.org/10.1017/S1743921314004657

Voss, R., & Tauris, T. M. (2003). Galactic distribution of merging neutron stars and black holes - prospects for short gamma-ray burst progenitors and LIGO/VIRGO. *MNRAS*, *342*(4), 1169–1184. https://doi.org/10.1046/j.1365-8711.2003.06616.x

Webbink, R. F. (1984). Double white dwarfs as progenitors of R Coronae Borealis stars and type I supernovae. *ApJ*, *277*, 355–360. https://doi.org/10.1086/161701

Weiler, K. W., Sramek, R. A., Panagia, N., van der Hulst, J. M., & Salvati, M. (1986). Radio Supernovae. *ApJ*, *301*, 790. https://doi.org/10.1086/163944

Wongwathanarat, A., Janka, H. .-., & Müller, E. (2013). Three-dimensional neutrino-driven supernovae: Neutron star kicks, spins, and asymmetric ejection of nucleosynthesis products. *A&A*, *552*, Article A126, A126. https://doi.org/10.1051/0004-6361/201220636

Woosley, S. E. (1987). The Birth of Neutron Stars. In D. J. Helfand & J. .-. Huang (Eds.), *The origin and evolution of neutron stars* (p. 255).

Woosley, S. E. (2019). The Evolution of Massive Helium Stars, Including Mass Loss. *ApJ*, *878*(1), Article 49, 49. https://doi.org/10.3847/1538-4357/ab1b41

Woosley, S. E., & Bloom, J. S. (2006). The Supernova Gamma-Ray Burst Connection. *ARA&A*, *44*(1), 507–556. https://doi.org/10.1146/annurev.astro.43.072103.150558

Woosley, S. E., & Heger, A. (2006). The Progenitor Stars of Gamma-Ray Bursts. *ApJ*, *637*(2), 914–921. https://doi.org/10.1086/498500

Woosley, S. E., & Heger, A. (2007). Nucleosynthesis and remnants in massive stars of solar metallicity. *Phys. Rep.*, *442*(1-6), 269–283. https://doi.org/10.1016/j.physrep.2007.02.009

Woosley, S. E., & Heger, A. (2012). Long Gamma-Ray Transients from Collapsars. *ApJ*, *752*(1), Article 32, 32. https://doi.org/10.1088/0004-637X/752/1/32

Woosley, S. E., Langer, N., & Weaver, T. A. (1995). The Presupernova Evolution and Explosion of Helium Stars That Experience Mass Loss. *ApJ*, *448*, 315. https://doi.org/10.1086/175963

Woosley, S. E., & Weaver, T. A. (1995). The Evolution and Explosion of Massive Stars. II. Explosive Hydrodynamics and Nucleosynthesis. *ApJS*, *101*, 181. https://doi.org/10.1086/192237

Woosley, S. E., & Heger, A. (2015). The Deaths of Very Massive Stars. In J. S. Vink (Ed.), *Very massive stars in the local universe* (p. 199). https://doi.org/10.1007/978-3-319-09596-7_7

Wysocki, D., Gerosa, D., O'Shaughnessy, R., Belczynski, K., Gladysz, W., Berti, E., Kesden, M., & Holz, D. E. (2018). Explaining LIGO's observations via isolated binary evolution with natal kicks. *Phys. Rev. D*, *97*(4), Article 043014, 043014. https://doi.org/10.1103/PhysRevD.97.043014

Xu, W., & Stone, J. M. (2019). Bondi-Hoyle-Lyttleton accretion in supergiant X-ray binaries: stability and disc formation. *MNRAS*, *488*(4), 5162–5184. https://doi.org/10.1093/mnras/stz2002

Yoon, S.-C., Chun, W., Tolstov, A., Blinnikov, S., & Dessart, L. (2019). Type Ib/Ic Supernovae: Effect of Nickel Mixing on the Early-time Color Evolution and Implications for the Progenitors. *ApJ*, *872*(2), Article 174, 174. https://doi.org/10.3847/1538-4357/ab0020

Yoon, S.-C., Dessart, L., & Clocchiatti, A. (2017). Type Ib and IIb Supernova Progenitors in Interacting Binary Systems. *ApJ*, *840*(1), Article 10, 10. https://doi.org/10.3847/1538-4357/aa6afe

Zaldarriaga, M., Kushnir, D., & Kollmeier, J. A. (2018). The expected spins of gravitational wave sources with isolated field binary progenitors. *MNRAS*, *473*(3), 4174–4178. https://doi.org/10.1093/mnras/stx2577

Zapartas, E., de Mink, S. E., Justham, S., Smith, N., Renzo, M., & de Koter, A. (2021). Effect of binary evolution on the inferred initial and final core masses of hydrogen-rich, Type II supernova progenitors. *A&A*, *645*, Article A6, A6. https://doi.org/10.1051/0004-6361/202037744

Zapartas, E., Renzo, M., Fragos, T., Dotter, A., Andrews, J. J., Bavera, S. S., Coughlin, S., Misra, D., Kovlakas, K., Román-Garza, J., Serra, J. G., Qin, Y., Rocha, K. A., Tran, N. H., & Xing, Z. P. (2021). Revisiting the explodability of single massive star progenitors of stripped-envelope supernovae. *A&A*, *656*, Article L19, L19. https://doi.org/10.1051/0004-6361/202141506

Zapartas, E., de Mink, S. E., Justham, S., Smith, N., de Koter, A., Renzo, M., Arcavi, I., Farmer, R., Götberg, Y., & Toonen, S. (2019). The diverse lives of progenitors of hydrogen-rich core-collapse supernovae: the role of binary interaction. *A&A*, *631*, Article A5, A5. https://doi.org/10.1051/0004-6361/201935854

Zevin, M., Kremer, K., Siegel, D. M., Coughlin, S., Tsang, B. T. .-., Berry, C. P. L., & Kalogera, V. (2019). Can Neutron-star Mergers Explain the r-process Enrichment in Globular Clusters? *ApJ*, *886*(1), Article 4, 4. https://doi.org/10.3847/1538-4357/ab498b

Zevin, M., Spera, M., Berry, C. P. L., & Kalogera, V. (2020). Exploring the Lower Mass Gap and Unequal Mass Regime in Compact Binary Evolution. *ApJ*, *899*(1), Article L1, L1. https://doi.org/10.3847/2041-8213/aba74e

Zhang, B. (2016). Mergers of Charged Black Holes: Gravitational-wave Events, Short Gamma-Ray Bursts, and Fast Radio Bursts. *ApJ*, *827*(2), Article L31, L31. https://doi.org/10.3847/2041-8205/827/2/L31

Zhang, W., & Fryer, C. L. (2001). The Merger of a Helium Star and a Black Hole: Gamma-Ray Bursts. *ApJ*, *550*(1), 357–367. https://doi.org/10.1086/319734